UNIVERSITY OF SOUTHAMPTON

FACULTY OF PHYSICAL AND APPLIED SCIENCES

School of Physics and Astronomy

Novel paradigms for resonance energy transfer mediated hybrid photovoltaic devices

by

Maël Brossard

Thesis for the degree of Doctor of Philosophy

February 2015

UNIVERSITY OF SOUTHAMPTON

ABSTRACT

FACULTY OF PHYSICAL AND APPLIED SCIENCES
School of Physics and Astronomy

Doctor of Philosophy

Novel paradigms for resonance energy transfer mediated hybrid photovoltaic devices

By Maël Brossard

This work focuses on the utilisation of quantum dots (QDs) and resonance energy transfer to enhance the properties of existing photovoltaic technologies. Time-resolved spectroscopy is used to demonstrate that lead sulphide (PbS) QDs could be used to enhance the absorptivity of silicon solar cells. In this scheme, QDs deposited on the solar cell act as absorber, while the photogenerated excitons are transferred to the underlying silicon to contribute to the photocurrent. QD hybridization is also demonstrated in InGaP solar cells. In this case, the QDs are used to mitigate the poor utilisation of the energy absorbed in the AlInP window layer. Excitons generated in this layer are non-radiatively transferred to the QDs, which emit photons below the AlInP band-gap to generate carriers close to the depletion region of the p-n junction. The overall performance of the solar cell is found to be significantly improved after hybridization, with a large 14.6% relative and 2% absolute enhancement of the photon conversion efficiency. Finally, the integration of QDs into thin film $Cu(In,Ga)Se_2$ (CIGS) solar cells is investigated. The deposition of a non-uniform layer of QD aggregates in close proximity to the heterojunction is found to provide a 10.9% relative enhancement of the photon conversion efficiency. Enhancements of the external quantum efficiency in both the blue and near-IR ranges are attributed respectively to radiative luminescent down-shifting from the QDs and to scattering on QD aggregates. Throughout this thesis, evidence is provided that placing efficient nanocrystaline emitters near ($< \lambda$) the depletion region of photovoltaic devices can significantly increase its performance. In this context, the high energy transfer efficiency of RET at short distances makes it a very interesting coupling mechanism for hybrid solar cells integrating QDs within traditional thin-film devices.

Acknowledgements

I would like to first thank my supervisor Prof. Pavlos Lagoudakis for accepting me in his group. I was truly humbled at the chance to access state-of-the-art equipment and to work with such talented collaborators. Looking back at myself four years ago, I am amazed to see how much I learned and changed. I am especially grateful of his willingness to let me take care of responsibilities outside the scope of my PhD thesis. Attending board meetings for the Nanophotonics for Energy Efficiency network of excellence taught me for instance a lot about how research is conducted in Europe and gave me an invaluable understanding of the intricacies of research politics. I would also like to thank Prof. David Lidzey for organizing the ICARUS FP7 Program, which gave me the opportunity to attend many workshops and summer schools on hybrid photonics. I am also indebted to all the collaborators that trusted me with their samples and their results, most notably Prof. Gerasimos Konstatos, Prof. Hao-Chung Kuo and Prof. Peichen Yu for their contributions to chapter 3, 4 and 5, respectively. Prof Martin D. Charlton was a constant help throughout my thesis and for this I am grateful.

This section would of course not be complete without expressing my deep gratitude to everyone in the Hybrid Optoelectronics, who helped me go through the ups and downs of the PhD rollercoaster. I would like to especially thank Peristera Andreakous, Junis Rindermann, Chunyong Li, Niccolo Somaschi and Hamid Ohadi for helping me during the first few years of my thesis, by showing me tricks in the labs or simply sharing a beer with me when nothing seemed to work. I also need to thank the current members of the group for creating such a great atmosphere of camaraderie, Alexis Askitopoulos, Pasquale Cilibrizzi, Giuseppe Buscemi, Giacomo Piana, Julian Toepfer, Christos Grivas… only to name a few.

I would like to dedicate this thesis to my family, and specifically to my mother and my sister, who somehow managed to put up with my sometimes terrible moods without complaining too much. Their continued support made it all possible.

List of publications

- P. Andreakou, M. Brossard, C. Li, P. G. Lagoudakis, M. Bernechea, G. Konstantatos, *" Spectroscopic evidence of resonance energy transfer mechanism from PbS QDs to bulk silicon"*, EPJ Web of Science **54**, 01017 (2013)
- P. Andreakou, M. Brossard, C. Li, M. Bernechea, G. Konstantatos, P. G. Lagoudakis, Pavlos, *"Size- and Temperature-Dependent Carrier Dynamics in Oleic Acid Capped PbS Quantum Dots",* Journal of Physical Chemistry C **117**, p.1887 (2013)
- M. Brossard, C.-Y. Hong, M. Hung, P. Yu, M. D. B. Charlton, P. G. Savvidis, P. G. Lagoudakis, *"Highly Efficient Flexible Hybrid Nanocrystal-Cu(In,Ga)Se2 (CIGS) Solar Cells",* Advanced Optical Materials, DOI: 10.1002/adom.201400356 (2014)
- Y.-K. Liao, M. Brossard, D.-H. Hsieh, T.-N. Lin, M. D. B. Charlton, S.-J. Cheng, C.-H. Chen, J.-L. Shen, L.-T. Cheng, T.-P. Hsieh, F.-I Lai, S.-Y. Kuo, H.-C. Kuo, P. G. Savvidis, P. G. Lagoudakis, "*10.9% relative efficiency enhancement in hybrid flexible nanocrystal-CIGS solar cells*", Advanced Energy Materials, DOI: 10.1002/aenm.201401280 (2014)
- M. Charlton, M. Brossard, P. G. Lagoudakis, "*High efficiency solar cell: circumventing heat loss in the window layers*", United Kingdom patent, filed (2014)

Table of Contents

List of figures

List of tables

Academic Thesis: Declaration Of Authorship

I, Maël Brossard, declare that this thesis and the work presented in it are my own and has been generated by me as the result of my own original research.

Novel paradigms for resonance energy transfer mediated hybrid photovoltaic devices

I confirm that:

1. This work was done wholly or mainly while in candidature for a research degree at this University;
2. Where any part of this thesis has previously been submitted for a degree or any other qualification at this University or any other institution, this has been clearly stated;
3. Where I have consulted the published work of others, this is always clearly attributed;
4. Where I have quoted from the work of others, the source is always given. With the exception of such quotations, this thesis is entirely my own work;
5. I have acknowledged all main sources of help;
6. Where the thesis is based on work done by myself jointly with others, I have made clear exactly what was done by others and what I have contributed myself;
7. Either none of this work has been published before submission, or parts of this work have been published as: [please list references below]:

Signed:

Date: 01/02/2015

Chapter 1: Introduction

1.1. Motivation

While many alternatives energy sources have been developed during the past decades, photovoltaics (PV) technology remains one of the strongest symbols of sustainable development. The considerable amount of resources invested around the world in research and development and the large market introductions schemes implemented by most western countries have created a strong recognition of the technology as an important vector for sustainable development, both in the minds of the politicians and of the general public. In this context, the strong continued growth of the installed global capacity remains critical to the mitigation of the impacts of global warming, in a society more and more willing to move towards a post-fossil fuel economy. Despite a sustained rapid growth over the past fifteen years, the global potential of photovoltaics remains mostly untapped, and renewables (hydropower excluded) only accounted for 3% of the global electricity production in 2013 [1]. It is for instance striking to realize that the United States, with a PV generation potential in excess of 1000 exajoules per year, could “realistically” supply more than three times the global primary demand (Table 1) [2]. The potential of PV is also far greater than all other sustainable energy sources, with estimated generation potentials of respectively 1, 2, 114, 179 and 418 exajoules per year for hydro-, bio-, geothermal, wind and concentrated thermal solar energy for the U.S. territory.

Compared to traditional energy sources, photovoltaic technology also has the advantage of being highly modular, which allows photovoltaic panels to be used as power bricks to assemble small to large generation facilities [3]. This modularity could allow the decentralisation of the energy production, displacing energy production closer to the consumers and minimizing transportation losses. In a highly volatile geopolitical context impacting the world’s major oil producers, solar energy can also offer relatively stable prices only weakly dependent on fossil fuel prices [4]. This relatively stable return on

investment might provide the necessary incentive for private entities to heavily invest in PV technology and could allow PV to become gradually completely decoupled from government subsidies.

Table 1: Total estimated U.S. technical potential generation per technology [2].

Technology	Generation Potential (exajoules per year)
Urban utility-scale PV	8
Rural utility-scale PV	1010
Rooftop PV	3
Total PV	1021
Concentrated solar power	418
Onshore wind power	118
Offshore wind power	61
Total wind power	179
Biopower	2
Hydrothermal power	1
Enhanced geothermal	113
Total geothermal	114
Hydropower	1

While photovoltaics could provide large amounts of energy, the technology still suffers from important drawbacks, the most important of which being intermittency due to cloud coverage and day-only operation. This issue is especially problematic in western countries with cold to moderate climates, where the mismatch between peak production (afternoon in the summer) and peak consumption (winter in the evening) is the greatest. Introducing a large (>10%) amount of solar power in the energy mix would thus require the development and installation of large scale storage facilities. Renewable energy production plants are also typically very small scale (~1-10 MW) compared to nuclear and coal-fired power plants (~1-5 GW). Mass-scale adoption of renewable energy would thus require a rapidly evolving “smart” transportation grid, capable of handling multiple intermittent sources and large scale storage facilities and of channelling electricity between delocalised production sources and consumers. This challenge has proven technologically complex and remains

for the time being prohibitively expensive. Land-mounted PV production finally requires large amounts of land, which might be needed to feed a rapidly growing global population. Improving the efficiency of PV modules is a way to directly mitigate these issues, by lowering the generation costs, thus helping the financial viability of complex distribution and storage schemes, and by improving the surface efficiency of solar power plants.

1.2. Hybrid photonics

Colloidal semiconductor nanocrystals represent a very promising material for a wide range of applications. Such materials can be synthesised on a mass scale using low-cost liquid chemistry techniques with a wide range of sizes and shapes, ranging from simple spherical structures (quantum dots) to complex tetrapods [5,6]. Their high absorption cross section, absorption and emission tunability and their good processability make them ideal candidates for light harvesting applications. Thanks to recent advancements in surface chemistry, high photoluminescence quantum yields (PQY) in excess of 90% have now been reported [7] and materials with PQYs in excess of 60% are now commercially available. Such materials suffer however from poor charge transport properties, which drastically complicates their integration into full-scale devices. This has for now kept the efficiency of semiconductor nanocrystal solar cells to about 8% [8].

Bulk semiconductors present on the other hand rather different properties. Due to their relatively low absorption cross section, light harvesting devices need to use relatively thick films. Their bandgap is typically fixed, and can only be slightly adjusted by varying doping levels or by changing the dilution level of semiconductor alloys. The typical processing techniques involved in semiconductor manufacturing are also complex and expensive, often requiring high temperatures, vacuum conditions and clean room environments. They do however offer well established technological platforms and very good electrical properties.

Dexter was the first to propose a hybrid photovoltaic scheme, by depositing a thin layer of a strongly absorbing organic dye on top of a semiconductor cell [9]. His idea was to combine the large absorption cross section and good processability of organic molecules and the good electrical properties of bulk semiconductors. In this scheme, the organic dye

would act as an absorber, generating localised excitons that could be non-radiatively transferred to the underlying semiconductor using resonance energy transfer (RET). Hybrid QD/bulk semiconductor photovoltaics is a direct extension of this work, utilising the novel properties of colloidal QDs to funnel excitons to a solid state solar cell.

Due to its near-field nature, RET is especially interesting for thin-film heterojunction solar cells. As discussed previously, carriers are in this case typically generated very close to the heterojunction interface (~10-100nm) i.e. at roughly the same length scale as resonant energy transfer. An interesting idea stemming from this premise is to introduce an emitting material (e.g. QDs) at or near the heterojunction interface. While this can introduce recombination centres and induce resistive losses for the photogenerated carriers, the potential benefits due to RET recycling of poorly extracted carriers, to luminescent down-shifting in the QDs and to scattering on QD aggregates can far outweigh any detrimental effects. This concept is demonstrated in this thesis to a certain extent for InGaP and CIGS solar cells and represents the main direction of this thesis.

1.3. Structure of this thesis

This thesis presents the implementation of several QD hybridization schemes for different established PV technologies. In chapter 2, the relevant principles of solid state physics are detailed, along with the theoretical background of carrier confinement in QDs, of photovoltaics generation and of resonance energy transfer. The work in chapter 3 involves the hybridization of Si with lead sulphide (PbS) QDs. Time-resolved spectroscopy was used to study the dependence of the lifetime of PbS QDs on the separation distance to a silicon slab placed in close proximity, so as to unequivocally demonstrate the presence of RET between the QDs and bulk silicon. The temperature dependence of RET was also investigated. In chapter 4, a RET-mediated luminescent down-shifting layer is implemented in high efficiency InGaP solar cells by depositing an epilayer of QDs. A large increase of the photon conversion efficiency and of the quantum efficiency of the devices is demonstrated. Time-resolved spectroscopy is once again used to demonstrate the presence of RET between the QDs and the underlying semiconductor structure. In chapter 5, a luminescent down-shifting and scattering QD layer is integrated into CIGS solar cells. A significant increase of the efficiency of the devices after hybridization is again shown.

The morphology of the spray-deposited QD films is investigated, along with the electrical and optical properties of the hybrid solar cells. A discussion of the drawbacks of such an approach is provided, along with potential mitigations schemes. The final chapter provides a discussion of the potential of hybrid structures for photovoltaics generation, along with some proposed future developments.

Chapter 2: Theoretical Background

2.1. Bulk organic semiconductors

The concept of resonance energy transfer, a process that involves the coupling of excitons in different semiconductor materials, is central to this thesis. It is thus important to define semiconductors and their optical properties. Crystalline solids can be classified in three categories: insulator, conductor and semiconductor. While insulators and conductors are characterised by their ability to respectively inhibit and allow electron transport, the electron transport properties of semiconductors can be modulated over several orders of magnitude by introducing impurity atoms, in a process known as doping [10,11]. This is a direct consequence of the interaction of the carriers with the crystal lattice, which results in the formation of an energy gap in the electron levels. In the case of semiconductors, this bandgap is relatively small (~1eV) and lies between occupied and unoccupied electronic states, respectively the valence and conduction bands (see Figure 2.1), which describe the relationship between energy and momentum for electrons interacting with the lattice [12].

The valence and conduction bands can be understood by considering the hybridization of the electronic states of a hydrogen atom. In this case, the 1s ground state orbitals of the hydrogen atoms interact and are linearly combined to form hybridized bonding and antibonding states. Similarly, when a quasi-infinite number of atoms are assembled to form a crystal, their atomic levels interact and are hybridized to form energy bands that determine the electronic properties of the material. In this framework, excited electrons undergo transitions from the valence band to the conduction band, leaving unoccupied electronic states behind. These excited electrons interact with each-other and with the lattice to form a many-body system, too complex to be directly solved. These interactions are instead described by defining electron quasiparticles, of same charge and spin as elementary electrons, but with an effective mass m_e^* that varies by a factor of typically 0.01 to 10 from the true mass of the electron m_e. In the following discussion “electron” refers to the quasiparticle and not to the elementary particle. In the same fashion, the remaining

electron population in the valence band can be shown to behave as a finite number of quasiparticles of opposite spin, charge and momentum to the electrons and of mass m_h, called holes. Excited electrons and holes can freely move through the periodic potential of the crystal lattice, and are characterized by an energy and a wave vector $k = p/\hbar$, where p is the momentum of the charge carrier and $\hbar$ is the reduced Planck constant. Using the classical expression for free particles $E = p^2/2m$, the kinetic energy of the carriers can thus be expressed as

$$E = \frac{\hbar^2 k^2}{2m} \tag{1}$$

which corresponds to parabolic conduction and valence bands.

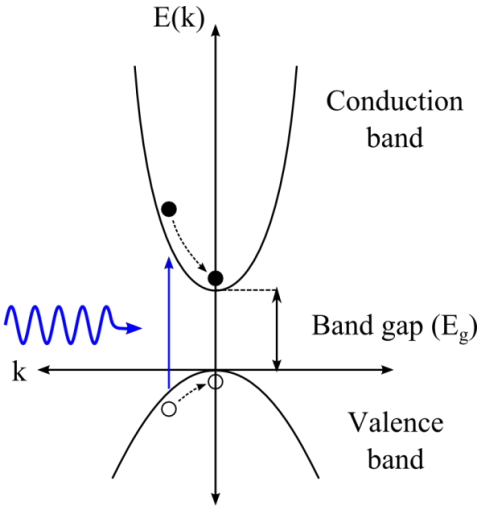

Figure 2.1: Dispersion curve for a bulk semiconductor. The absorption of a photon triggers the promotion of an electron from the valence band to the conduction band, which then thermally relaxes to the bottom of the conduction band.

In the ground state, the valence band is filled with electrons and the conduction band is empty. The promotion of an electron from the valence band to the conduction band of a semiconductor, known as an interband transition, thus requires to provide enough external energy to overcome the bandgap energy E_g. This energy can be provided in several forms, including heat, but optical transitions, mediated by the absorption of a photon, are of special interest here. In this case, a photon is absorbed by the semiconductor material and transfers energy and momentum to a carrier in the valence band, triggering an optical transition (see Figure 2.1). Since the momentum of the photon is negligible compared to

the momentum of the electron, optical transitions can be approximated as vertical transitions. The principle of conservation of energy in the process thus states that:

$$E_p = \frac{hc}{\lambda} = E_g + E_e + E_h + E_{Coulomb} \quad (2)$$

where E_p is the photon energy, h is the Planck constant, c is the speed of light, λ is the photon wavelength, E_e and E_h are respectively the kinetic energies of the electron and the hole and $E_{Coulomb}$ is the Coulomb interaction energy between the electron and the hole. The excited state can relax through the reverse transition, where the electron and the hole are annihilated and the excess energy is released as a photon or is transferred to the lattice in the form of heat.

As stated in the energy conservation equation, the electron and hole, being charged particles, interact via Coulomb interaction and form an electron-hole bound state or exciton. The resulting quasiparticle is neutral and has a slightly lower energy than its unbound constituents. The spatial extension of the excitons can be characterised by their exciton Bohr radius. This value is defined in analogy to the Bohr radius of the electron in a hydrogen atom by scaling the hydrogen Bohr radius a_0 by the dielectric constant of the material ε and by the ratio of hydrogen electron mass m_0 to the effective mass μ^*:

$$a_B^* = \varepsilon \frac{m_0}{\mu^*} a_0 = \frac{\varepsilon \hbar^2}{\mu^* e^2} \quad (3)$$

where $\hbar = \frac{h}{2\pi}$, e is the elementary charge and μ^* is the exciton effective reduced mass defined by $\mu^{*-1} = m^{*-1}_e + m^{*-1}_h$. The exciton binding energy or Rydberg energy (R_y^*) is given by $R_y^* = \frac{e^2}{2a_B^*}$ and corresponds to the ionization energy of the lowest state. Exciton Bohr radii can vary from 1 to 10nm in common bulk semiconductors, yielding Rydberg energies of 1 to 100meV. An exciton behaves as a single particle and its motion is described by its centre of mass $M^* = m_e^* + m_h^*$. The dispersion relationship can be expressed as

$$E_n(K) = E_g - \frac{R_y^*}{n^2} + \frac{\hbar K^2}{2M^*} \quad (4)$$

where K is the exciton wave vector. If an exciton is created by the absorption of a photon, the total energy E_{exc} can be derived through the equation:

$$E_{exc} = E_g - \frac{R_y^*}{n^2} \quad (5)$$

2.2. Optical transitions in colloidal quantum dots

2.2.1. Colloidal semiconductor nanocrystals

Colloidal semiconductor nanocrystals, also referred to as quantum dots (QDs), are spherically shaped crystalline inorganic particles with dimensions ranging between 2 and 50 nm. Falling in between the size ranges of large organic molecules (1-10 nm) and small bulk inorganic crystals, QDs display properties reminiscent of both molecular (for instance, narrow photoluminescence spectra and high photoluminescence quantum yields) and bulk crystalline solids (such as broad absorption spectra and good photostability). The size-dependence of the optical properties of QDs is also especially notable. Due to the confinement of the carrier wavefunction in the QDs, the energy level spacing increases with decreasing size of the particles, which makes it possible to tune QD emission wavelengths over wide ranges (>1 eV) without changing the chemical composition of the material [13,14]. This unique size-tunability of the optical and electronic properties has been the main motivation behind the development of such materials, with the aim of developing low-cost efficient optoelectronic devices. The ability of QDs to create multiple excitons from a single photon (multiexciton generation, MEG) and the prospect of producing cheap highly efficient photovoltaic devices has also generated a lot of interest in the past few years [15,16].

Since quantum confinement depends strongly on the size the QDs, the effects only become significant when the diameter of the QD becomes of the same order as the exciton Bohr radius, which represents the natural spatial extension of the exciton. Table 2 presents characteristic material properties and the exciton Bohr radii of some semiconducting materials. The exciton Bohr radius, and thus the minimum particle size necessary to observe quantum confinement, varies very significantly from semiconductor to semiconductor, with a_B values ranging from 2 nm for CdS to 104 nm for PbTe. Since the confinement energy scales approximately with the inverse of the electron and hole effective mass, materials with low carrier effective masses, i.e. high Bohr radii, will display stronger confinement effects. For example, a 2 nm PbTe QD will host much more strongly confined excitons than a CdS quantum dot of the same size. It is also important to note that, since holes are heavier than electrons in most semiconductors, quantum

confinement effects are more pronounced in the conduction band than in the valence band. IV-VI lead-salts present a notable exception to this rule, with electrons almost as heavy as or even heavier than the holes.

Table 2: Bandgap, electron, hole and exciton relative effective masses and Bohr radii for various bulk semiconductors [17].

		E_g (eV)	m_e^*/m_0	m_h^*/m_0	μ^*/m_0	$a_{B,exc}$ (nm)
II-VI	CdS	2.48	0.25	0.6	0.176	2
	CdSe	1.73	0.12	0.9	0.106	4
	CdTe	1.48	0.09	0.8	0.081	5
III-V	InP	1.34	0.073	0.45	0.063	8
	InAs	0.35	0.023	0.57	0.022	29
	InSb	0.17	0.012	0.44	0.012	61
IV-VI	PbS	0.42	0.087	0.083	0.042	21
	PbSe	0.28	0.047	0.041	0.022	55
	PbTe	0.31	0.034	0.032	0.016	104

The Bohr radii of the hole, electron and exciton define three confinement regimes for the carriers in the QDs: the weak confinement regime, if the QD radius is larger than both the electron and hole Bohr radii, the intermediate confinement regime, where either electron or hole Bohr radius is smaller than the QD radius, and the strong confinement regime, in which both Bohr radii are smaller than the QD radius. The different electronic and optical properties of QDs in the different regimes have been extensively investigated [14]. IV-VI lead-salt QDs, with similar electron and hole Bohr radii and large exciton radii, represent especially interesting materials for the study of the strong confinement regime and have been invaluable in establishing the subtleties of QD properties.

2.2.2. The “particle in a box” model

The properties of QDs can be inferred using two approaches: “top-down” and “bottom-up”. In the “bottom-up” perspective, the properties of the QDs are calculated by sequentially assembling atoms and hybridizing electron orbitals to form a core particle, using many-body simulation techniques such as the tight binding method [18]. This approach has been gaining traction in recent years, due to the rapid increase of available computational power allowing calculations on hundreds and even thousands of atoms [19]. Alternatively, the electronic properties of QDs can be derived from the properties of the bulk material, using the “top-down approach”. In this approach, QD confinement is accounted for by setting rigid zero boundary conditions to the bulk electron and hole wavefunctions at the physical boundary of the QDs. This is analogous to the simple “particle in an infinite potential well” or “particle in a box” problem of basic quantum mechanics. In this model, a charge carrier of mass m is confined in a one-dimensional symmetric potential V, defined as

$$V(x) = \begin{cases} 0 & \text{for } 0 < x < a \\ \infty & \text{for } x \leq 0 \text{ and } x \geq a \end{cases} \quad (6)$$

where a is the width of the potential. The Schrödinger equation of the carrier is in this case

$$\frac{\hbar^2}{2m_e}\frac{d^2\psi(x)}{dx^2} + V(x)\psi(x) = E\psi(x) \quad (7)$$

where E and ψ are the energy and the wavefunction of the carrier, respectively. This differential equation can be solved using functions of the form $\psi(x) = Ae^{ikx} + Be^{-ikx}$, where A and B are unit-less scaling parameters. Using the boundary conditions $\psi(0) = 0$, the wavefunction can be calculated to be $\psi(x) = C\sin(kx)$. The second boundary condition $\psi(a) = 0$ is satisfied for $C\sin(ka) = 0$, which is solved for $k = \frac{n\pi}{a}$ where $n \in \mathbb{N}^*$. In this framework, the discrete allowed energy levels are thus given by

$$E_n = \frac{\hbar^2 k^2}{2m} = \frac{\pi^2\hbar^2}{2ma^2}n^2 \quad (8)$$

This problem can be extended to a spherically symmetric potential, in which case the Schrödinger equations can be separated into radial and angular eigenfunctions

$$\psi(r.\theta,\phi) = CJ_l(kr)Y_l^m(\theta,\phi), \quad (9)$$

where C is a normalization constant, $J_l(kr)$ is the l-th order spherical Bessel function and $Y_l^m(\theta, \phi)$ is a spherical harmonic. In this case the boundary conditions impose $k = \beta_{nl}$, where β_{nl} is the n-th zero of J_l. Allowed energy levels are then given by

$$E_n = \frac{\hbar^2 \beta_{nl}^2}{2ma^2}. \tag{10}$$

Several key fundamental expectations regarding optical transitions in QDs can be derived from this simple model. First, the confinement energy is found to scale as $1/r^2$, where r is the diameter of the particle. Second, because the Coulomb attraction scales as $1/r$, the confinement energy is expected to be the main additional contribution to energy bandgap for QD of small diameter, the Coulomb attraction representing only a weak perturbation to the quantized energy states. Third, the labelling of the wavefunctions with the quantum numbers n, l, m is analogous to the hydrogen wavefunctions, which allows us to characterize QD wavefunctions as s-, p- and d-type with the appropriate selection rules derived from the angular momentum intrinsic to these symmetries.

2.2.3. Electronic and optical properties of zero-dimensional crystals

While so far we have only considered the case of a charge carrier in an empty well, the electrons and holes in QDs also feel the periodic potential of the QD lattice. This deviation from the ideal "particle in a box" model can be implemented using Bloch's theorem, which states that the wavefunction of a free carrier in a semiconductor is the product of a plane wave and of a function $u_{nk}(\vec{r})$ that follows the periodicity of the crystal lattice, the so-called Bloch function [20–22]. The electronic wavefunction can thus be written as

$$\psi_{nk}(\vec{r}) = u_{nk}(\vec{r}) e^{i\vec{k}.\vec{r}} \tag{11}$$

where n labels the energy level of the particle and $\vec{k}$ is its wave vector. The plane wave can be considered as the backbone of the wavefunction, while the Bloch function corresponds to its atomic-like portion, arising from a linear contribution of the orbitals of the atoms within the unit cell. In a QD, the lack of translational symmetry has to be accounted for, which can be done by assuming that the Bloch function is wave vector independent and is equal to the bulk value at k = 0, and by replacing the backbone by a linear combination of plane waves forming an envelope function $f(\vec{r})$ respecting the boundary conditions:

$$\psi_{nk}(\vec{r}) = u_{n0}(\vec{r}) \sum_k C_{nk}\, e^{i\vec{k}.\vec{r}} = u_{n0}(\vec{r}) f(\vec{r}) \tag{12}$$

where C_{nk} are expansion coefficients. The electron and hole wavefunctions in a QD are thus a product of three contributions: one that originates from the unit cell of the crystal (u), a spherical Bessel function satisfying the boundary conditions at the surface of the QD (j) and a spherical harmonic (Y).

The total wavefunction of the exciton in a QD can then be written as:

$$\psi_{exc}(\vec{r_e},\vec{r_h}) = \psi_e(\vec{r_e})\psi_h(\vec{r_h}) = C\left(u_c J_{L_e}(kr_e)Y_{L_e}^m\right)\left(u_v J_{L_h}(kr_h)Y_{L_h}^m\right), \quad (13)$$

where the subscripts c and v denote the conduction and the valence band, respectively, and L_e and L_h are the angular momentum quantum numbers of the spherical harmonics of the electron and of the hole. The allowed energy levels of a QD are thus predicted to be

$$E = E_g + \frac{\hbar^2\beta_{n_e,L_e}^2}{2m_e^* a^2} + \frac{\hbar^2\beta_{n_h,L_h}^2}{2m_h^* a^2} - E_C, \quad (14)$$

where E_C is a first-order correction due to the Coulombic attraction between electron and hole, which can be calculated from perturbation theory to be $1.8e^2/4\pi\epsilon a$, where e is the elementary charge and ϵ is the dielectric permittivity [23].

The probability of an optical transition exciting an electron from the valence to the conduction band of a QD is given by

$$P = |\psi_e|\vec{e}\cdot\hat{p}|\psi_p\rangle|^2, \quad (15)$$

where $\vec{e}$ is the polarization vector of the incident photon and $\hat{p}$ is the momentum operator. Assuming that the envelope function is constant within the unit cell, the momentum operator only applies to the Bloch function, giving

$$P = |u_C|\vec{e}\cdot\hat{p}|u_v\rangle|^2|f_c||f_v|^2. \quad (16)$$

Since in the case of a particle in a spherical potential the envelope function are orthonormal eigenfunctions of a Hermitian operator,

$$P = |u_C|\vec{e}\cdot\hat{p}|u_v\rangle|^2\delta_{n_e,n_h}\delta_{L_e,L_h}, \quad (17)$$

where δ is a Dirac delta function. In this formula, $|u_C|\vec{e}\cdot\hat{p}|u_v\rangle|^2$ corresponds to the transition dipole matrix element of the optical transition between the two states, while $\delta_{n_e,n_h}\delta_{L_e,L_h}$ only allows transitions following the selection rules $\Delta n = 0$ and $\Delta L = 0$ (see Figure 2.2). The lowest allowed energy level is usually visible as a peak in the absorption spectrum near the absorption onset (see for instance Figure 2.3). At these wavelengths, the photon energy is resonant with the energy level, which enhances the oscillator strength of the transition. Photon emission from photoexcited carriers follows the reverse process, and

a thermalized exciton can radiatively recombine to provide a photon at the bandgap energy. A red-shift of the photoluminescence energy compared to the lowest lying excitonic peak in the absorption spectrum can typically be observed. This effect, called Stokes shift, is due to additional contributions to the exciton wavefunction and can be induced by the anisotropy of the crystal lattice, by the non-perfectly spherical shape of the QD and by the electron-hole interaction [13].

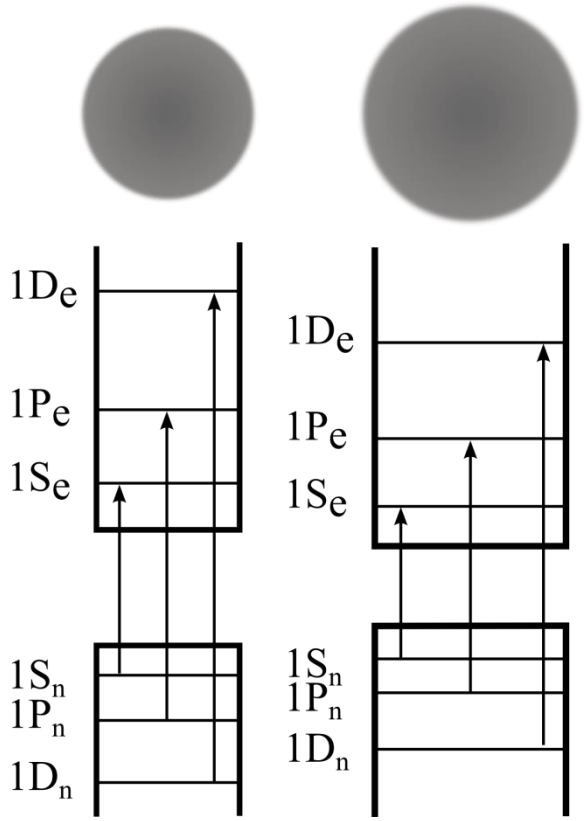

Figure 2.2: Energy level diagram and allowed optical transitions in QDs of two different sizes.

As visible from the presence of the absorption peak, quantum confinement strongly impacts the oscillator strength f of the QDs, due to the overlap between the electron and hole wavefunctions. The oscillator strength of exciton absorption per unit volume is given by the expression

$$f = \frac{2m_e^*}{\hbar^2}\Delta E|M_t|^2\left|U_{(o)}\right|^2 \tag{18}$$

where ΔE is the transition energy, M_t the transition dipole moment and $\left|U_{(o)}\right|^2$ is the probability of finding an electron and a hole in the same site [12].

2.2.4. Core-shell QDs

A number of post-synthesis surface treatments were developed to improve the properties of colloidal QDs. Due to the small size of the particles, surface atoms play a crucial role in the photophysics of the QDs. For instance, a 5 nm PbSe QD has about 40% of its atoms at the surface. The wavefunctions of the hole and of the electron extend in this case over many surface atom sites, which act as energetic traps for the charge carriers and can drastically damage the optical properties of the QD. One the most important of these modifications is the epitaxial deposition of a second semiconductor material ("the shell") on the existing particles ("the core") to form so-called "core/shell" nanostructure. Core/shell structures can be classified in two categories, depending on where the electron and the hole are trapped. In "type I" QDs, the valence band of the shell is lower than the valence band of the core and the conduction band of the shell is higher than the conduction band of the core, which confines both electron and hole inside the core. In this case, the carriers remain in close proximity and the electron and hole wavefunctions strongly overlap. In "type II" heterostructures, the valence and conduction bands of the shell are respectively higher than the valence and conduction bands of the core. This results in a separation of the carriers, with the electron trapped in the core and the hole in the shell. Due to the differences in electron and hole wavefunction overlap, these two type of core/shell heterostructures typically display very different optical properties. Since in type I structure both carriers are confined within the same material, these QDs are typically good light emitters [24,25], with demonstrated QYs in excess of 80% for CdSe/CdS/ZnS QDs [26,27]. On the contrary, the charge separation of type II QDs makes them very poor emitters, but their large dipolar strength has proven advantageous in photovoltaic devices and single exciton lasers [28,29].

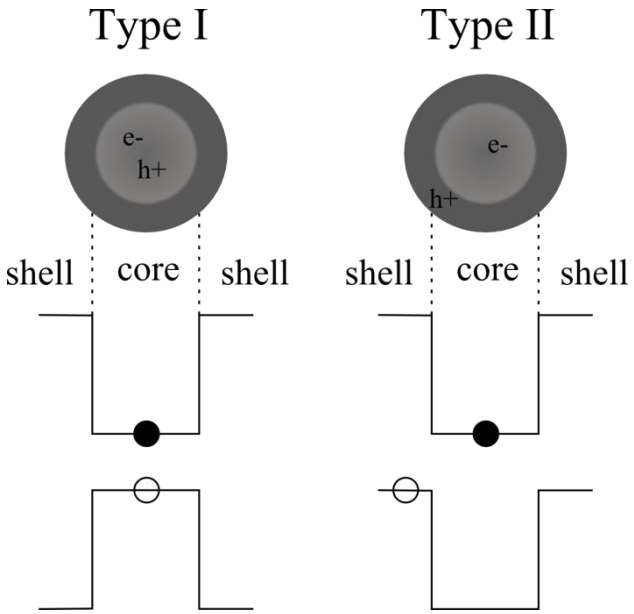

Figure 2.3: Schematic representation of type I and type II core/shell QDs.

2.3. Solar cells fundamentals

2.3.1. Photovoltaic conversion

Photovoltaic conversion, i.e. the conversion of light into usable electrical current, consists fundamentally of two steps. The first one involves the absorption of an incident photon and its conversion into an electron-hole pair or exciton. The second step corresponds to the separation of excitons into free electrons and holes and their transport to the negative and positive contacts of the device. The band diagram of a prototypical single p-n junction solar cell is depicted in Figure 2.4. The structure consists of n and p-doped Si layers sandwiched between a back and front contact, the front contact being patterned to allow the transmission of the incident light. The p-type base layer is in this case a lot thicker than the n-type emitter layer, and absorbs most of the incident light. When photons are absorbed in this layer, the minority carriers (electrons for a p-type semiconductor) diffuse towards the p-n junction, where they are swept away by the built-in depletion field and driven into the n-type layer and the top contact. Excess majority carriers (holes) are free to diffuse towards to the back contact, thus forming a usable photocurrent.

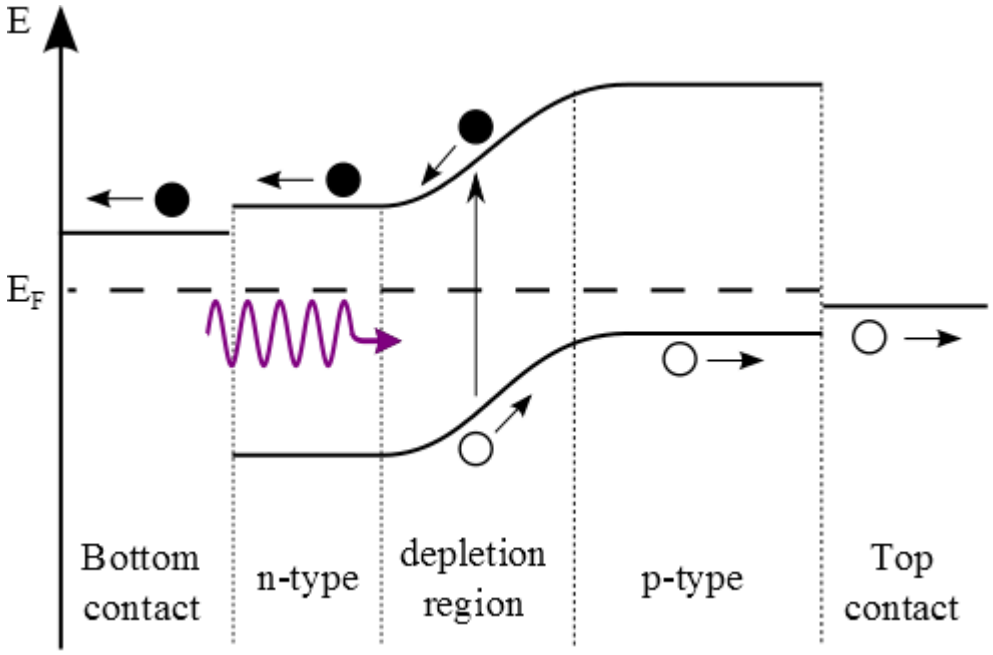

Figure 2.4: Band diagram of a prototypical single p-n junction solar cell.

An ideal solar cell can be approximated by a current source connected in parallel to a rectifying diode. The I-V characteristic of this equivalent circuit is described by the Shockley solar cell equation:

$$I = I_{ph} - I_0(e^{\frac{qV}{k_B T}} - 1) \tag{19}$$

where I_{ph} is the photogenerated photocurrent, I_0 is the diode saturation current, k_B is the Boltzmann constant, T is the absolute temperature, q is the electron charge and V is the applied voltage. The photogenerated current is closely related to the incident photon flux and is usually assumed to be independent of the applied voltage. Figure 2.5 shows the I-V characteristics of a prototypical solar cell, under one sun illumination (AM1.5 spectrum). In this case, I_{ph} corresponds to the short-circuit current I_{SC} and the open circuit current V_{OC} corresponds to the voltage necessary to cancel out the photocurrent, and is thus given by:

$$V_{OC} = \frac{k_B T}{q} \ln(1 + \frac{I_{ph}}{I_0}) \tag{20}$$

The efficiency of a solar cell is defined by the ratio of the electrical output to the energy input from the incident photon flux. The photon conversion efficiency (PCE or η) is thus defined as follows:

$$\eta = \frac{P_m}{E * S} \tag{21}$$

where P_m is the solar cell's output at the maximum power point, E is the incident light power density and S is the active area of the device. This efficiency can be derived from the I-V characteristics:

$$\eta = \frac{V_{OC} I_{Sc} FF}{E * S} \tag{22}$$

where FF is the fill factor of the solar cell. The fill factor represents an ideality parameter of the I-V characteristics, and is equal to 1 in the case of a perfectly square I-V curve.

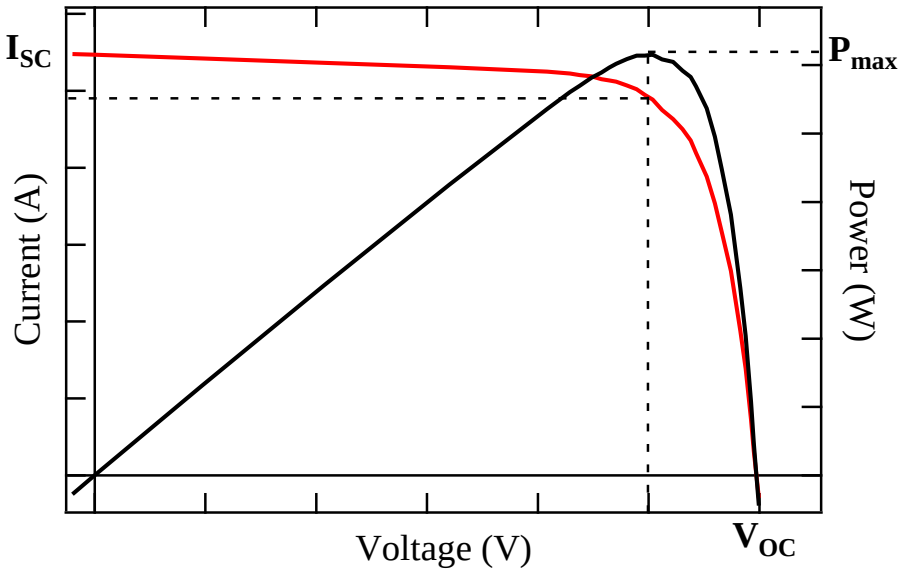

Figure 2.5: I-V (red) and P-V (black) curve for a prototypical solar cell.

2.3.2. Quantum efficiency

The quantum efficiency of a solar cell for a given wavelength is defined as the ratio of the number of electrons delivered to an external circuit to the number of incident photons of said wavelength. Two quantum efficiencies are typically defined: the external quantum efficiency (EQE) and internal quantum efficiency (IQE). These two values differ in the way they treat photons reflected and back-scattered at the front surface of the device. While the EQE takes into account the photons incident on the outside surface of the solar cell, the IQE only includes the photons absorbed by the device. The total photogenerated current can thus be derived from the EQE or IQE:

$$I_{ph} = q \int_{\lambda} \Phi(\lambda) * EQE(\lambda)\, d\lambda$$
$$= q \int_{\lambda} \Phi(\lambda) * (1 - R(\lambda) - T(\lambda)) * IQE(\lambda)\, d\lambda \quad (23)$$

where $\Phi(\lambda)$ is the photon flux incident on the cell at wavelength λ, $R(\lambda)$ and $T(\lambda)$ are respectively the reflection and transmission coefficients of the cell at λ and the integration is done over the absorbing spectral range of the solar cell.

The spectral response $SR(\lambda)$ of a device provides another way to quantify the photocurrent generated. It is defined as a ratio of the current generated by the solar cell to incident power on the solar cell. The spectral response can be derived from the EQE using the following equation:

$$SR(\lambda) = \frac{q\lambda}{hc} * EQE \quad (24)$$

where h is the Planck constant and c is the speed of light.

The EQE and spectral response of a typical silicon solar cell are displayed in Figure 2.6. A number of physical insights can be gleaned from such characteristic curves. The EQE curve shows an almost square behaviour, with a drop in the near UV and in the near IR, near the silicon bandgap. At short wavelengths, photons are absorbed very near the front surface of the solar cell, where generated carriers tend to get trapped on surface states and defects and recombine non-radiatively. On the contrary, the absorption cross-section of the material is gradually lowered at higher wavelengths and photons are absorbed very deep in the silicon p-type layer. Carriers tend in this case to recombine on defects at the back surface of the cell. For higher wavelengths, below the Si bandgap, the absorber becomes transparent and no light is absorbed. While maximum external quantum efficiencies can be very high in silicon devices (> 90%), the mismatch between measured and ideal values in the optimal wavelength range is due to reflections at the front surface and to the finite diffusion length of the generated carriers. The spectral response of the solar cell additionally shows the impact of using a fixed bandgap semiconductor. Contrary to the EQE, the spectral response gradually decreases for decreasing wavelengths, i.e. for increasing photon energies. High energy photons need to thermally relax to the Si bandgap before they can be extracted, which induces important losses in the form of heat. On the

contrary, an “ideal” device capable of extracting carriers at their generation energy (hot carriers) would provide a flat SR response curve.

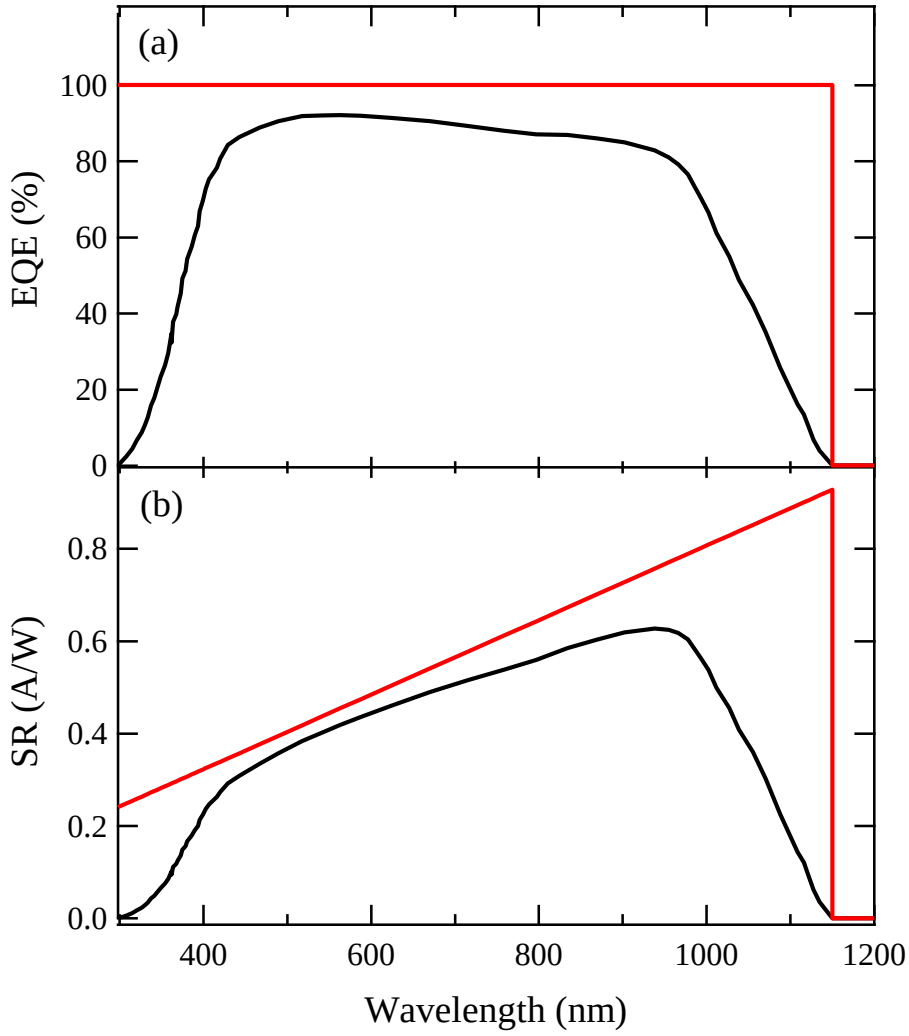

Figure 2.6: (a) External Quantum Efficiency (EQE) of a commercial (black) and ideal (red) silicon solar cell. (b) Spectral Response (SR) of a commercial (black) and ideal (red) silicon solar cell.

Several loss mechanisms are inherent to single p-n junction photovoltaic devices, and a maximum theoretical efficiency can be calculated: the Shockley-Queisser limit. Depending strongly on the material’s bandgap, this limit sets an upper boundary for the photon conversion efficiency of a PV device (Figure 2.7). Three primary mechanisms need to be taken into account. Like any material that is not at a zero absolute temperature, solar cells emit blackbody radiation. In the case of a solar cell at room temperature, these losses represent about 7% of the incoming solar energy. Radiative recombination of

photogenerated carriers can also prove a significant limiting factor for the performances of the device, by diminishing the photocurrent. Finally, the most important loss mechanism for all PV devices remains spectrum losses. As discussed previously, the presence of a single bandgap in a basic solar cell induces large losses. Before being separated and extracted, the excitons thermally relax through lattice interaction. The heat thus dissipated represents about 33% of the incoming energy for a 1.1 eV bandgap. Finally, due to the transparency of the semiconducting material below its bandgap, low energy photons are transmitted through the PV device, which represents a 19% loss for a silicon solar cell in one-sun illumination. All these fundamental losses drastically limit the efficiency of a single p-n junction device with a 1.1 eV (silicon) bandgap to 33.7%. It is to be noted that this limit is only absolute for single p-n junction devices under one-sun illumination (unconcentrated) with the assumption that a photon generates one exciton that thermally relaxes. Overcoming the Shockley-Queisser limit thus requires to negate one of these assumptions, by using tandem cells, concentrated sunlight, multiexciton generation (MEG) or hot carrier extraction schemes.

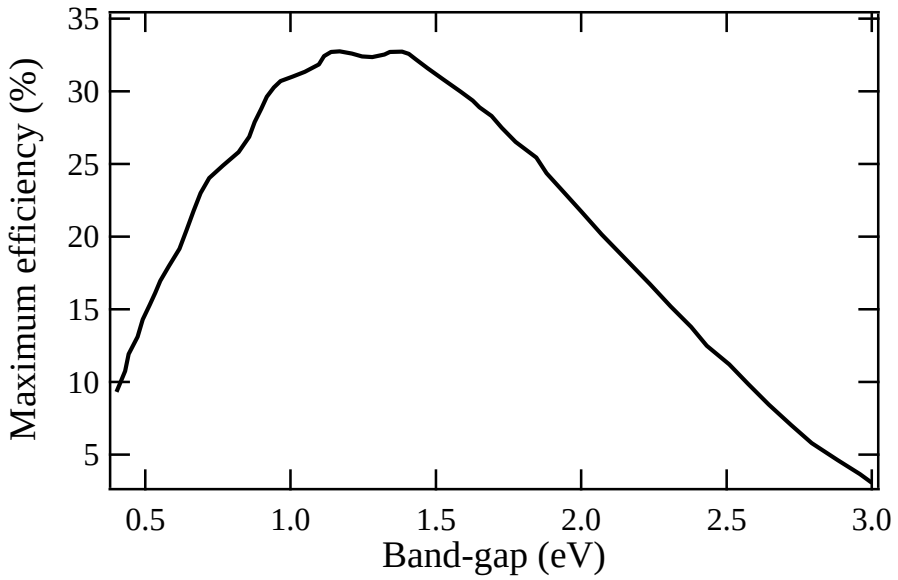

Figure 2.7: Shockley-Queisser efficiency limit as a function of the bandgap of the semiconductor material of the solar cell.

2.4. Thin film solar cells: a rapid overview

While crystalline Si solar cells now provide high PCEs and represent a robust and proven PV technology, with lab-scale cells exceeding 25.6% [30], silicon wafers remain expensive and material costs are an important limiting factor for the overall cost competitiveness of the modules. On the contrary, due to greatly lowered material consumptions, to the possibility of fabricating devices on inexpensive substrates, such a stainless steel or plastic, and to the prospect of low-cost monolithically connected tandem cells, thin-film PV technology has the potential to drive costs well below grid parity. Rapid progress has been achieved over the past 20 years, and thin-film PV now represents a significant portion of the photovoltaic production, with a market share of around 10%. Three main technologies dominate at the moment the inorganic thin-film PV market: thin-film silicon (mostly amorphous), cadmium telluride (CdTe) and copper indium gallium diselenide (CIGS).

2.4.1. a-Si:H technology

Amorphous silicon thin-films were first reported in 1965 as 'silicon from silane' deposited using radio frequency glow discharge [31]. The semiconducting nature of these materials and their successful n and p doping was only demonstrated 10 years later by Walter Spear and Peter LeComber [32]. While at the time the importance of hydrogen in the electrical properties of a-Si was not fully recognized, it was later shown that this atomic impurity plays an important role in passivating the dangling bonds of the material now referred to as hydrogenated amorphous silicon (a-Si:H). At the time, this new development gave rise to enormous amounts of interest. The large absorption cross-section of a-Si:H (1 µm being enough to absorb 90% of the visible light) coupled to the possibility of rapid low-cost plasma enhanced chemical vapour deposition (PECVD) over large areas (> $1m^2$) at low temperature (< 400°C) offered for the first time the possibility of producing cheap flexible lightweight thin-film solar cells.

Since the first a-Si:H solar cell was fabricated in 1976 with a PCE of 2.4% [33], considerable improvements in deposition and treatment technique have allowed a-Si:H single PV devices to reach PCEs in excess of 13% [30]. While these PCEs cannot compete with bulk Si or other thin-film PV technologies, the possibility of integrating such

materials into “low-cost” tandem cells has raised a lot of interest over the past decade. The low ambipolar diffusion lengths of a-Si:H (typically below ~0.3 µm) makes the use of standard p-n junction architectures inefficient, since most of the carriers would recombine before diffusing to the depletion region, and requires the use of more advanced p-i-n architectures. A schematic depiction of an a-Si:H p-i-n solar cell is presented in Figure 2.8: Schematic representation of an a-Si:H p-i-n solar cell. [34]. In these devices, an absorbing layer (~300 nm) is sandwiched between thin p- and n-doped layers (~10-20 nm), that build up a field across the active region. A textured transparent conductive oxide (TCO) contact increases light absorption by scattering incident photons. It is to be noted that these cells typically suffer from important light induced degradation issues, through a process known as the Staebler–Wronski effect, which still makes their integration into long lifetime (> 10 years) modules somehow problematic. [126]

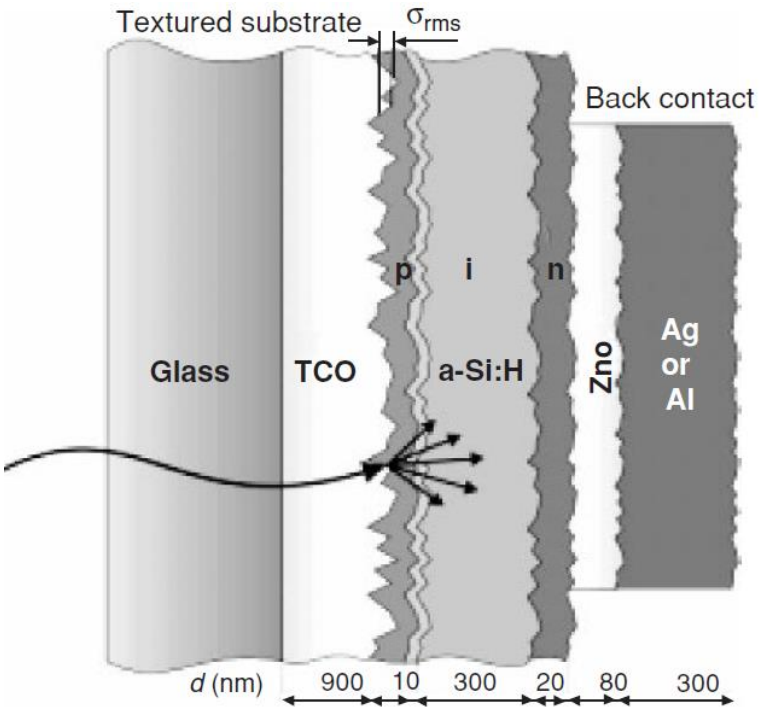

Figure 2.8: Schematic representation of an a-Si:H p-i-n solar cell. [34]

2.4.2. CIGS solar cells

With demonstrated lab-scale efficiencies in excess of 21% coupled to excellent thermo- and photo-stability when encapsulated, coper indium gallium diselenide (CIGS) solar cells have attracted a lot of attention over the past decades. A wide variety of techniques has

been used to deposit CIGS film, using both vacuum depositions, such as evaporation, and liquid processing, such as electrodeposition and spray deposition. These films typically display a polycrystalline chalcopyrite structure, with crystal sizes ranging between several hundreds of nanometres to a few microns [35]. This material is a direct p-type bandgap semiconductor, with bandgap energy that can be tuned between ~1.00 eV ($CuInSe_2$) and 1.68 eV ($CuGaSe_2$) by varying the indium/gallium ratio. Since it has proven very difficult to deposit high-quality n-type CIGS, the thick (~1 μm) absorbing CIGS layer needs to be coupled with an heterojunction partner, typically a much thinner (50-100 nm) n-CdS layer. Similarly to the homojunction case, the doping level difference between the layers builds up a strong depletion field at the CIGS/CdS interface, which allows the efficient separation of photogenerated excitons. The full device structure is typically obtained by growing successively the CIGS absorber and CdS buffer on a conductive transparent substrate, typically glass/molybdenum, and by terminating the device with intrinsic ZnO (~70 nm), aluminium doped ZnO (~100 nm) and an electric metal contact.

2.4.3. CdTe technology

With a bandgap (~1.5eV) very close to optimum value for a solar absorber, cadmium telluride (CdTe) was one of the first semiconductor to be considered for solar panels, with early research dating back to the 1950s. Similarly to CIGS and other CIS alloy technologies, CdTe solar cells are heterojunction devices, with a thick (~1-2 μm) p-type polycrystalline CdTe absorber and thinner (~100 nm) n-type CdS junction partner. The active layers are typically deposited on a TCO-coated glass substrate and terminated with Au or Ni-Al metal contact, in a superstrate configuration. Much like CIGS, CdTe has benefitted from slow but steady technological improvements, which has brought lab-scale and module efficiencies respectively above 21% and 17% in 2014 [36].

2.4.4. Conclusion on thin film PV technology

With proven lab-scale efficiencies in excess of 21%, thin-film solar cells now outperform multicrystaline technology [30]. Being much thinner than first generation devices, they can also be produced on cheap flexible substrate and be made flexible. This could potentially drastically reduce the installation costs, which represent now a very significant portion of

the overall PV system costs. The market share of thin-film PV nevertheless never exceeded 20%, and has been reclining in recent years. [37] In this context, hybridization with low cost colloidal QDs (such as the recently synthesised perovskite QDs) could enhance the commercial viability of thin-film PV system.

2.5. Resonance energy transfer

Resonance energy transfer (RET), also known as Förster resonance energy transfer (FRET), is a non-radiative near-field electrodynamic mechanism involving the transfer of excitons between an excited donor and an acceptor in the ground state. As a resonant process, it requires a good overlap between the emission spectrum of the donor and the absorption spectrum of the acceptor. The process of RET involves several step (see Figure 2.9). First a photon is absorbed by the donor, and an exciton is generated in the n^{th} excited state. This exciton rapidly (~ps) relaxes to the ground state by transferring phonons to the crystal lattice. The energy of the thermalized exciton is then transferred to the acceptor by annihilating the exciton in the donor and generating an exciton in the acceptor in a dipole-dipole interaction. The RET-generated exciton in the acceptor can then thermalize and recombine by emitting a photon. First introduced by T. Förster [38,39], RET is now routinely used to determine the separation distance between molecules in biology and chemistry. RET also of course applies to excitons in inorganic semiconductors, and many RET-optoelectronic devices have been postulated and demonstrated, both for lighting [40–44] and light harvesting applications [9,42,45–50].

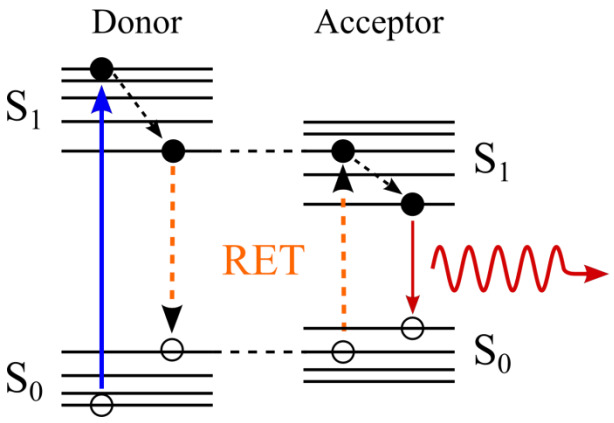

Figure 2.9: Schematic representation of RET between a donor and an acceptor

RET originates from an interaction of the form

$$H_{RET} = -\vec{E} \cdot \overrightarrow{P_a} \tag{25}$$

Where H_{RET} is the dipole-dipole coupling Hamiltonian, $\vec{E}$ is the electrostatic field generated by the oscillations of the donor dipole and $\overrightarrow{P_a}$ is the polarisation of the acceptor [45]. The electric field generated by the donor dipole at the acceptor site can be calculated using the classical equation

$$E(\vec{R}) = \frac{1}{4\pi\epsilon_0}\frac{1}{R^3}[3\frac{(\overrightarrow{P_d} \cdot \vec{R})\vec{R}}{|\vec{R}|^2} - \overrightarrow{P_d}] \tag{26}$$

where $\vec{R}$ is the vector between the donor and the acceptor and $\overrightarrow{P_d}$ denotes the polarization vector of the donor. The corresponding energy transfer rate can then be calculated to be

$$k_{RET} = \frac{1}{\tau}\left(\frac{R_F}{R}\right)^6 \tag{27}$$

where τ is the lifetime of the excited state of the donor and R_F is the Förster radius, a material parameter depending on the donor quantum yield and on the spectral overlap between the donor emission and the acceptor absorption. This theoretical framework can be extended to the case of a single dipole coupling to an array of dipoles, by spatially integrating over the acceptor arrays, which yield the formula

$$k_{RET} = \frac{1}{\tau}\left(\frac{R_F}{d}\right)^n \tag{28}$$

where d is the minimum donor-acceptor separation distance and n is a function of the dimensionality of the acceptor array: a thin line of dipoles yields $n = 5$, a thin layer yields $n = 4$ and a bulk volume yields $n = 3$ [51]. It is important to remember that this theoretical framework only applies to point-like dipoles, which may not be case in all

material systems, such as for extended Wannier Mott excitons. This assumption is however reasonable for QDs, and a good agreement between theory and experimental evidence was found for instance by Lunz et al. [52] in alternating QD layers.

2.6. RET optoelectronics

2.6.1. Hybrid solar cells

The idea of combining organic molecules and inorganic bulk semiconductors through RET to enhance the efficiency of solar cells was first envisioned by Dexter in 1979 [9]. In this scheme, the high absorption cross-section of organic materials is used to efficiently absorb the incoming solar radiation. The photogenerated excitons are then non-radiatively transferred through RET to an underlying semiconductor slab, capable of efficiently transporting and extracting carriers. Published at a time when silicon wafers represented most of the cost of solar panels, the hybrid concept presented in this paper nevertheless attracted very little interest and was soon forgotten. Significant studies of the underlying mechanisms were however undertaken during the same period. The review paper by Agranovich et al. *"Hybrid Resonant Organic-Inorganic Nanostructures for Optoelectronic Applications"* [45] includes an overview of the work carried out during that time and is a recommended read. One of the main focuses was to study the impact of placing an emitter close to a metallic surface on its photoluminescence behaviour. This provided a direct experimental demonstration of the Purcell effect, through which the spontaneous decay rate of an emitter depends on the photon mode density at the position of the emitter [53,54]. Of special interest here, careful theoretical studies of the behaviour of emitters in very close proximity ($\ll \frac{\lambda}{2}$) to a semiconductor slab were also carried on [55]. A very strong quenching of the photoluminescence intensity of the emitter was observed in this case, indicating the predominance of an additional non-radiative decay channel.

Experimental demonstrations of energy transfer from organics to semiconductor was presented early on in two papers by Alivisatos et al. in 1983 and 1987 [56,57], in which they demonstrated non-radiative energy transfer from pyridine thin films to bulk GaAs and Si by carefully modulating the separation distance between the materials. The concept of

hybrid solar cell remained seemingly dormant until 2007, when Lu et al. demonstrated energy transfer between a PbS QD epilayer and a single InGaAs/GaAs quantum well (QW) [49]. Dexter's scheme as initially intended, using an organic absorber, was "inadvertently" demonstrated a year later by Gowrishankar et al. [58]. While their work was focused on the study of charge separation at the interface between amorphous silicon and organic materials (P3HT and MEH-PPV), they found that non-radiative exciton transfer from the organics to a-Si:H was significant for P3HT-hybridized devices, with a 30% efficiency, and even dominated in the case MEH-PPV, with a transfer efficiency in excess of 80% [58]. The first demonstration that RET could be used to enhance the electrical photoresponse of a solar cell was obtained in 2009 by Chanyawadee et al. [47,48,59]. The hybrid devices investigated in these studies consisted of GaAs/AlGaAs multi quantum wells (MQW) *p*-*i*-*n* solar cells hybridized with CdSe/CdS and CdTe QDs. Before hybridization, deep channels were etched through the MQW region of GaAs diodes using a focused ion beam. This allowed the deposition of QDs in close proximity to the depletion region of the devices, where RET-injected excitons could be efficiently separated into useable carriers. The highly absorbing QDs could in this configuration directly contribute to the photocurrent and improve the performance of the device. A six-fold enhancement of the photocurrent conversion efficiency was obtained after hybridization. Implementation of a RET hybridization scheme in silicon nanowire photovoltaic devices was demonstrated during the same year by Lu et al. [60]. In this work, PbS QDs were used to improve the absorptivity of a planar array of silicon nanowires. They showed that RET-hybridization enhanced the photocurrent by 79%. More recently, in 2010 and 2011, Nguyen et al. demonstrated nonradiative energy transfer from CdSe/ZnS QDs to planar Si and to Si nanomembranes [50,61]. Both studies used SiO_2 films of varying thickness separating donor and acceptor to study the separation distance dependence of RET between QDs and Si. High energy transfer efficiencies (radiative and nonradiative) in excess of 80% could be demonstrated. RET was also used simultaneously to improve the efficiency of dye-sensitized solar cells (DSSCs) using so-called energy relay dyes (ERDs) [62]. In this scheme, ERDs absorb sunlight and non-radiatively transfer energy to the sensitizing dyes [63,64], in which the charge separation takes place. Since the ERDs do not participate in the charge transfer mechanisms, their energy levels do not need to be perfectly aligned, which allows a wide variety of dyes to be used. Hardin et al. demonstrated for instance an excitation transfer efficiency in excess of 90% between the ERD 4-(Dicyanomethylene)-2-

methyl-6-(4-dimethylaminostyryl)-4H-pyran (DCM) and the NIR sensitizing dye TT1. This enhanced the PCE of the device from 3.5% to 4.5%, by improving the device absorption in the blue-green wavelength range. Similar ERD approaches were also notably implemented in P3HT:PCBM polymer solar cells [65] and non-fullerene based organic solar cells [66], which yielded significant performance enhancements.

2.6.2. Hybrid LEDs

The utilisation of RET for colour conversion application in LEDs was first postulated by Agranovich, Basko and La Rocca, who proposed in the late 90s to non-radiatively transfer energy from a shallow QW to an emitting organic epilayer [40,67]. Such an approach would combine the efficient carrier injection properties of inorganic structure and the high luminescence quantum yield of organic emitters to obtained white and coloured LEDs. An early experimental demonstration of this scheme was achieved by F. Heneberger's group in 2006 [68], when they optically showed the possibility of efficient RET from a ZnO QW to a α-sexithiophene organic overlayer. Several studies then focused on transposing this scheme to InGaN QW, due to its industrial relevance. Works by Heliotis et al. studied RET between an InGaN QW to a F8DP epilayer and its dependence on the QW capping layer thickness [44,69]. In parallel, M. Acherman demonstrated that this colour conversion scheme could be extended to QD emitters using time-resolved spectroscopy, with early studies of RET from InGaN QW to CdS/ZnS core-shell QDs [41,70]. The temperature dependence study of RET between InGaN QWs and colloidal CdS QDs reported by S. Rohrmoser et al. demonstrated soon after that high energy transfer efficiencies (>60%) could be obtained with such hybrid configurations [71]. While all the experimental studies were done so far on single QWs using optical excitations, S. Chanyawadee showed in 2010 that non-radiative colour conversion could be extended to electrically excited MQW LEDs [42]. In this work, holes both deep (penetrating through the MQW region) and shallow (not reaching the active area) were etched into the structures, which were then hybridized with QD. A large enhancement of the colour conversion efficiency was demonstrated in the case of the deep-etched devices, where the QDs are in close proximity with the QWs, compared to shallow-etch reference case. In 2011, J. J. Rindermann showed that the RET transfer efficiency from a GaN QW to a F8BT overlayer was strongly temperature dependent, with a clear maximum around 150K [72]. This temperature dependence was attributed to a

balance between localized and free exciton populations in the QW, free exciton transfer being about one order more efficient than in the case of localized excitons. The author interestingly outlines that the excitonic localisation length of the QW could be tuned to enhance RET-mediated colour conversion at room temperature.

2.6.3. Conclusion

While the previous schemes historically studied focused on trying to separate photon absorption and charge transfer (for solar cells) or charge injection and photon emission (for LEDs), the author believes that more advanced schemes need to more carefully investigated. With quantum yields ever increasing and much improved photostabilities, quantum dots could in the regard prove very interesting materials to hybridize existing optoelectronic technologies. Specifically for solar cells, numerous effects, such as the internal light management and RET harvesting schemes developed in the next chapters, can be combined and tuned to enhance the properties of specific technologies. This is especially true for low-cost thin film devices, which can be manufactured using roll-to-roll processes that could easily integrate rapid QD spray deposition.

Chapter 3: Resonance Energy Transfer between PbS quantum dots and bulk silicon

3.1. RET silicon photonics

As mentioned in the previous chapter, QDs represent a promising material for optoelectronics applications. Amongst this family of materials, the large Bohr radius of lead chalcogenide QDs (PbS, PbSe, and PbTe QDs) make these colloidal nanocrystals ideally suited to study the strong confinement regime [73–75]. Their widely tuneable bandgap, ranging from 0.5eV to 2.5 eV, also made them good candidates for multi-exciton generation (MEG), a process in which a high energy photon ($E > 2E_g$) generates more than one exciton in the absorbing material [16,76]. While this phenomenon remains rather controversial, with several recent studies reporting discrepancies and lower conversion yield than initially measured [77–79], the prospect of overcoming the Shockley–Queisser limit and of obtaining quantum efficiencies in excess of 100% is a strong driving force in the field of quantum dot photovoltaics. In the simplest scheme, the large absorption cross section of PbS QDs in the visible can be leveraged by utilizing the material as a solar absorber. The near-infrared extension of their absorption spectra could also allow the efficient collection of low energy solar radiation, typically discarded by conventional solar cells. While they present very interesting absorption properties, extracting the photogenerated carriers from strongly confined QDs has proven challenging, even though significant progress has been previously reported [8,80]. Excitons generated in the PbS QDs could on the other hand be transferred to a bulk semiconductor such as silicon using RET. Such hybrid solar cell devices would be able to take advantage of the high absorption cross section of the QDs and of the good carrier transport properties of bulk crystalline p-n junctions [60].

Much effort has been focused on improving the passivation of QDs. Due to their large surface areas, surface properties are critical to the optical and electrical properties of the

QDs. The abrupt termination of the crystal lattice at the interface with the surrounding material can induce high densities of electronic trap states, which can dramatically impact the quantum yield of the QDs and the performances of QD devices. To mitigate this problem, a number of passivation techniques have been developed over the years, either by adding an additional semiconductor shell around the QDs (as discussed in Section 2.2) or by using organics ligand molecules and advanced surface chemistry techniques to passivate the surface of the QDs. These surface treatments can also limit particle aggregation, which can drastically lower their QY. Recent advancement in surface chemistry and passivation technology utilising tetrabutylammonium iodide (TBAI) have allowed largely improved PbS QDs photostabilities [8,80,81]. These air-stable particles were employed to make PbS QDs p-n junction PV devices, enabling record photon-conversion efficiencies in excess of 8% (compared to previous certified records of ~7%). This recent development has triggered a renewed interest in both the material and all-QD photovoltaic devices, with PCEs surpassing the “psychological” 10%-threshold in sight.

The QDs used in this chapter are thiol-passivated PbS QDs, properties of which have been previously extensively investigated [82]. The intensity of the photoluminescence (PL) of thiol-capped PbS colloidal QDs was shown to be enhanced for increasing temperature below 50K, but to decrease with increasing temperature above that threshold. The behaviour has been explained by introducing temperature dependent population of trapped excitons in the QD. No fine structure splitting was however derived from these observations. While the exact impact of surface states remains unclear, the fine exciton splitting in colloidal PbS QDs has been shown to be dependent on the surface area of the QDs, and thus on the diameter of the particles.

3.2. Material and methods

3.2.1. Time resolved spectroscopy

Time resolved measurements were performed using a streak camera system with a temporal resolution of about 30 ns. All QDs were excited non-resonantly at 400 nm with 150 fs pulses at a 27 kHz repetition rate. Samples were mounted on a cold finger helium flow cryostat and excited at an oblique angle (~30°) as illustrated in Figure 3.1. The

fluorescence was collected at normal incidence to the sample surface. Steady-state PL measurements were carried out using a fiber-coupled spectrometer equipped with a CCD detector with a 1 nm resolution. Absorption measurement were obtained in a UV-VIS-NIR spectrophotometer

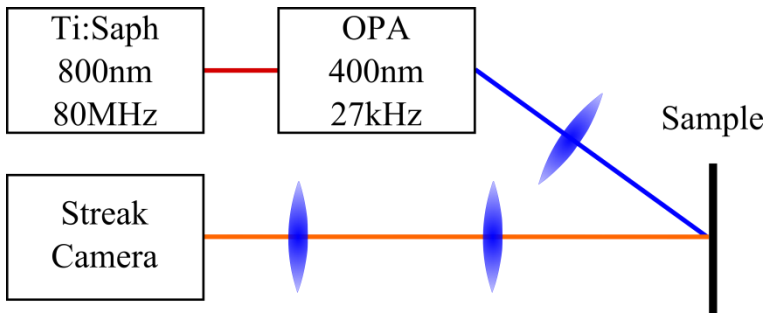

Figure 3.1: Time resolved photoluminescence experimental setup. Excitation is provided by a Ti:Saph femtosecond laser fed into an Optical Parametric Amplifier (OPA) which converts frequency doubles the excitation and decreases the repetition rate to 27kHz. The generated photoluminescence is collected by optics and directed to a streak camera.

The operating principle of a streak camera is depicted in Figure 3.2. These ultra-fast and ultra-sensitive photon detectors use a fast sweeping electric field to provide spatial and temporal information with sub-ps resolution. In these instruments, the light passes through a slit which is imaged onto the photocathode of the streak tube. At this point, the photons are converted into electrons, which are accelerated through the streak tube by a pair of electrodes and bombarded onto a phosphor screen. In the streak tube, a high voltage is applied to the sweep electrodes, which induces a high-speed spatial sweep of the electrons passing in between the electrodes. This allows electrons arriving at different times to be deflected at different angles and to be projected onto different areas of the micro-channel plate (MCP). The MCP then multiplies the electron population several hundred times before the electrons can reach a phosphor screen and be converted back into light. An image of the phosphor screen is finally acquired by a CCD camera to obtain usable images. An example of a streak camera image is displayed in Figure 3.2b. In this image, the horizontal and vertical axis respectively provide spectral and temporal information on the photoluminescence signal. The time decay curve is obtained through an horizontal average of the streak camera image.

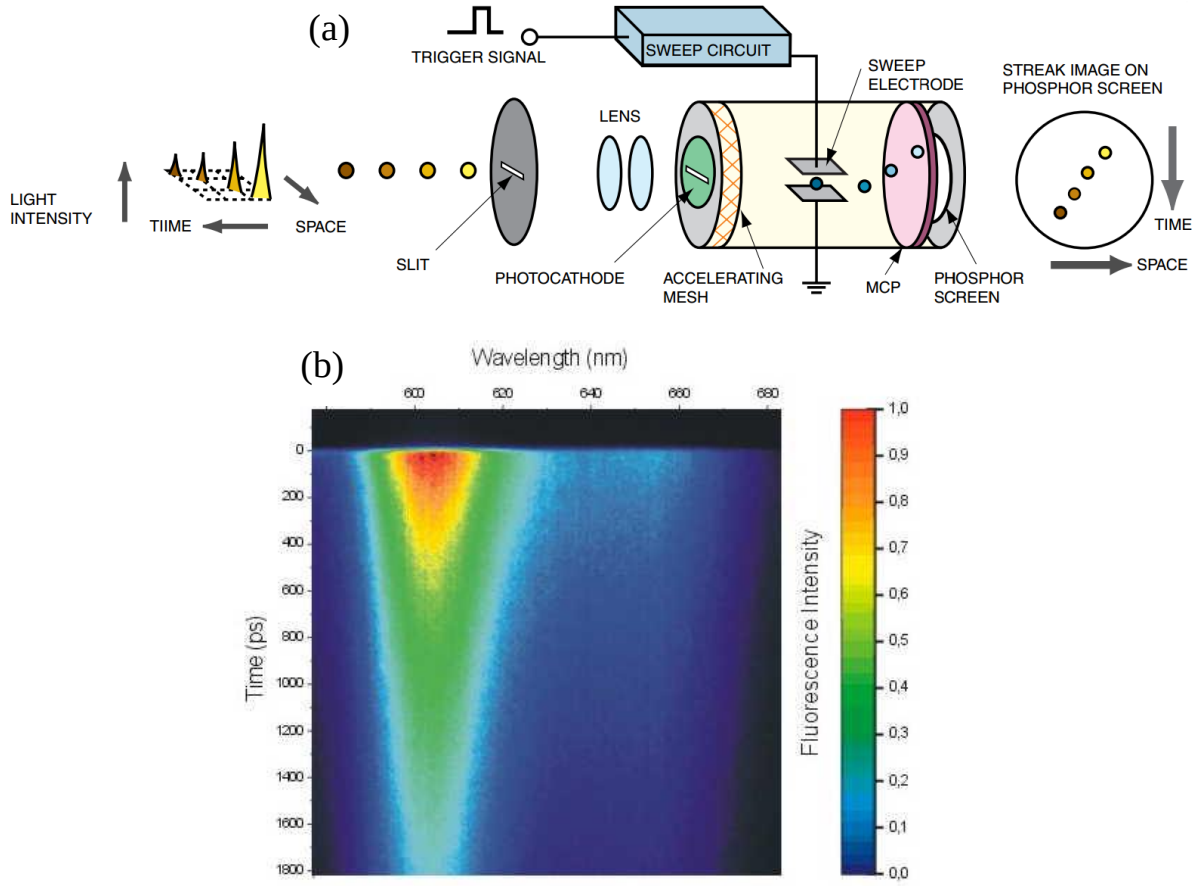

Figure 3.2: (a) Operating principle of a streak camera and (b) typical streak camera image. (Adapted from [83]**)**

The decay dynamics of the PbS QDs was found to exhibit a significant non-single exponential behaviour, and the decay curves were satisfactorily fitted with a bi-exponential function:

$$I(t) = A_1 e^{-k_1 t} + A_2 e^{-k_2 t}. \tag{29}$$

The average decay rate was calculated using the equation

$$< k >= \frac{A_1\tau_1 + A_2\tau_2}{A_1\tau_1^2 + A_2\tau_2^2} \tag{30}$$

where $\tau_1 = \frac{1}{k_1}$ and $\tau_2 = \frac{1}{k_2}$ are the lifetimes of the two exponential components in the above equation.

3.2.2. Fabrication

Thiol-passivated PbS nanocrystals were synthesized following a slight modification of the previously reported method[21]. The devices studied in this work consisted of PbS QDs deposited on silicon substrates with different thicknesses of silica (SiO_2). To produce the silica spacers on the silicon samples, a 100 nm silica thin film was thermally grown on a silicon wafer in a furnace. This wafer was then diced into 20x20 mm^2 samples. Each sample was finally etched down using reactive ion etching to obtain the required spacer thicknesses. The final SiO_2 thickness was measured using ellipsometry.

3.3. Size and temperature dependent optical properties

3.3.1. Room temperature optical properties in solution

The absorption and emission spectra of oleic-acid passivated QDs of 6 different diameters were measured using a UV/visible spectrophotometer and a fibre-coupled CCD spectrometer, respectively, and are presented in Figure 3.3. The particle diameters were measured using a zetasizer. As expected from the theory, as the size of the QD decreases, the confinement contribution to the exciton energy increases, which blue-shifts the absorption spectra. The maxima of the first exciton absorption peak is found to located at ~2.08, 1.73, 1.50, 1.43, 1.35 and 1.24 eV for QDs of diameter 2, 2.3, 3, 3.5, 3.6 and 3.8 nm, respectively. The PL emission spectra show the same size-dependent behaviour as the absorptions spectra, with emission peaks of 1.61, 1.45, 1.37, 1.32 and 1.27 eV for QD of diameter 2, 2.3, 3, 3.5 and 3.6 nm, respectively. The emission spectrum of the 3.8 nm QDs could not be measured, due to the poor responsivity of the detector near the silicon bandgap. The Stokes shift energy of the QDs, mentioned in Section 2.2.3, is plotted as an inset in Figure 3.3b as a function of the diameter of the QDs. In lead salt QDs, the lowest excitonic manifold occurs at four equivalent L-points in the Brillouin zone. The electron-hole exchange interaction and spin-orbit coupling force a splitting of the energy levels, and in particular of the lowest 1S-1S state. This leads to the formation of a dark state (singlet) and of a 3-fold degenerate bright exciton state (triplet), separated by an energy gap [73]. As the diameter of the QD decreases, quantum confinement and the electron-hole

wavefunction overlap are enhanced, which increases the dark-bright splitting and thus the Stokes shift.

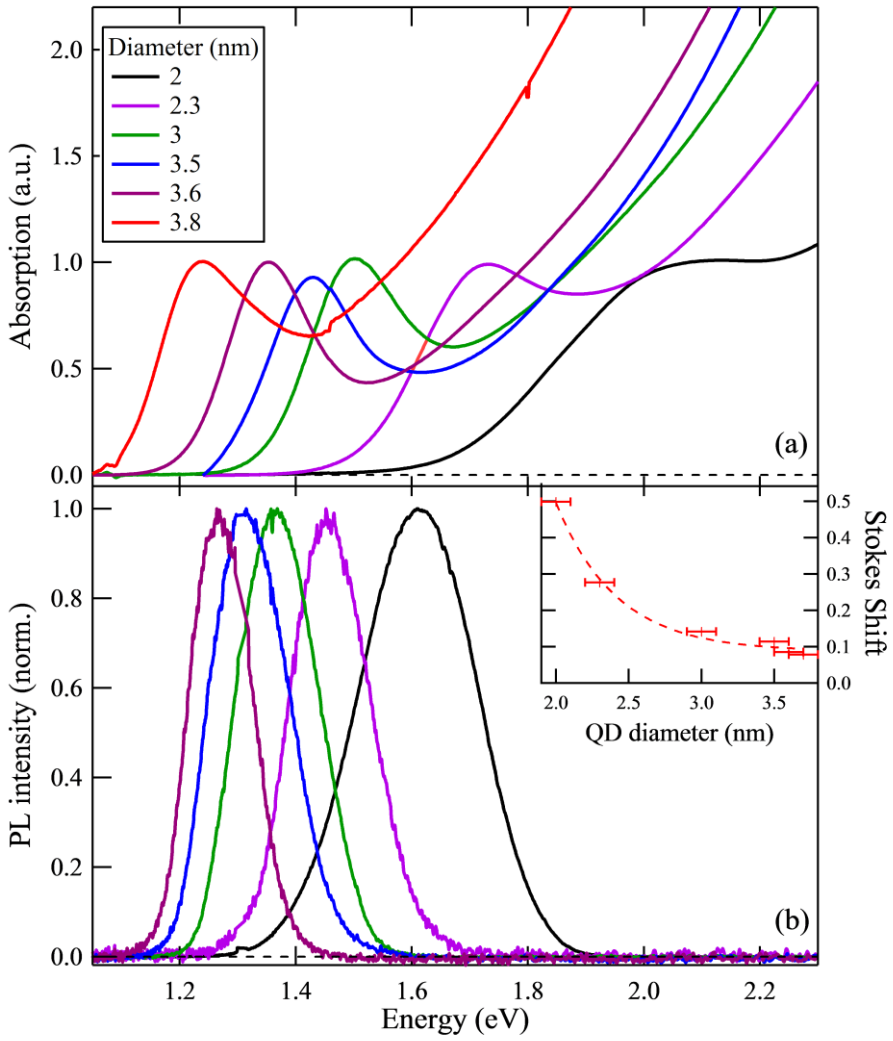

Figure 3.3: Absorption (a) and photoluminescence (b) spectra of PbS QDs of different sizes. Inset: Stokes shift energy as a function of the diameter of the QDs.

The PL decay curves of PbS QDs of various sizes in solution are presented in Figure 3.4a. The decays were fitted as previously described (Equation 29), and the average decay rate is plotted in Figure 3.4b. The decay rate of the QDs is found to be very size dependent, with a rapid increase below 3 nm. As the size of the QDs decreases, the $\left|U_{(o)}\right|^2$ factor describing the electron-hole wavefunction overlap in equation (18) increase, which increases the

oscillator strength f. As a first approximation, the oscillator strength of the first excitonic transition (f_1) is inversely proportional to the volume of the QD, through the equation

$$f_1 = f_{ex}\frac{\pi a_B^3}{V} = \frac{3}{4} f_{ex}\left(\frac{a_B}{r}\right)^3 \tag{31}$$

where f_{ex} is the exciton oscillator strength of the bulk, V and r are the volume and radius of the QD (assumed spherical) and a_B is the Bohr radius. Since the radiative decay rate k_{rad} is proportional to the oscillator strength, the dependence $k_{rad} \propto r^{-3}$ is also verified.

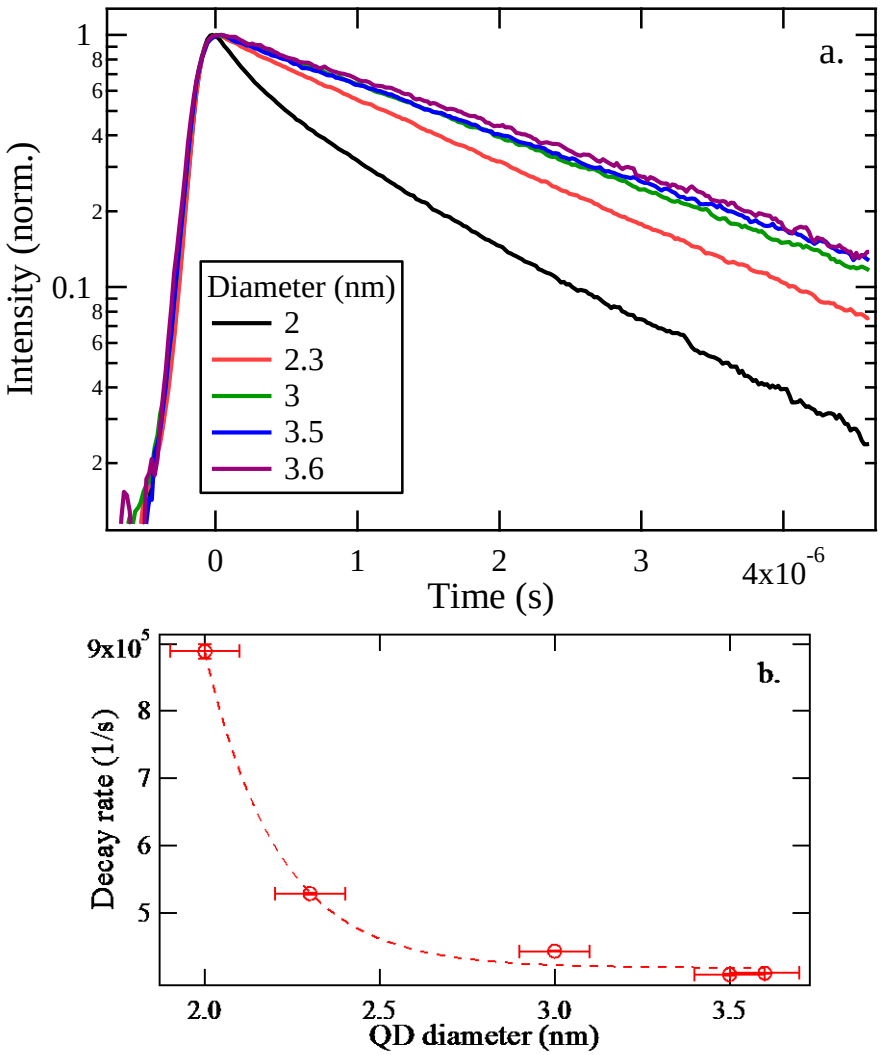

Figure 3.4: (a) Time-resolved photoluminescence decays of QDs of various sizes. (b) Fitted decay rate as a function of QD diameter.

3.3.2. Temperature dependence study of PbS QDs on glass

Time-resolved spectroscopy measurements were performed on oleic acid capped PbS QDs spincoated on glass substrates placed inside a helium cryostat. The concentration of the QDs was kept low (~1 mg/mL) so as to avoid inter-QD interactions. The PL decays were again found to be bi-exponential, and analysed as previously described. This bi-exponential behaviour is attributed to the presence of dark and bright recombination channels, as reported in [84]. PL intensities were extracted by integrating steady-state spectra of the QD emission. The PL decay rate and intensity are presented as a function of temperature in Figure 3.5 for QDs of diameter 2.3, 3, 3.5 and 3.6 nm.

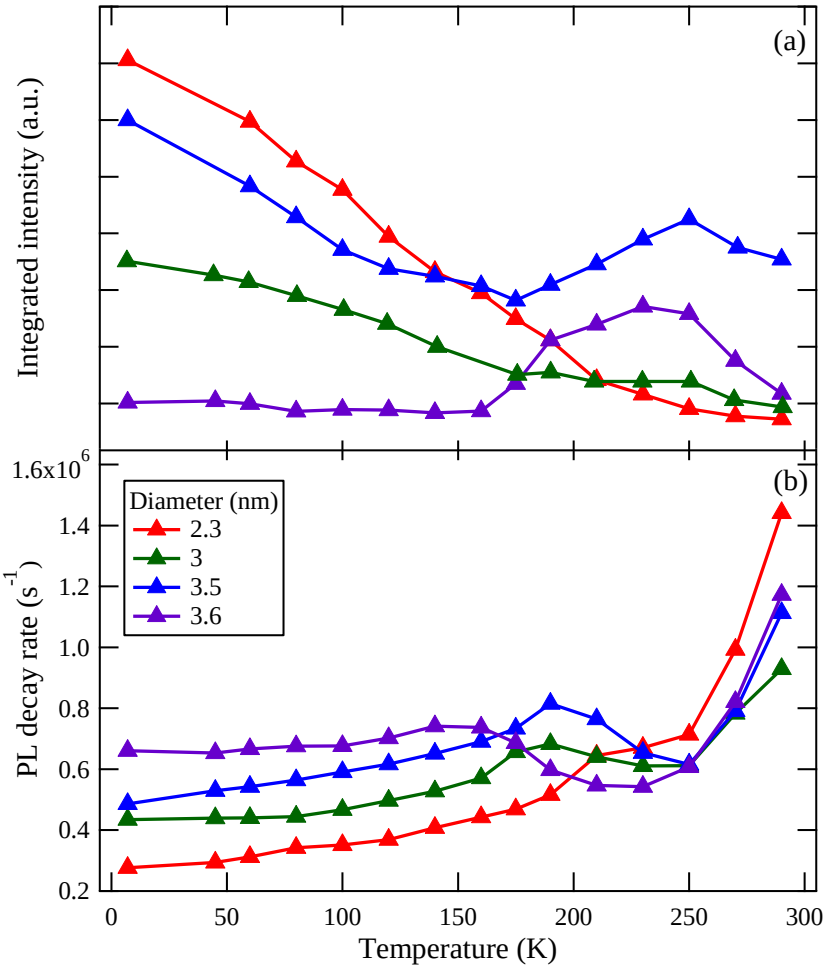

Figure 3.5: PL intensity (a) and decay rate (b) of PbS QDs of various sizes as a function of temperature.

A non-monotonic temperature dependence can clearly be observed for larger QDs. This behaviour becomes gradually more monotonic for decreasing particle sizes, with 2.3 nm QDs displaying virtually monotonic temperature dependences. Three temperature regimes can be identified: a low temperature regime below ~180 K, and intermediate temperature regime in the ~180 to ~250 K temperature range and a high temperature regime above ~250K. This behaviour was modelled in detail in [84] by P. Andreakou and only a short description of the phenomenon is provided here. In this model, the fine structure of the lowest exciton state is represented by a bright and a dark level, with radiative recombinations rates k_B and k_D respectively (see Figure 3.6). The energy gap ΔE separating these two levels is dependent on the size and shape of the QD, and is in the range of a few meV [73,84]. An in-gap trap state representing surface states is also present. An energy barrier is present between the bright state and the trap state to avoid complete quenching of the bright state, which renders the trap state thermally activated.

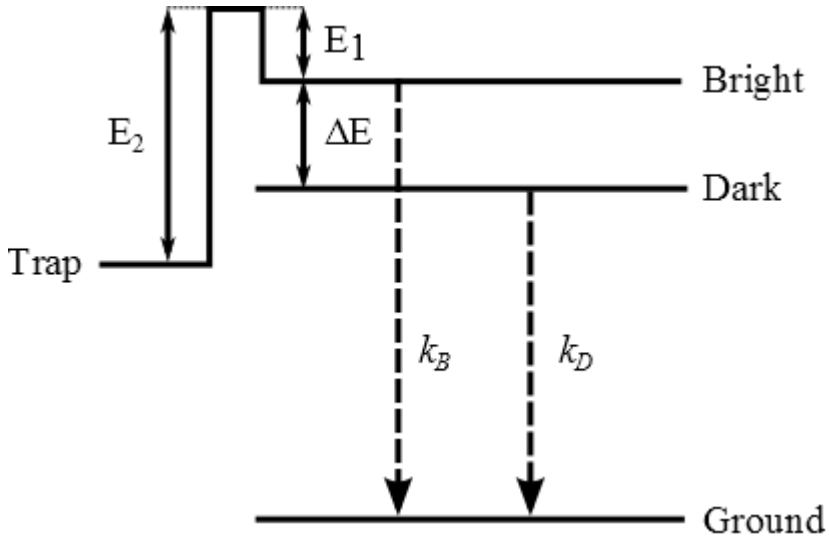

Figure 3.6: Schematic representation of the exciton relaxation process in PbS QDs.

The low temperature regime (< ~180 K) is characterised by a decrease in intensity and an increase in PL decay rate with increasing temperature. The increase of the decay rate is attributed to the dark-bright splitting of the lowest exciton state, as previously reported [85]. As the temperature increases so does the phonon population. This allows the bright state to be gradually more and more populated, thus increasing the overall decay rate of the QDs. The intensity increase in this regime, while counter-intuitive in this model, is a commonly observed phenomenon, attributed to trap states [85]. Carriers with energy $k_B T > E_1$ are quenched on surface trap states, thus decreasing the overall number of

excitons radiatively recombining. This phenomenon also explains the strong size-dependence of the intensity variations: small QDs, such as the 2.3 nm QDs, display a stronger quenching of the intensity than larger ones, such as the 3.5 nm QDs, their higher surface to volume ratios making them more sensitive to surface traps. In the intermediate temperature regime, the average decay rate of the QDs decreases and the PL intensities gradually recovers. The effect is again found to be most predominant for larger QD. Above a temperature threshold (~180 K), the thermal energy of the trapped carriers is sufficient to overcome the E_2 energy barriers, repopulating the dark and bright states and increasing the PL intensity. Finally, in the high temperature regime (> ~250 K), the PL intensity is found to be gradually quenched for increasing temperature, which indicates the presence of a non-radiative recombination channel from the trap state, not represented in the model in Figure 3.6.

3.4. Donor-acceptor separation dependence of resonance energy transfer

Oleic acid capped particles with an absorption exciton peak at ~800 nm were spin-coated onto substrates consisting of SiO_2 thin films of various thicknesses on bulk Si (see Figure 3.7a). The QDs, with a 1s emission peak around 900 nm, were chosen so as to allow RET between the QDs and Si. Their diameter was found to be 2.9 nm, using a zetasize. Their strong absorption in the visible spectral range provides a good overlap with the solar spectrum, which makes them ideal as solar absorbers. Their absorption and photoluminescence spectra are displayed in Figure 3.7b. The efficiency of RET depending strongly on the separation distance between the donor and the absorber, the presence of a SiO_2 spacer of variable thickness allows the gradual activation of the RET channel. This additional channel quenches the PL of the QD and accelerates its PL decay. Studying the dependence of the QD dynamics on the spacer dynamics can thus provide a strong evidence of the presence of RET between the QDs and bulk silicon.

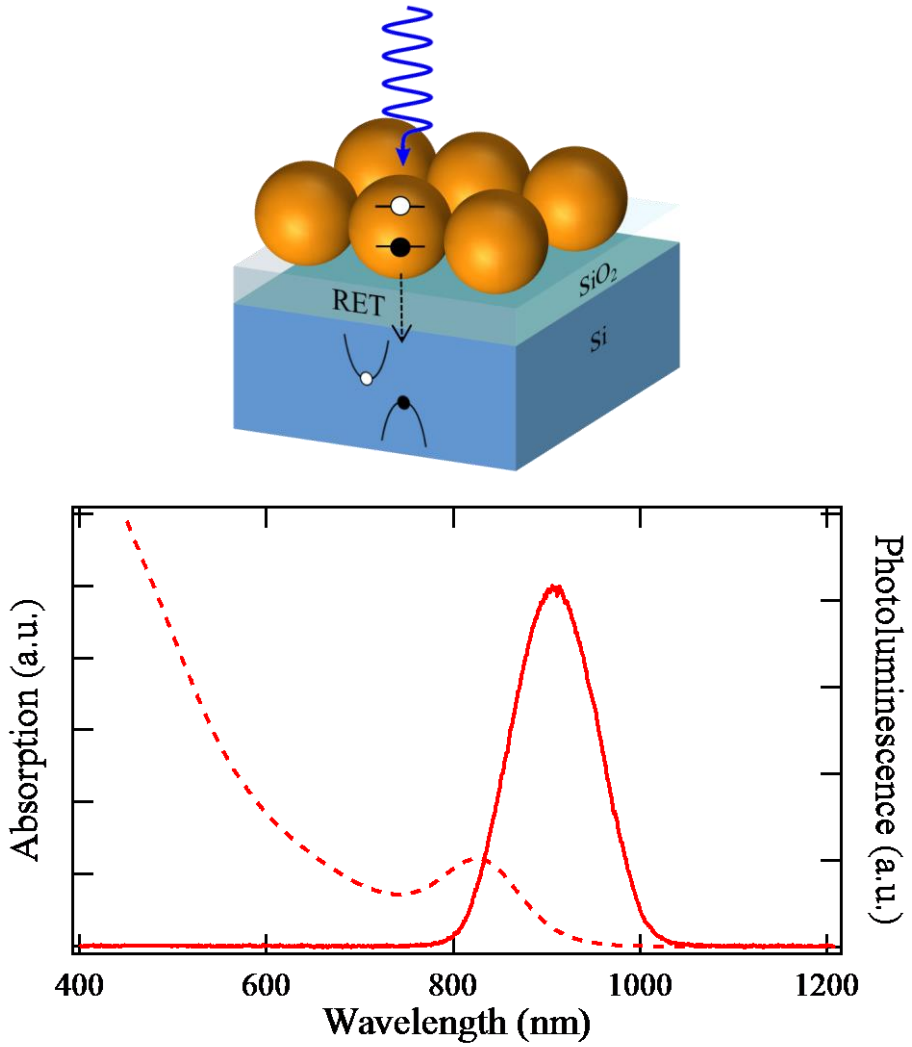

Figure 3.7: (a) Schematic representation of energy transfer between PbS QDs and bulk Si. (b) Absorption (dashed) and photoluminescence (continuous) spectra of the PbS QD chosen for this study.

Time-resolved spectroscopic measurements of the QD photoluminescence were carried on as previously described for SiO_2 thicknesses ranging between 5 and 56 nm. The decay rates were again found to be non-single exponential, and were fitted with a double exponential to extract an average decay lifetime (see Section 3.2.1). The decays of PbS QDs on glass and on 5 nm and 8 nm SiO_2 spacers are displayed in Figure 3.8a. A clear acceleration of the decay dynamics as the QD/Si separation distance decreases is observed. The average lifetime of the QDs is plotted in Figure 3.8b as a function of the spacer thickness. As expected in the presence of a RET decay channel, the PL decay rate increases rapidly for decreasing separation distances below 12 nm. The decay rate is found to be constant above that threshold, with values comparable to the decay rate of PbS QDs on glass (blue dashed line). The observed acceleration in the lifetimes of PbS QDs for short separation distances is a strong evidence of RET from the QDs to the bulk silicon. The data was fitted with a power law to extract the separation distance dependence of the decay rate of the QDs:

$$k(t) = A + B * t^K \tag{32}$$

where A and B are fitting paremeters, K is the power factor and t is the thickness of the spacer layer. The fitted curve is displayed in Figure 3.8b. A value of K of -2.6 ± 0.52 was found, in good qualitative agreement with the value of -3 predicted by the theory described previously in the case of RET between a dipole (here a QD) and a bulk semiconductor (silicon) [67]. The constant A, corresponding to the QD decay rate for an infinitely thick spacer layer, is found to be 1.08 s^{-1}, in good agreement with the experimental value of 0.98 s^{-1} measured for the QDs on glass. This is also in agreement with separation distance studies of RET from a dye molecule to bulk silicon [56].

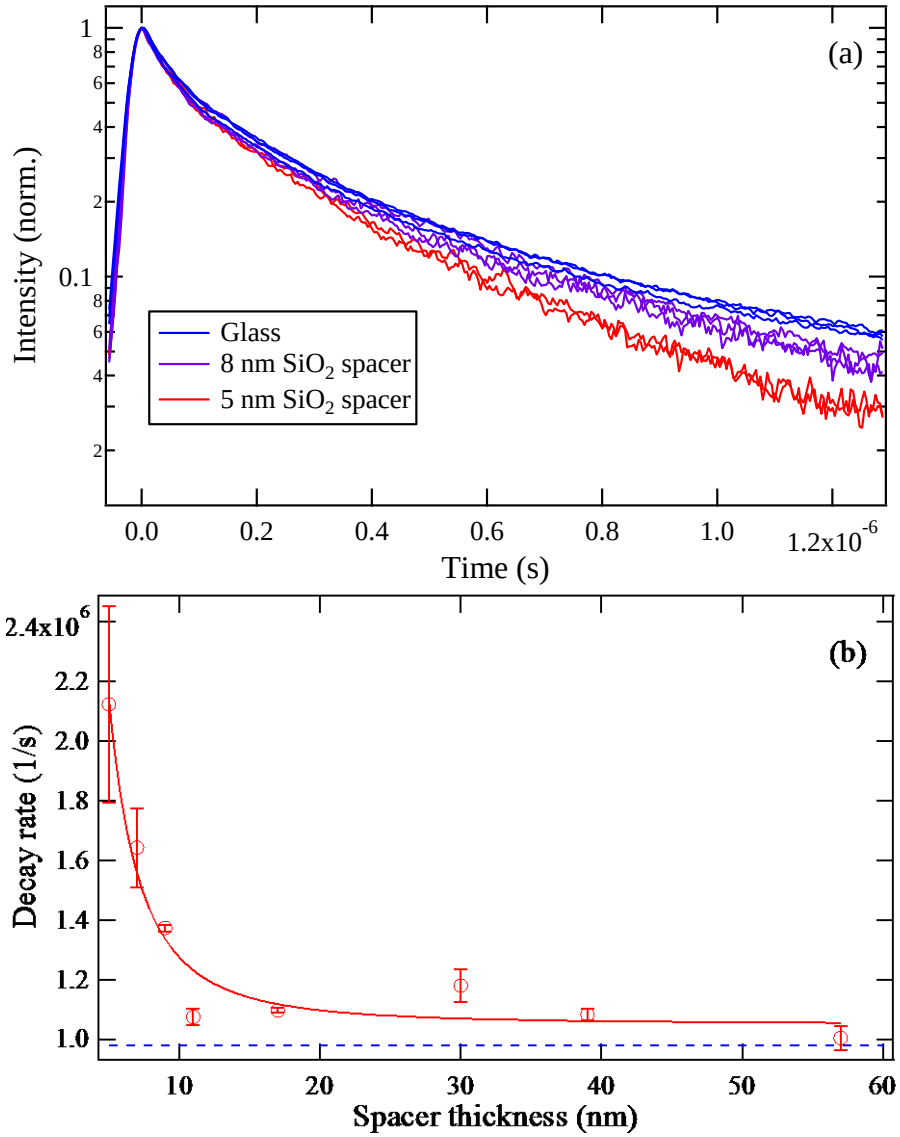

Figure 3.8: (a) Time-resolved photoluminescence decays of PbS QDs on glass (blue), on a 8 nm SiO_2 spacer (purple) and on a 5 nm SiO_2 spacer (red). (b) Average decay rate of PbS QDs as a function of the spacer thickness. The blue line indicates the decay rate of the QDs on a glass substrate.

3.5. Temperature dependence of energy transfer in oleic acid capped PbS quantum dots/silicon hybrid structures

To characterise the temperature dependence of RET between PbS QDs and bulk silicon, temperature dependent time-resolved PL measurements were performed on PbS QDs spincoated on a glass substrate, on a 5 nm SiO_2 spacer and on a 20 nm SiO_2 spacer on Si.

The average decay rate is plotted as a function of temperature for these three samples in Figure 3.9. The temperature dependence of the decay rate of the QDs exhibits a similar behaviour on all three substrates. This behaviour was described in details in Section 3.3.2, and is attributed to the fine structure of the lowest exciton state of the QDs. The decay rate of QDs on a 20 nm spacer (black markers) remains lower than on a 5 nm spacer (red markers) across the 6 to 290 K temperature ranges, and is close to the decay rate of QDs on glass (blue marker). The dynamics of the QDs on a 5 nm spacer layer includes an additional decay channel compared to both the 20 nm spacer and the glass substrates, which was demonstrated previously to be RET between the QDs and the underlying Si. Since it was shown that the decay rate remains constant for spacer thicknesses above 12 nm, RET between the QDs and Si is assumed to be completely supressed for a 20 nm spacer. The good match with the decay rates of the QDs on glass further corroborates this assumption.

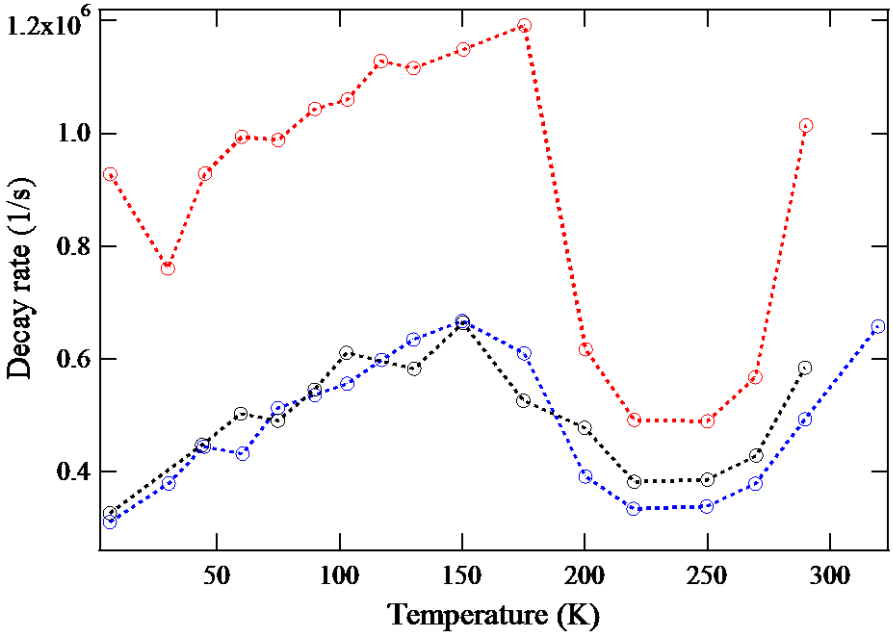

Figure 3.9: Average decay rate of PbS QDs deposited on a glass substrate (blue markers), on a 5 nm SiO_2 spacer (red markers) and on a 20 nm SiO_2 spacer (black markers) as a function of temperature.

The RET rate for a 5nm separation distance between donor and acceptor can be extracted using the formula:

$$k_{5nm} = k_{20nm} + k_{RET} \tag{33}$$

where k_{5nm} is the decay rate of PbS QDs deposited on the 5 nm SiO_2 spacer sample,k_{20nm} is the decay rate of PbS QDs deposited on the 20 nm SiO_2 spacer sample and k_{RET} is the RET rate between the QDs and silicon. The RET efficiency is calculated using the equation:

$$\eta_{RET} = \frac{k_{RET}}{k_{5nm}} \tag{34}$$

where η_{RET} is the RET efficiency. The RET rate is plotted in Figure 3.10: RET rate for a 5nm spacer as a function of temperature. as a function of temperature. It is found to follow a trend similar to the temperature dependence of the decay rate of the PbS QDs on glass. This non-monotonictemperature dependent behaviour of the PbS QDs photoluminescence results in an increase of RET rate close to room temperature, with a room temperature RET rate comparable to the values at low temperatures. The RET efficiency was calculated to be 44% at room temperature and 57% at 5K.

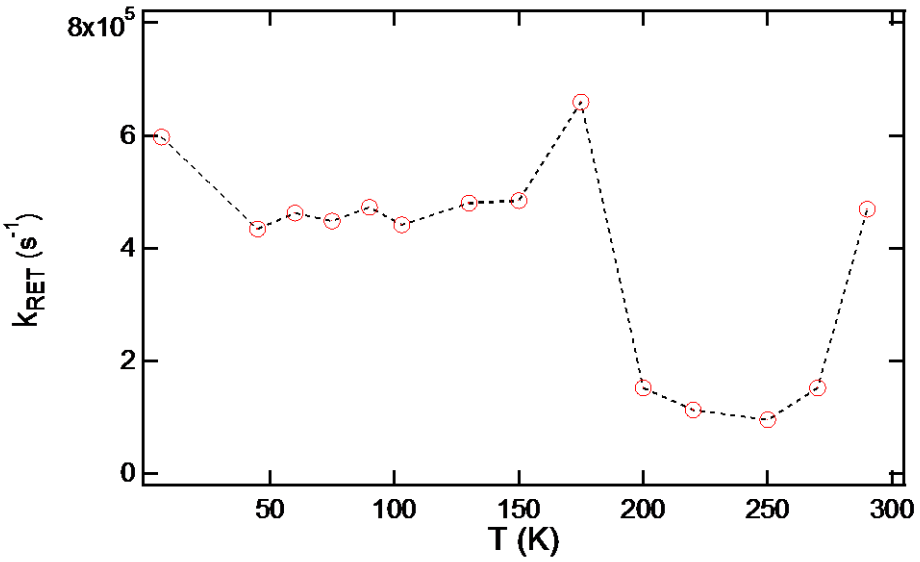

Figure 3.10: RET rate for a 5nm spacer as a function of temperature.

3.6. Conclusion

Efficient resonance energy transfer from PbS QDs to bulk silicon was demonstrated. The PL decay rate of the QDs was found to be significantly quenched for spacer thicknesses below 12 nm and the RET rate was found to be roughly proportional to the inverse cube of

the separation distance between the PbS QDs and the silicon. Time-resolved photoluminescence measurements for a range of temperatures were also presented for PbS QDs deposited on glass and silicon with 5 nm and 20 nm spacer thicknesses substrates, showing a strong non-monotonic behaviour previously described in the literature. The good match between the solar spectrum and the absorption spectrum of PbS QDs make these QDs especially interesting for photovoltaic applications. The large absorption cross section of the QDs makes them ideal visible light absorbers, but at the cost of typically low carrier extraction efficiencies. We demonstrated that resonance energy transfer was a viable candidate to activate exciton transfer between such absorbers and bulk semiconductors.

In this framework, associating PbS QDs with bulk silicon and using RET as a transfer mechanism could allow the fabrication of hybrid photovoltaic devices that combine the excellent absorption properties of quantum dots with the high carrier mobility and extraction efficiency of bulk semiconductors. A previous study by H. Nguyen at al. [50] demonstrated that colloid QDs could be used to hybridize a thin Si nanomembrane, by strongly enhancing the overall absorption of the semiconductor structure. An energy transfer efficiency of 85% was demonstrated. These CdSe/ZnS QDs were however tuned to emit in the visible and thus could not absorb the red/near infrared parts of the solar spectrum. Using a blend of high quality visible (such as CdSe/ZnS) and near-infrared (such as PbS) QDs could provide an optimum structure, potentially improving the overall transfer efficiency across the solar spectrum. While many high energy transfer efficiencies were reported ([47,50,84]), it is important to note that a paper by M. T. Nimmo et al. ([86]) is questioning the validity of the underlying analysis. In this work, a theoretical framework was developed to model energy transfer between emitters and a bulk semiconductor. The model includes both radiative and non-radiative energy transfer terms. They claim that these emitters can also efficiently radiatively couple to waveguiding modes in the semiconducting slab, modifying the decay dynamics of the emitters.

3.7. Contributions to the work

The optical measurements were carried out by the author and Peri Andreakou, who also developed the modelling of exciton dynamics in PbS QDs. The analysis of the time-resolved spectroscopy data was done by the author. The SiO_2 spacer samples were fabricated by the author. The QDs were produced by Maria Bernechea and Gerasimos Konstatos at ICFO, Barcelona.

Chapter 4: Resonance energy transfer mediated luminescent down-shifting in high efficiency InGaP solar cells

4.1. Introduction

The spectral mismatch between the response of a solar cell and the solar spectrum represents the largest loss factor for all photovoltaic technologies. While sub-bandgap photons cannot be absorbed by the semiconducting material, the excess energy of high energy photons is lost via non-radiative relaxation of the carriers in the form of heat. These fundamental losses limit the theoretical maximum photon conversion efficiencies (PCE) efficiency to 34% for an optimal 1.34eV bandgap. The best experimental single junction solar cells achieve conversion efficiencies around 30% under one sun illumination [87]. These high experimental efficiencies are typically achieved through advanced front surface optimization of the solar cells, to maximize the collection efficiency of the high energy photons absorbed at the surface of the devices. Such optimization techniques prove in many cases too costly for large-scale industrial production, and typical mass-produced solar modules only reach conversion efficiencies of around 20% [88]. Inefficient use of high energy photons thus remains an important limiting factor for commercial solar cells.

High performance solar cells can exhibit very high PCEs, with demonstrated values in excess of 40% [89–91] and even reaching 44.7% [92]. These solar cells are typically triple-junction devices, with a Ge bottom cell absorbing mostly near-infrared photons between 0.65 eV and 1.4 eV, a middle InGaAs cell principally absorbing red photons in the 1.4-1.86 eV range and an InGaP top cell harvesting blue and UV photons above 1.86 eV. A thin window layer of AlInP is typically deposited above the top cell to act as a passivation layer. This layer minimizes non-radiative surface recombination of the excitons created near the surface of the top cell by creating an energy barrier for the minority carriers (see Figure 4.1a). While improving the extraction efficiency in the top cell, the window layer

also acts as an absorber for high energy photons, since AlInP is an indirect semiconductor with a bandgap around 2.2 eV [93]. The carriers created in the window layer tend to recombine through surface states, which reduces their extraction efficiency [94]. This effect lowers the quantum efficiency of the solar cell in the high energy region of the solar spectrum. Figure 4.1b presents the wavelength dependence of the absorptivity of a 30nm AlInP window layer, calculated with refractive index extracted from [88], and of the typical IQE of a single p-n junction InGaP PV device, which shows that the IQE drop in the blue and UV parts of the spectrum correlates with a rapid increase of the absorptivity of the window layer at shorter wavelengths. A typical 30nm window layer can in this way induce a loss of more than 5% of the incident solar power.

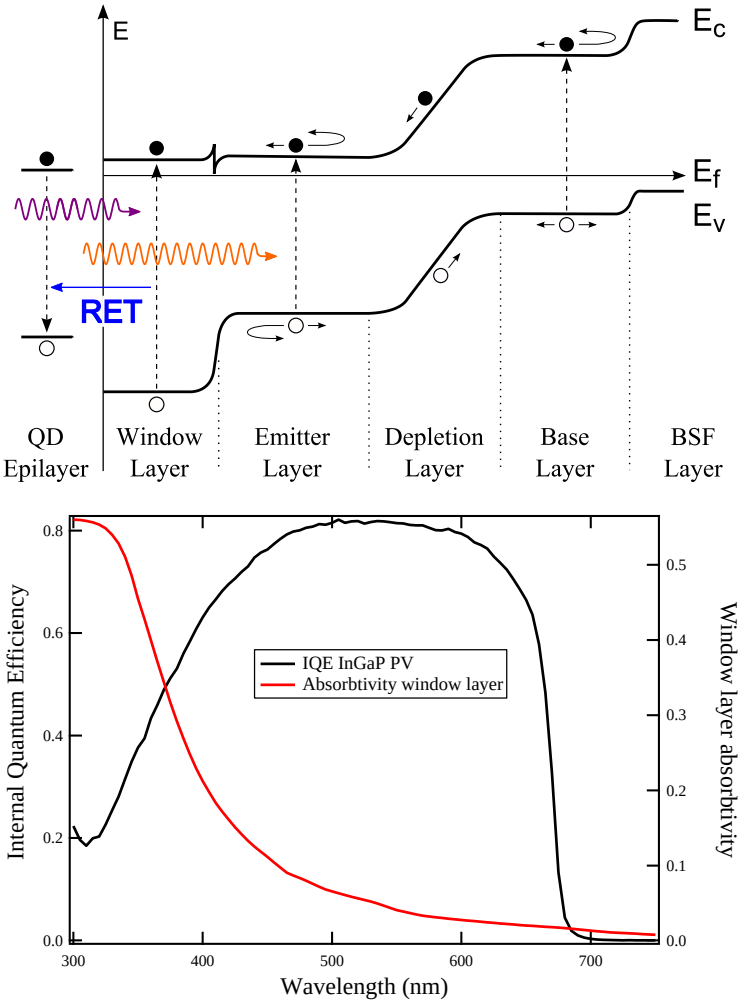

Figure 4.1: (a) band diagram of the hybrid InGaP solar cell and (b) wavelength dependence of the absorptivity of a 30nm AlInP layer and of the typical IQE of a single-junction InGaP PV device.

A simple approach to achieve a better utilization of high energy photons is luminescent down-shifting (LDS) of the solar spectrum. In this scheme, short wavelength (high energy) photons are absorbed by a luminescent material which re-emits at a more favourable higher wavelength. Organic dyes [88,95–97] and colloidal quantum dots (QDs) [98–102] have been considered as LDS materials for a wide range of photovoltaic technologies. The high absorptivity at shorter wavelengths, narrow emission spectral range, good absorption and emission tunability, high absorption cross-section and high photoluminescence quantum yield [7,103] of colloidal QDs make them ideal candidates for LDS layers [104]. Large scale LDS films can be readily deposited using low-cost techniques such as spray coating and do not significantly add to the cost of the final modules, thus maintaining the cost competitiveness of the modules.

To harness the carriers captured in the passivation layer, we deposit an epilayer of colloidal semiconductor QDs and use resonance energy transfer (RET) to funnel indirect excitons from the passivation layer to the QD epilayer. RET is a non-radiative electrodynamic process occurring between a donor (in our case the AlInP layer) and an acceptor (QDs in this study). Photons absorbed by the donor create excitons that non-radiatively transfer to the acceptor through dipole-dipole interaction. Since AlInP is an indirect semiconductor, resonance energy transfer of excitons from the AlInP layer to the direct bandgap InGaP p-n junction is forbidden by momentum conversation. The indirect bandgap nature of AlInP also forbids radiative recombination of the carriers generated in this layer, which prevents luminescent down-shifting in the window layer. On the contrary, quantum confinement in the QDs breaks the translational symmetry invariance, relaxing the constraints imposed by momentum conservation. This allows for RET between the indirect bandgap window layer and the epilayer of QDs. The QDs are tuned to emit below the bandgap of the window layer, optically pumping the p-n junction, where the photogenerated carriers can be efficiently extracted. Since AlInP has a much higher refractive index than air (n_{AlInP}=3.00 at 585nm) [93], most of the QD emission couples into the cell. This scheme allows us to circumvent the window layer bottleneck for high energy photons, leading to a 2% absolute increase in photon conversion efficiency.

4.2. Materials and Methods

4.2.1. Fabrication

The InGaP solar cells used in this work were grown by low pressure metal organic chemical vapour deposition (MOCVD) in a Veeco E475 epitaxial growth reactor. The growth took place at a temperature of 650℃ and a pressure of 40 Torr on Si-doped GaAs wafers with a (100) 2 degree off to [110] orientation. The structure consists of a n++/p++ GaAs tunnel diode, a 50 nm $Al_{0.7}Ga_{0.3}As$ back surface field (BSF) layer, that provides an energy barrier for the minority carriers, a 1500 nm p-$In_{0.5}Ga_{0.5}P$ base layer, where most of the carriers are generated, a 40 nm n-$In_{0.5}Ga_{0.5}P$ emitter layer and a 30 nm $Al_{0.5}In_{0.5}P$ window layer, that provides an energy barrier for the majority carriers. Gold bottom and top contacts were deposited using electron beam evaporation, and the final devices were microbonded to circuit boards for analysis. The active area of the devices is 16.24 mm^2. Figure 4.2 presents a schematic representation of the layer stack of the device, along with a picture of the final device micro-bonded to a carrier PCB. The QDs are Trilite^{TM} 585 (here QD-585) and Trilite^{TM} 665 (here QD-665), procured from Cytodiagnostics. These QDs are oleic acid capped CdS_xSe_{1-x}/ZnS core/shell colloidal semiconductor quantum dots, with 1s emission wavelengths of respectively 585+/-15nm and 665+/-15nm and 1s absorption peaks of respectively 560nm and 660nm indicating a respective Stokes shift of 9.5meV and 1.4meV. QDs epilayers were deposited using dynamic spincoating at 1500RPM. The film thickness was estimated to be 10nm using a M-2000 J.A. Woollam multi-angle ellipsometer. Ellipsometry measurement were taken in the 193-1690nm for 3 different angles, and the data was fitted using a B-spline model in the software CompleteEase. Devices were fully characterized before and after QD deposition, to discard any possibility of sample to sample disparities.

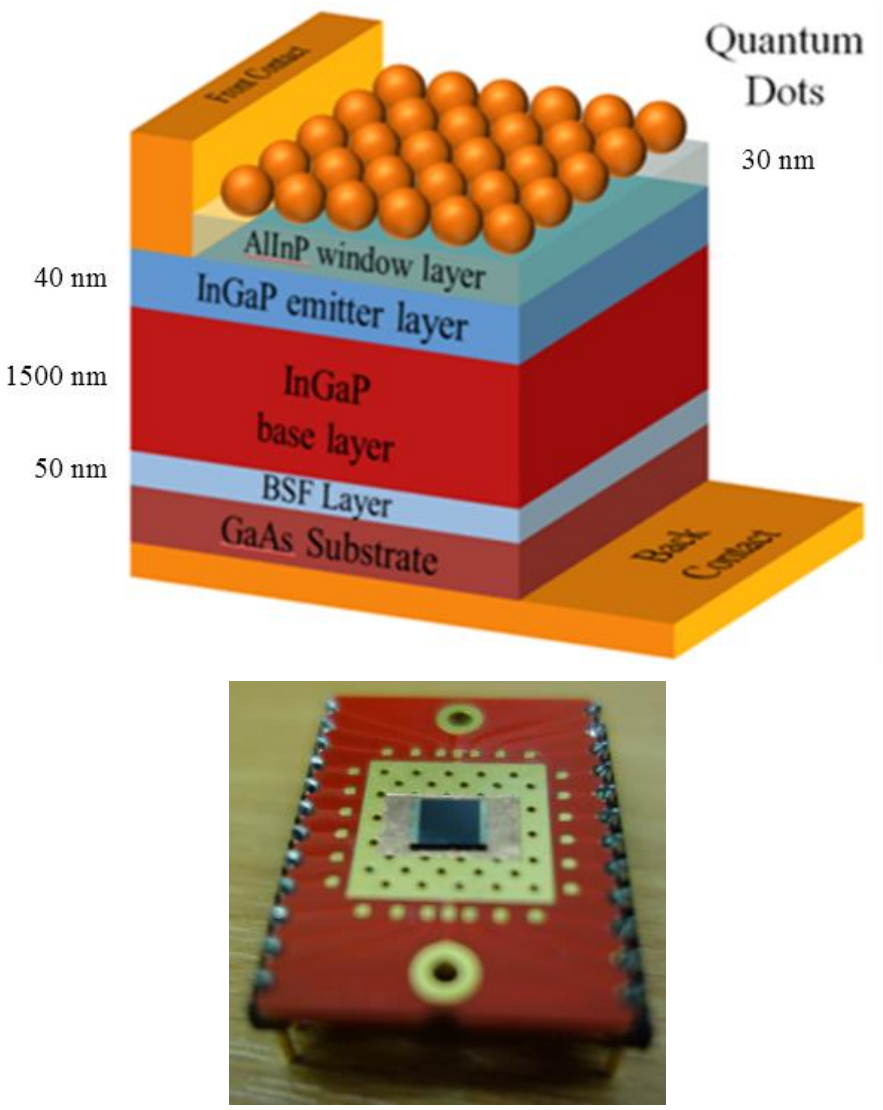

Figure 4.2: (a) Schematic representation of the hybridized InGaP PV device and (b) photograph of a device micro-bonded to a carrier PCB.

4.2.2. Characterization Methods

Absorption spectra were obtained using a Jasco V-570 UV/VIS/NIR spectrophotometer. The complex refractive index of the QDs spin-coated on glass was measured using ellipsometry. The complex refractive index of AlInP was obtained from the literature. [93] The EQE of the devices were obtained using a Bentham PVE300 PV Characterization System, equipped with a monochromatic probe source (dual Xenon/quartz halogen light source and TMc300 monochromator). The EQE was measured with a 25 mm^2 focused beam, for wavelengths between 300 and 1100 nm. The system was calibrated with a standardized silicon photodetector (Bentham DH-Si) before every measurement. The

absorptivity of the structure was measured in an integrating sphere using the same excitation source, by placing the sample at the reflectance port of the sphere. Every run was preceded by a calibration measurement, where the sample was replaced by a scattering surface. The beam size was in this case kept smaller than the sample size, with an area of about 9 mm^2. Absorptivity was calculated as $A = 1 - \frac{I_s}{I_{ref}}$, where I_s and I_{ref} are the currents collected by a photodiode at the bottom port of the integration sphere for the sample and for a reference barium sulfate scattering surface. The IV characteristics and the PCE of the devices where measured using a separate solar spectrum simulator (ABET Technologies Sun 3000), equipped with a Xe lamp and an AM1.5G filter. The calibration of the system was checked with a standardized silicon photovoltaic cell before each measurement. Photoluminescence spectra and time-resolved photoluminescence measurements of the QDs were obtained using a Jobin Yvon VS140 spectrometer and a silicon single photon avalanche diode (PicoQuant PDM Series) coupled to a time-correlated single photon counting (TCSCP) acquisition card (Becker & Hickl SPC-14). The excitation source was a tunable femtosecond Ti:Sapphire (Coherent Chameleon, 80 MHz repetition rate and 180fs pulse duration) coupled to a second harmonics generator (Coherent SHG). A confocal configuration was used, with a dichroic mirror (Thorlabs DMLP567, cut-off at 567nm) separating excitation and emission. The excitation was focused on the sample using a 10x objective (Nikon M-Plan 10, NA=0.25), while the photoluminescence was focused onto the APD and onto the slit of the spectrometer with a 40x objective (Nikon M-Plan 40, NA=0.50). The photoluminescence was filtered by a long pass edge filter (Thorlabs FEL450) and a short pass filter (Thorlabs FES0700), to respectively filter out the excitation and the InGaP emission. The photon flux absorbed by the sample was kept constant for all wavelengths, using a reference of 0.5mW at 450nm.

4.3. Hybridization with QD575

In this work, we use colloidal semiconductor QDs to engineer a single layer, LDS, antireflective coating that utilizes RET to harvest the carriers trapped in the window layer. Single junction InGaP devices (Figure 4.1a) coated with a 30nm AlInP window layer were hybridized with two batches of oleic acid capped CdS_xSe_{1-x}/ZnS core/shell colloidal

semiconductor QDs emitting at 585nm and 665nm (respectively QD-585 and QD-665). The band diagram of the hybrid solar cell is depicted in Figure 4.1b along with the energy transfer processes at play.

After hybridization with the QDs, absorptivity measurements showed a drastic increase (Figure 4.3a). The effect is especially pronounced in the UV, where the QDs are strong absorbers, with a 22% relative increase in absorptivity at 325 nm. The enhancement remains significant across the 300-1100nm wavelength range under consideration, even for energies below the bandgap of the QDs. This indicates that the QD film acts as a refractive index matching layer between the air and the window layer, enhancing the overall light coupling efficiency across the spectral range. The optimal value for a refractive index matching layer at normal incidence can be approximated to the geometric average of the refractive indices of the materials above and beneath it [105,106]. In our case, using a value of n=3.00 for AlInP [88] and n=1 for air at 585nm, the optimal value is found to be n=1.73. This is indeed close to the refractive index of the QDs, with a value of 1.61 at 585 nm. The absorptivity enhancement due to refractive index matching can be approximated at normal incidence using the transfer matrix method at the air/QDs and QDs/AlInP interfaces for a 10nm thick QD thin film, as reported in the literature [107,108]. These calculations only account for variations in the specular reflectance, while diffuse reflectance (scattering) is neglected. The calculated relative absorption enhancement for a non-absorbing film is presented as a green dashed curve in Figure 4.3a. A good match between measured and calculated data can be observed between 600 and 900nm. In this range, the QDs do not absorb light and the calculations, that assume a non-absorbing layer, provide a good approximation of the absorptivity enhancement. The slight mismatch above 900nm is assumed to be due to the additional contribution of the InGaP/GaAs interface. Below 600nm, the QDs become strong absorbers and the mismatch between measured and calculated curves is attributed to the absorption of the QDs. The fringe patterns visible in the absorptivity spectra above 750 nm are attributed to interferences within the InGaP layer for photon energies below its bandgap. Hybridization with QD-665 was found to have a similar effect on the absorptivity of the devices, with a broadband increase due to refractive index matching and an additional increase due to the absorption by the QDs (see Section 4.4).

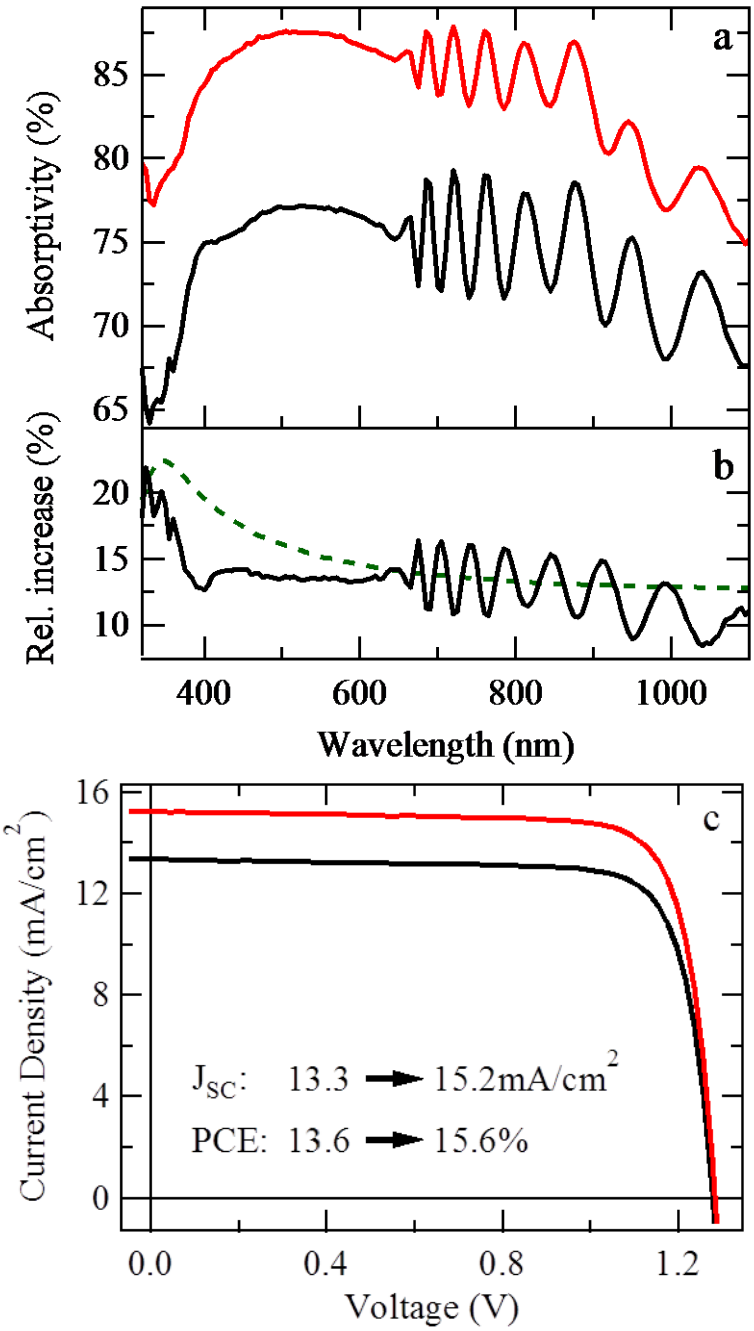

Figure 4.3: a) Absorptivity of the devices before (black) and after (red) hybridization with QD-585. b) Measured (black, solid) and calculated (green, dashed) relative absorptivity enhancement due to hybridization, assuming a non-absorbing layer of QDs. c) I-V characteristics of the device before (black) and after (red) hybridization with QD-585.

The current-voltage (I-V) characteristics and PCEs of the solar cells were investigated under one sun illumination in a solar simulator (Figure 4.3b). As expected from the

absorptivity data, the short-circuit current (J_{sc}) of the QD-585 hybridized device is strongly enhanced, increasing from 13.31mA/cm^2 to 15.21mA/cm^2. The PCE is found to increase from 13.6% to 15.6%, indicating a relative enhancement of 14.6%. The open-circuit voltage (V_{oc}) and fill-factor (FF) are mostly unchanged, as expected for an LDS driven enhancement. In the case of QD-665, hybridization is found to be detrimental, with a relative decrease of the PCE by 10.6%.

The external quantum efficiency (EQE) spectra of the devices, both before and after the QD deposition, are presented in Figure 4.4a. The EQE of the hybrid device (red curve) is significantly improved compared to the bare case (black curve) across the wavelength range, with a maximum relative enhancement of 227% at 320 nm. The 1s absorption peak of the QDs is clearly visible as a negative dip in the EQE spectrum of the hybrid device at 560nm. To separate the effects of light coupling enhancement and of QD absorption, the EQE after hybridization can be estimated for a non-absorbing film as follows:

$$EQE_{calc} = EQE_{bare} * (1 + \Delta A_{Fresnel}) \quad (35)$$

where EQE_{bare} is the EQE of the device before hybridization and $\Delta A_{Fresnel}$ is the relative absorption enhancement for a non-absorbing layer shown in Figure 4.3b. The calculated EQE, shown as a green curve in Figure 4.4a, corresponds to the EQE of a device coated with a non-absorbing material of the same refractive index as the QDs. Below 382nm, the EQE of the hybrid device is largely enhanced compared to EQE_{calc}. This indicates that the enhancement is not only due to refractive index matching, but that the absorption properties of the QDs activate efficient photon conversion channels that increase the EQE. Above this crossing point, the EQE of the hybrid solar cell remains significantly lower than the calculated values. The presence of a dip in the EQE spectrum of the hybrid device at the 1s absorption wavelength of the QDs clearly shows the detrimental effect of QD absorption in this wavelength range. Above 600nm, the QDs are only weakly absorbing and EQE_{calc} matches the values measured for the hybrid device.

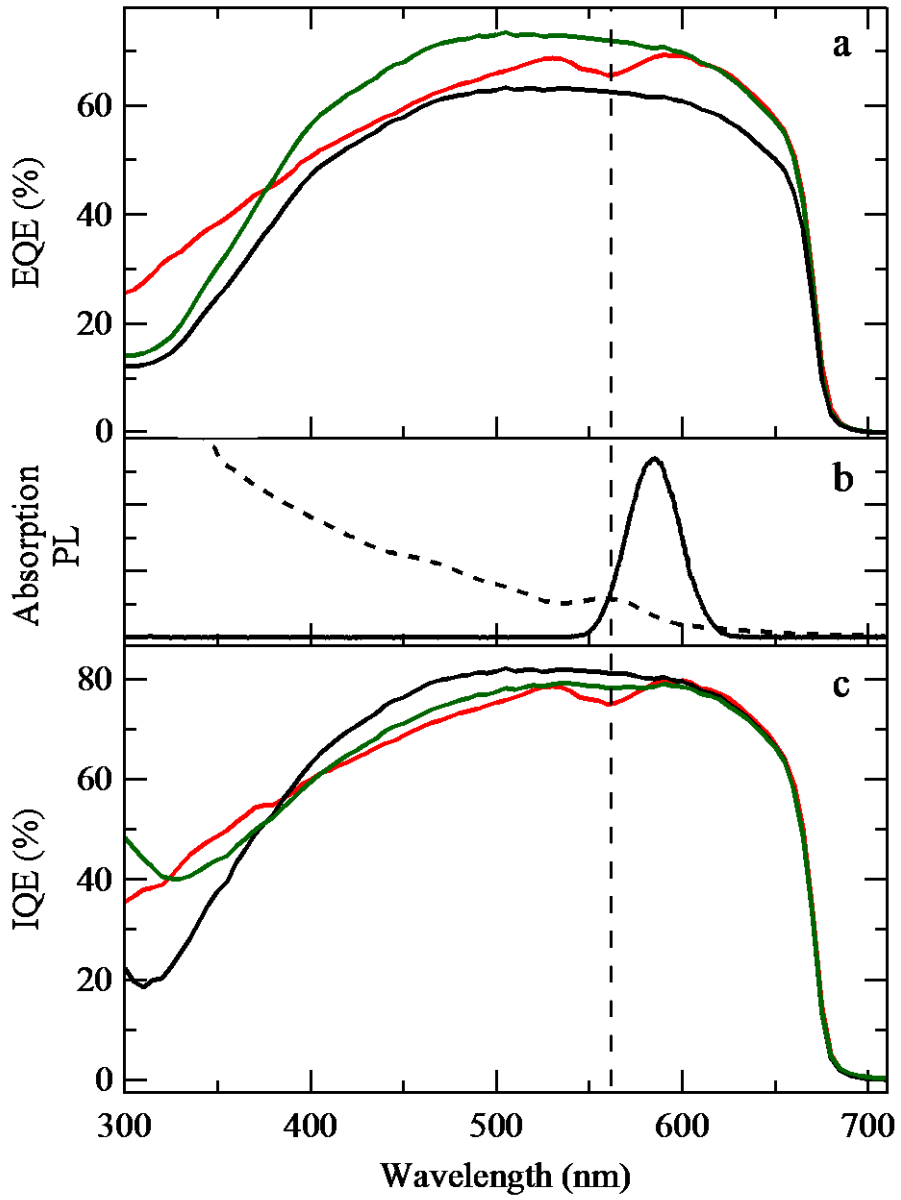

Figure 4.4: a) EQE of the device before (black) and after (red) hybridization with QD-585 and calculated EQE of the hybrid structure assuming a non-absorbing QD layer (green). b) Photoluminescence spectrum (black, solid) and absorption spectrum (black, dashed) of QD-585 on glass. c) IQE of the device before (black) and after (red) hybridization with QD-585. The green solid curve corresponds to the fitted hybridized IQE with a RET efficiency of 70%.

To explain the EQE variations after hybridization, we consider two QD-mediated pumping mechanisms. On the one hand, the QD film acts as a LDS layer: QDs are optically excited, radiatively relax and the resulting photoluminescence is transmitted through the window

layer into the InGaP p-n junction, where it is absorbed to create efficiently extractable carriers. The second mechanism involves RET of excitons photogenerated in the AlInP window layer to the QD epilayer that consequently luminesce, resulting in a RET mediated LDS process. Since both LDS processes involve the absorption of the QD luminescence by the p-n junction, their overall PCEs are proportional to the spectral overlap between the emission of the QDs and the EQE of the bare solar cell. The emission wavelength of QD-585 was chosen so as to be close to the maximum EQE of the bare device (Figure 4.4b), with a value of 70% at 585nm. In the case of QD-665, the emission wavelength corresponds only to a 28% EQE in the bare device. The EQE is found to be strongly suppressed after hybridization with QD-665 (see Section 4.4), which demonstrates the importance of the spectral overlap between the QD emission and the EQE of the bare device for the mechanisms under consideration.

The Internal Quantum Efficiency (IQE) is shown in Figure 4.4c for both devices, before and after hybridization. The IQE of the QD-585 hybridized device (red) is found to be significantly higher than the IQE of the bare device (black) below 385nm, with a maximum enhancement in excess of 200% at 310nm. Hybridization proves to be detrimental to the IQE above 385nm. This crossing point confirms the presence of a competition between LDS mechanisms and direct radiative excitation of the InGaP p-n junction, due to radiative coupling losses and non-radiative recombination channels intrinsic to the QDs. For lower wavelengths, LDS is efficient enough compared to direct pumping of the p-n junction to beneficially contribute to the IQE of the hybrid device. The absorptivity of both the QDs and the window layer increases rapidly towards the UV, which enhances the impact of LDS. Above the crossing point, LDS cannot compete with direct radiative pumping of the p-n junction and the hybridized IQE is lower than in the bare case. Getting closer to the InGaP bandgap, the QDs become non-absorbing and the hybridized and bare IQEs match. Hybridization with QD-665 strongly suppressed the IQE across the absorbing spectral range of the QDs (see Section 4.4).

The IQE of the hybrid structure was modelled to separate the contributions of LDS and of direct optical pumping of the p-n junction:

$$IQE_{Hybrid}(\lambda) = IQE_{direct}(\lambda) + IQE_{LDS}(\lambda) + IQE_{RET}(\lambda) \quad (36)$$

where IQE_{direct}, IQE_{LDS} and IQE_{RET} are the contributions of direct optical pumping of the p-n junction, of LDS due to direct optical pumping of the QD film and of RET mediated LDS to the overall IQE, respectively. These contributions are described as follows:

$$IQE_{direct}(\lambda) = \left(1 - \alpha_{QD}(\lambda)\right) * \left(1 - A(\lambda)\right) * IQE_{InGaP}(\lambda) \quad (37)$$

$$IQE_{LDS}(\lambda) = \alpha_{QD}(\lambda) * QY * IQE_{Bare}\left(\lambda_{PL-QD}\right) \quad (38)$$

$$IQE_{RET}(\lambda) = \left(1 - \alpha_{QD}(\lambda)\right) * A_{AlInP}(\lambda) * \eta_{RET} * QY * IQE_{bare}\left(\lambda_{PL-QD}\right) \quad (39)$$

where IQE_{Hybrid} and IQE_{Bare} are the IQEs of the hybrid and bare devices, IQE_{InGaP} is the IQE of the InGaP p-n junction, α_{QD} and QY are the absorptivity and quantum yield of the QDs, λ_{PL-QD} is the emission wavelength of the QDs, A_{AlInP} is the absorptivity of the AlInP window layer and η_{RET} is the efficiency of resonance energy transfer between the window layer and the QDs. For zero extraction efficiency of excitons photogenerated in the window layer:

$$IQE_{Bare} = \left(1 - A(\lambda)\right) * IQE_{InGaP}(\lambda) \quad (40)$$

For simplicity, the quantum yield and the resonance energy transfer efficiency are assumed independent of the excitation wavelength. The absorptivity of a 30nm thin film of AlInP was calculated using the complex refractive index of the material [88]. The absorptivity of the QD film on the solar cell was assumed to be the same as for the QDs on glass, measured in an ultraviolet-visible spectrometer. Initially, we neglect the RET mediated LDS contribution and set the RET efficiency to zero. A least squares technique was used to fit the measured data by varying the QY, which yielded an unrealistic value of QY of 66%. This value is much higher than the QY of 40% which was measured for QDs deposited on glass in an integrating sphere and higher than the QY of the QDs in solution (50%). Next, we fit the data by setting the QDs QY to 40%, as measured on glass, and by using the RET efficiency as a fitting parameter. The resulting IQE spectrum is shown as a green continuous line in Figure 4.4c. The analysis yielded a value of 71% for the RET efficiency, in agreement with previous measurements in similar hybrid QD/epitaxial semiconductor configurations [42]. The remaining variations between fitted and measured data are attributed in part to the neglected excitation energy dependence of the QY of the QDs (demonstrated in CdTe/ZnS and CdSe/ZnS QDs) [109,110]. Resonant Rayleigh scattering near the band-edge of the QDs could also explain why the 1s absorption peak of the QDs is more pronounced in the measured data than in the simulated curve.

The contributions of the various IQE components to the generated photocurrent can be estimated using the following equation:

$$\frac{I_X}{I_{SC}} = \frac{\int IQE_X(\lambda) * A_{hybrid}(\lambda) * \Phi_{AM1.5}(\lambda) d\lambda}{\int EQE_{hybrid}(\lambda) * \Phi_{AM1.5}(\lambda) d\lambda} \quad (41)$$

where I_X and IQE_X are respectively the contributions of each pumping channel to the I_{SC} and to the IQE of the solar cell, A_{hybrid} is the absorptivity of the hybrid structure and $\Phi_{AM1.5}$ is the photon flux of the AM1.5 direct spectrum (ASTMG173). RET mediated LDS is found to account for 3.5% of the total photocurrent, while direct LDS from the QD film is found to amount to 5.2% of the total photocurrent, resulting in an 8.7% overall contribution of LDS to the total photocurrent.

The PCE variations can be correlated to the EQE data, since the PCE is proportional to the integral of the product of the EQE and of the AM1.5 photon flux:

$$PCE\ \alpha \int EQE * \Phi_{AM1.5} d\lambda \quad (42)$$

where $\Phi_{AM1.5}$ is the AM1.5 photon flux spectrum (NREL ASTM G173-03 Direct + Circumsolar) and where the integration is done from 300nm to 750nm. Calculating these values for the bare and hybrid cases, we find a relative PCE enhancement of 13.3%. The slight discrepancy between the values measured and calculated from the EQE is attributed to the difference in power density between the monochromatic source used for the EQE measurements and the AM1.5 solar spectrum. Since the absorption of the hybrid and bare structure vary significantly, spectral mismatch issues due to imperfections in the simulated AM1.5 spectrum of the solar simulator can complicate direct PCE measurements. Deriving these values from EQE measurements thus represent an important verification of the validity of the measured photon conversion efficiencies. The enhancement is even more pronounced if the AM1.5 photon flux spectrum is replaced by the AM0 solar spectrum (ASTM E490 Air Mass Zero) in Equation 41. This spectrum describes the solar spectrum outside the earth's atmosphere, and is of interest for space applications. The PCE is found to increase in this case by 17.6% after hybridization with QD-585, which further underlines the usefulness of RET luminescent down-shifting for space applications, where costly III-V multi-junction solar cells are typically used.

Further evidence of RET between the AlInP window layer and a QD-585 epilayer was obtained using time-resolved spectroscopy, by monitoring the photoluminescence rise time

of the QDs as a function of excitation wavelength. The photoluminescence rise dynamics of the QDs on glass and on AlInP are presented as an insert in Figure 4.5 for an excitation wavelength of 355nm using 180fs pulses. The photoluminescence rise dynamics was fitted with a single exponential for the first 200 ps for both glass and AlInP substrates and the rise times are presented as a function of the excitation wavelength in Figure 4.5. The rise dynamics of the QDs on glass is found to be only weakly dependent on the excitation wavelength. The slow relaxation dynamics are attributed to the ternary nature of the QDs, while the weak excitation wavelength dependence on glass is attributed to an accelerated photoactivation for shorter wavelengths. On the contrary, the rise time of the QDs on AlInP is found to vary strongly with excitation wavelength, with a rapid acceleration below 400nm and a 25% decrease at 355nm compared to the value on glass. Excitons photogenerated in the AlInP window layer can rapidly relax (~100fs) and transfer non-radiatively through RET to the overlying QDs. The transferred excitons are relatively cold (~2.2eV) and can quickly relax to the ground state of the QD (~2.1eV), thus accelerating the average rise time of the QDs population. As the excitation wavelength decreases, the exciton population in the window layer increases, which enhances the RET contribution to the rise time of the QDs. This provides strong evidence of the presence of RET between the AlInP window layer and the QD epilayer in hybrid InGaP solar cells.

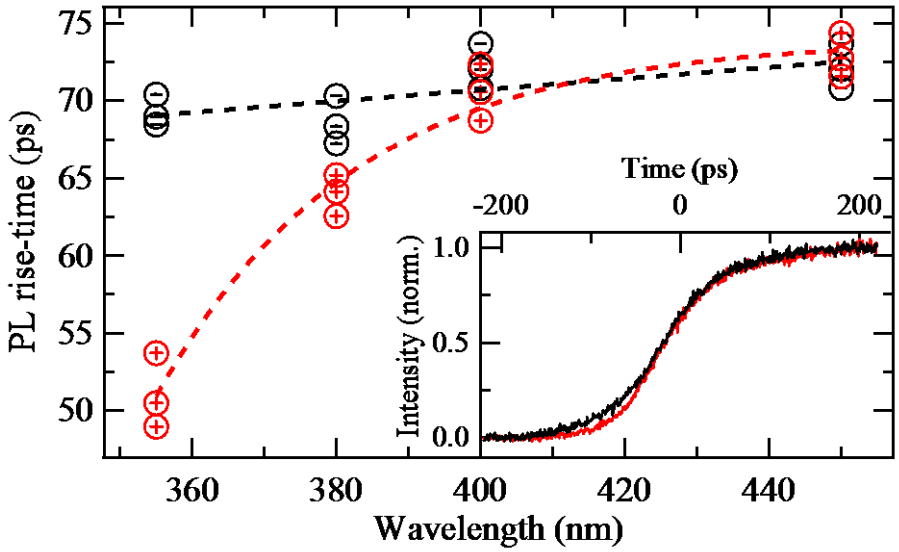

Figure 4.5: Photoluminescence rise time of QD-585 on glass (black) and on AlInP (red) as a function of the excitation wavelength. The inset shows the rise dynamics of QD-585 on glass (black) and on AlInP (red) for a 355nm excitation wavelength.

4.4. Hybridization with QD665

Absorptivity, EQE, IQE and I-V measurements were carried out before and after hybridization with QD-665. The absorptivity of the bare (black curve) and QD-665 hybridized (red curve) device are displayed in Figure 4.6a and the relative enhancement after hybridization is show in Figure 4.6b. The enhancement is found to be especially important in the UV, where QDs absorb strongly, with a relative increase of 30% at 320nm. The broadband enhancement of the absorptivity across the spectral range under consideration is a clear sign that the QD epilayer acts as a refractive index matching layer, increasing the light coupling efficiency. The absorption and photoluminescence spectra of the QDs on glass are presented in Figure 4.7a.

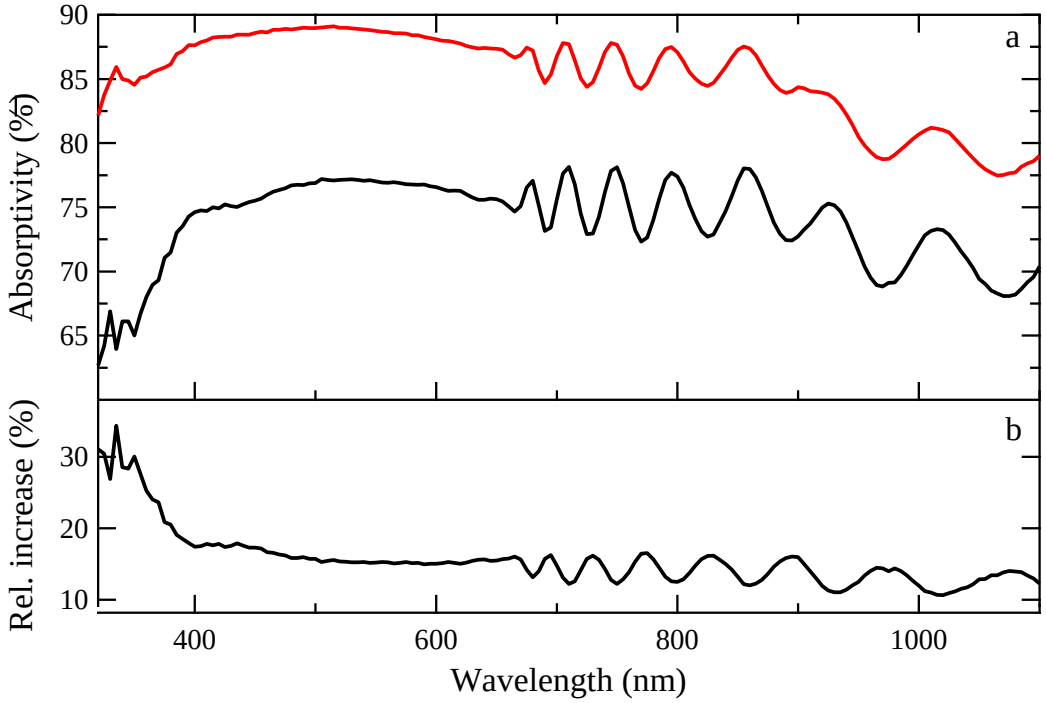

Figure 4.6: a) Absorptivity of the solar cell before (black) and after (red) hybridization with QD-665. b) Relative increase of absorptivity after hybridization with QD-665.

The EQE of the device before (black curve) and after (red curve) hybrization with QD-665 are shown in Figure 4.7b. The EQE is found to be significantly lowered after hybridization in the 300 to 600 nm range. This indicates that the absorption of the dots is in this case detrimental, countering any potential increase due to refractive index matching. The slight increase above 600nm, where the absorption cross section of the QDs is low, is attributed to refractive index matching.

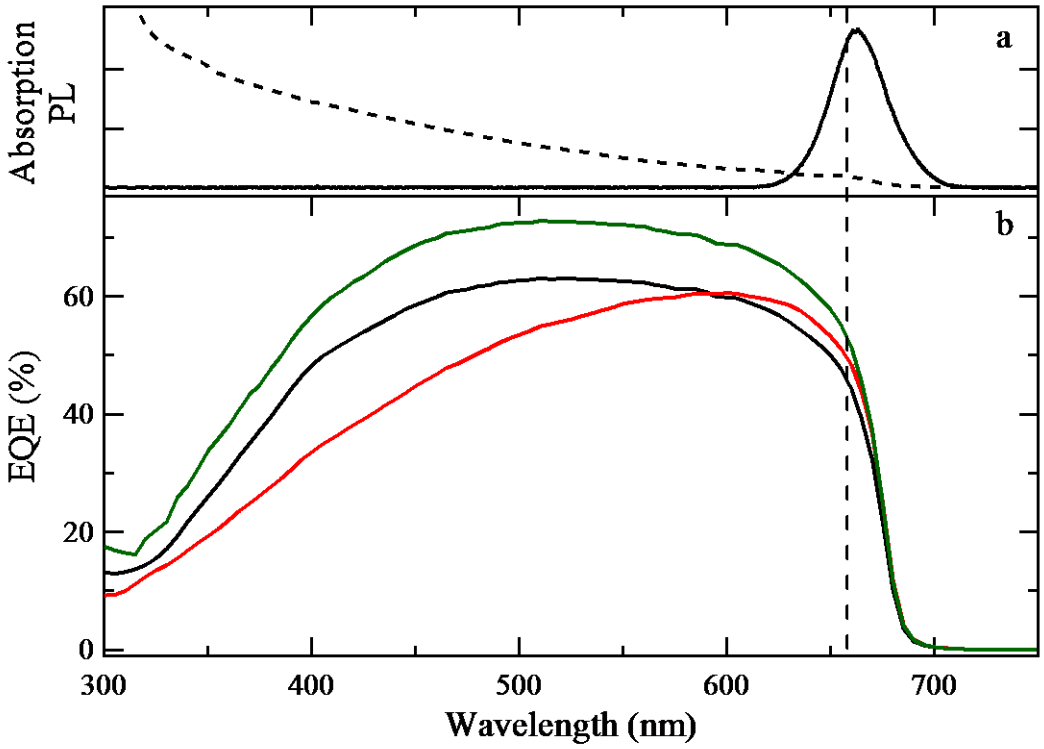

Figure 4.7: a) Photoluminescence spectrum (black, solid) and absorption spectrum (black, dashed) of QD-665 on glass. b) EQE of the device before (black) and after (red) hybridization with QD-665.

The IQEs of the device before (black curve) and after (red curve) hybrization with QD-665 are presented in Figure 4.8. The IQE is found to be strongly supressed after hybridization across the 300-700nm wavelength range. LDS cannot in this case compete with direct radiative pumping of the p-n junction, as expected from the poor overlap between the emission spectrum of the QDs and the EQE of the bare device.

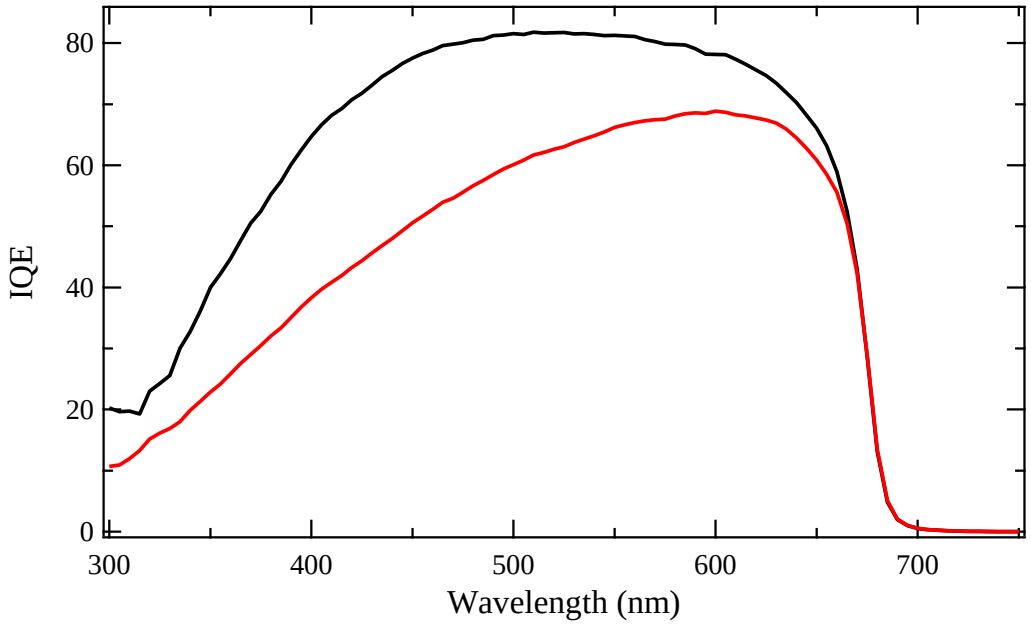

Figure 4.8: IQE of the device before (black) and after (red) hybridization with QD-665.

The I-V characteristics of the devices are presented in Figure 4.9. As expected from the previous data, the J_{sc} is strongly lowered after hybridization, with a relative decrease of 11.1%. The V_{oc} and the FF are not significantly impacted (<1% relative variations). The PCE is found to decrease from 13.4% to 12.0%, indicating a relative decrease of 10.6%.

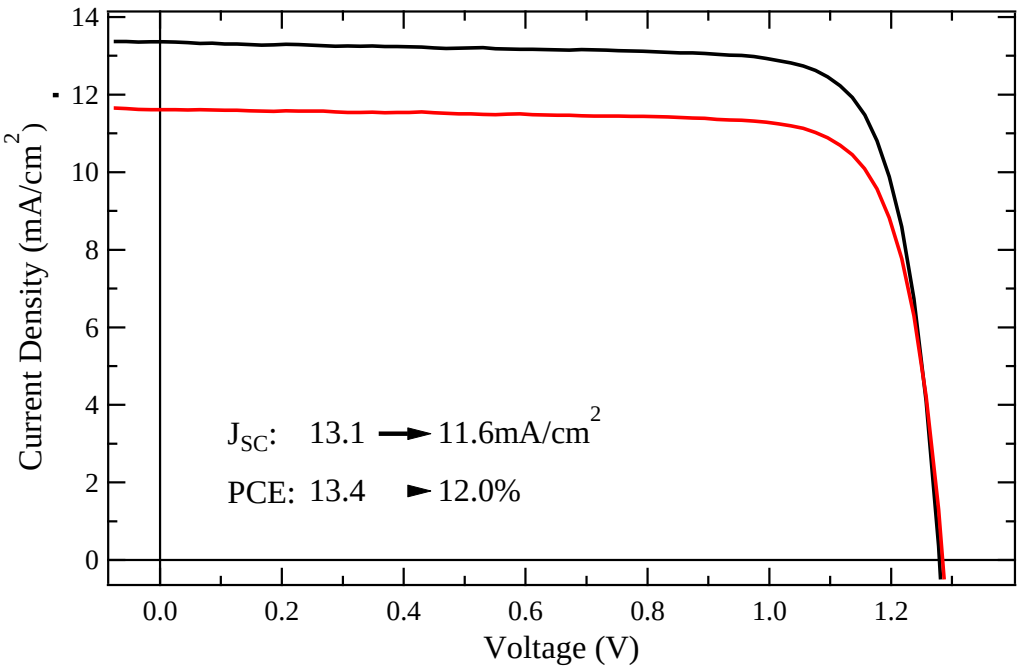

Figure 4.9: I-V characteristics of the device before (black) and after (red) hybridization with QD-665.

4.5. Conclusion

In this work we present a new paradigm for luminescent down-shifting layers that uses resonance energy transfer to engineer a recycling scheme for the carriers generated in the AlInP window layer of InGaP solar cells. We demonstrate an important enhancement of both internal and external quantum efficiencies in the UV-blue region of the solar spectrum due to direct and resonance energy transfer-mediated luminescent down-shifting. Refractive index matching at the air/AlInP interface also provides a broadband increase of the EQE across the solar spectrum. The quantum dot epilayer provides a large relative increase of 14.6% and an absolute increase of 2% of the photon conversion efficiency. Resonance energy transfer mediated luminescent down-shifting is believed to be a promising scheme to improve the high energy response of photovoltaic technologies plagued by strongly absorbing high bandgap materials, such as CdTe or CIGS.

4.6. Contributions to the work

This work was done in collaboration with Prof. Peichen Yu from the Department of Photonics of the National Chiao Tung University in Taiwan, who provided the bare PV devices. All electrical and optical (including time-resolved) measurements presented here were carried on by the author in Southampton university. The theoretical framework and analysis was also carried on by the author. A patent related to this work, and to RET-LDS in general, was filed in December 2014, and included significant contributions from the author.

Chapter 5: Hybrid QD/CIGS solar cells

5.1. Introduction

With lab-scale efficiencies exceeding 20% [111], thin film Cu(In,Ga)Se_2 (CIGS) solar cells have established themselves as frontrunners of thin-film photovoltaic (PV) technology. The intrinsic qualities of polycrystalline CIGS, such as its high absorptivity, bandgap tunability and easy grain boundary passivation, have attracted a lot of attention since the early days of PV technology [30]. Their compatibility with high throughput roll-to-roll processing could allow a drastic reduction of the device cost and payback time compared to traditional vacuum co-evaporation or sputtering techniques [112]. Typical CIGS solar cells are deposited on a rigid glass, flexible stainless steel or plastic substrate coated with a layer of molybdenum that acts as a back contact and reflector. A thick (2 μm) p-type CIGS absorber and thin (~50 nm) n-type CdS buffer layer are subsequently deposited to form a CdS/CIGS heterojunction. The devices are terminated with a thin intrinsic ZnO widow layer (~50 nm) and an Al:ZnO (AZO) transparent conductive oxide (TCO) layer (see Figure 5.1). An important drawback of this device stack architecture is the poor response of the solar cells in the UV to green part of the spectrum, due to the strong optical absorption of the CdS buffer, ZnO window and AZO TCO layers [61,113]. The strong doping asymmetry between the CIGS and CdS layers confines the depletion region to the CIGS. This inhibits the extraction efficiency of the carriers generated in the CdS layer and results in large quantum efficiency losses at lower wavelengths.

Luminescent down-shifting (LDS) provides a simple scheme to mitigate this issue. In this approach, a luminescent material deposited on or integrated into the device absorbs high energy photons and reemits below the bandgap of the buffer, window or TCO layers, optically pumping the absorber and generating efficiently extractable carriers [99,114]. Both organic dyes and quantum dots [98,102] have been extensively investigated as LDS materials for numerous PV technologies suffering from similar limitations [88], such as III-V and cadmium telluride solar cells [88,96–98,114]. The high absorptivity in the UV band, narrow emission spectral range, good absorption and emission tunability and high

quantum yields of QDs make them especially well-suited for such applications [115,116]. Previous attempts to implement LDS in CIGS solar cells focused on depositing luminescent material onto the AZO layer and resulted in relative low efficiency enhancements between 3 and 5% [98,117,118].

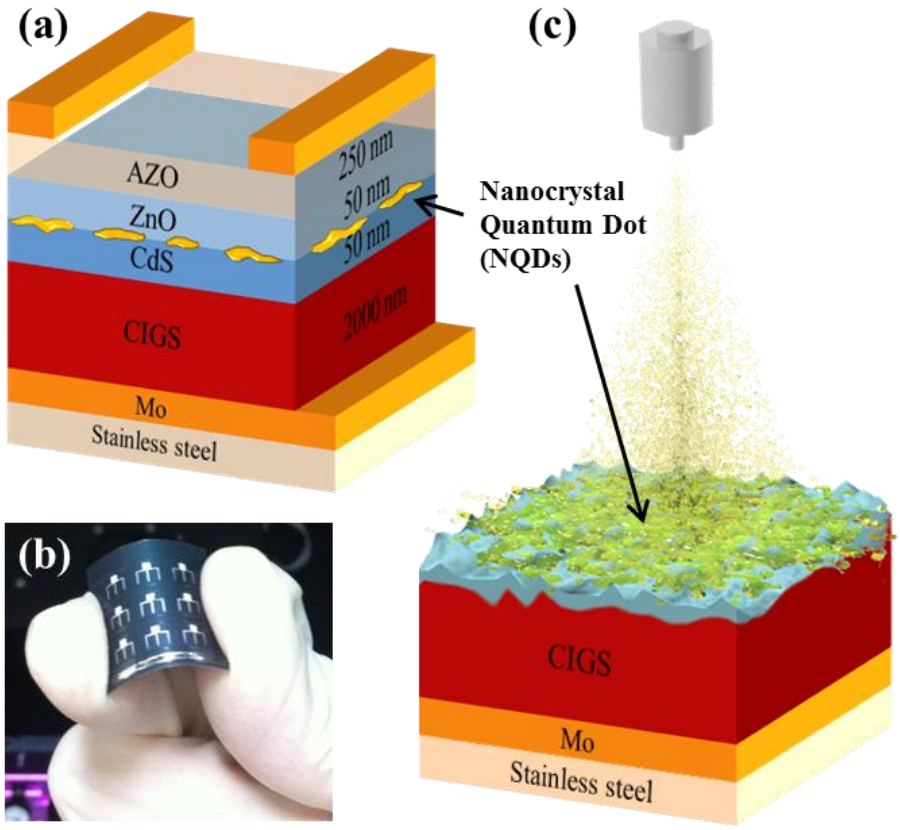

Figure 5.1: (a) Schematic illustration of a flexible inkjet-printed QD/CIGS hybrid solar cell. (b) Photograph of a hybrid device. (c) Schematic illustration of the pulsed-spray QD deposition system.

In this work, we report on the successful incorporation of self-assembled clusters of CdSe/ZnS core/shell QDs into flexible CIGS solar cells. The QDs are embedded between the CdS buffer and the ZnO window layer using pulsed-spray deposition (see Figure 5.1). We leverage the poor uniformity of spray deposited QD layers to engineer an integrated luminescent and light scattering layer of self-assembled QD aggregates. The nanocrystals are tuned to emit below the bandgap of CdS, with an emission wavelength of 560 nm, and LDS is found to provide an important enhancement of the quantum efficiency within the absorption range of the QDs. The QD clusters also provide a large increase of the PCE in

the red to near-IR spectral range. The QD aggregates scatter the incident light and displace the absorption closer to the CIGS/CdS interface, where the depletion field is strongest, which consequently increases the average extraction efficiency of the photogenerated carriers. The morphology of the QD aggregates is investigated using luminescence microscopy and cross-sectional transmission electron microscopy (TEM), while LDS is characterized using time-resolved spectroscopy. An optimum QD dose is obtained and hybridization is found to result in a 10.9% relative enhancement of the PCE. Integrating the QDs into the layer stack is believed to be beneficial to the performances of the hybridized structures. Placing scattering centres in close proximity to the p-n junction increases the in-coupling angle, which lowers the average penetration depth of scattered photons and thus increases the extraction efficiency of the generated carriers.

5.2. Materials and methods

5.2.1. Fabrication of the CIGS solar cells

The copper oxide (CuO), indium oxide (In_2O_3) and gallium oxide (Ga_2O_3) have been mixed with a Ga/(In+Ga) ratio of 0.3 and a Cu/(In+Ga) ratio of 0.8~1 in deionized water. The wet stirred milling process was then used with a small amount of surfactant to avoid nanoparticle aggregation, transforming particles with an initial size of a few micrometres into particles with size of only 50-80nm in a stable non-flocculated state. The solid content of the stable ink was measured to be about 0.2 g/ml. A doctor blade was used to coat the precursor film on a Mo/Cr/stainless steel (SS) substrate. The precursor was then reduced in an H_2 atmosphere at 450°C for 30 minutes, before being annealed in an H_2Se atmosphere and in an H_2S atmosphere at 400°C for 30 minutes and 500°C for 30 minutes, respectively. The CIGSeS absorption layer was rinsed in a KCN (5 wt%) solution to remove the excess CuSe. The CdS buffer was deposited using Chemical Bath Deposition (CBD) in a cadmium sulfate, thiourea and ammonium hydroxide solution. Before deposition, all substrates were rinsed with DI-water to prevent air voids. All substrates were blow-dried using nitrogen after deposition. Finally, the CdS/CIGSeS layer was coated with a transparent conductive oxide (TCO) using sputtering deposition, and a silver contact grid was deposited using a printing process.[26] The resulting device structure is a Al:ZnO

(250nm) / ZnO (50nm) / CdS (50nm) / CIGS (2μm) / Mo(800 nm) layer stack on a stainless steel substrate.

5.2.2. Deposition of nanocrystal quantm dots

A solution of colloidal CdSe/ZnS core-shell QDs procured from Sigma Aldrich (Lumidot™ 560, 0.08 mg/ml in toluene) was dispensed onto the surface of the CdS layer using air pressure pulsed-spray deposition. The QDs displayed 1s absorption and emission peaks of 525 nm and 561 nm, respectively. The QDs were chosen for their good quantum yield (>50% in solution) and their relatively low cost. The emission wavelength was tuned to limit absorption of the QD photoluminescence in the CdS layer while providing a good spectral overlap between QD and CdS absorption. In traditional spraying techniques, the viscosity of the spraying mixtures can considerably affect the uniformity of the finished film. The interaction between the particles in the pre-mixed solution can cause an aggregation of the material, which can impede the propagation of the spray. Pulsed-spray deposition mitigates this issue by using an air-injection mechanism in the nozzle, an intermittent spraying frequency (5 to 10 Hz) and a constant stirring system. This allows a better separation of the target particles in the suspending solution compared to traditional methods. The atomized NQD solution is projected through a small nozzle before reaching the desired surface, which further limits quantum-dot self-assembly. The operation was computer controlled to precisely monitor the amount of material deposited.

5.2.3. Optical measurements

A 470 nm pulsed diode laser was used for the spectrally-resolved and time-resolved photoluminescence (PL) measurements. The repetition rate of the laser was 4 MHz for the spectrally-resolved measurements and 0.5 MHz for the time-resolved measurements. The excitation power was kept constant at 0.5 mW and the excitation beam was focused at normal incidence with a 20 cm lens. The PL signal of the CIGS and of the QDs was collected at an oblique angle with a 10 cm lens, transferred to a monochromator and detected by a an avalanche photodiode (PicoQuant PDM series) connected to a TCSPC acquisition card (PicoQuant TimeHarp 200). All PL measurements were taken at room temperature. A UV-VIS-NIR spectrophotometer (Hitachi U4100) equipped with standard

mirror optics and an integrating sphere was used to measure the absorption of the solar cells. An Olympus BX51M brightfield/darkfield reflected light microscope equiped with Olympus UIS2 fluorescence mirror units and an Olympus DP26 digital camera was used to obtain bright and dark field images of the samples. The samples were excited with a filtered mercury lamp (BP330-385) and the photoluminescence signal was collected by an objective (Olympus MPLFFLN20x) and filtered with a long-pass filter (BA420) and a dichroic mirror (DM400). All fluorescence images were taken with an integration time of 80 ms and a magnification of 12.6x.

5.2.4. Electrical characterisation

Current-voltage measurements were performed following the procedure described in the international standard CEI IEC 60904-1. All solar cells were characterized under a simulated Air Mass 1.5 Global (AM1.5G) illumination with a power of 1000W/m^2. The temperature was actively controlled during the measurements and was kept at 25±1 °C. The power conversion efficiency (PCE) measurement system consisted of a 1000 W Class A solar simulator (Newport 91192A) equipped with a Xenon lamp (Newport 6271A), an AM1.5G filter (Newport 81088A) and a current-voltage source (Keithley 2400). The spectrum of the solar simulator was measured with a calibrated spectroradiometer (Soma S-2440) between 300 to 1100 nm. The external quantum efficiency (EQE) of the devices was measured using a 300 W Xenon (Newport 66984) light source and a monochromator (Newport 74112). The system was calibrated before each measurement with a calibrated silicon photodetector. The EQE measurements were carried out using a lock-in amplifier (Standard Research System, SR830), an optical chopper unit (SR540) operated at 260 Hz and a 1 Ω resistor in shunt connection.

5.3. Results and discussion

5.3.1. Optical properties

The PV devices studied consist of a Al:ZnO(250 nm)/ZnO (50 nm)/QDs/CdS(50 nm)/CIGS(2 μm)/Mo(800 nm) layer stack deposited on a stainless steel substrate, as depicted in Figure 5.1a and b. The air pressure pulsed-spray deposition system used to

deposit the QD layer is illustrated in Figure 5.1c. The QDs used in this study are colloidal ZnS/CdSe core-shell nanocrystals dispersed in toluene with a photoluminescence quantum yield (QY_{QD}) of ~40%. Reference (without QDs) and hybrid devices were fabricated side-by-side on the same 4 cm^2 sample to eliminate sample to sample disparities. Figure 5.2 shows the photoluminescence (PL) and absorption spectra of spray coated QDs on a glass substrate, along with the absorption spectrum of bulk CdS on glass. The emission wavelength of the QDs (560 nm) is chosen so as to minimize absorption from CdS. At higher wavelengths, CdS becomes transparent and the buffer layer allows transmission of the incident light into the underlying CIGS absorber.

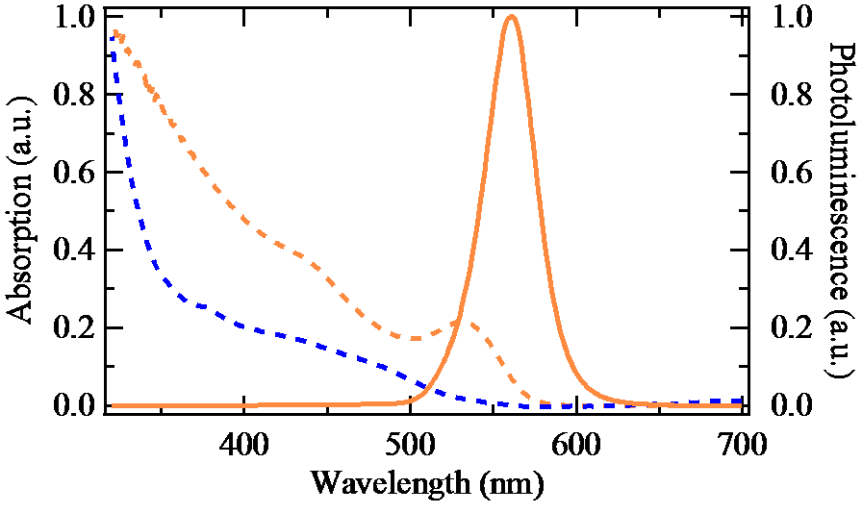

Figure 5.2: Absorption spectrum of a CdS thin-film on glass (blue, dashed line) and absorption/photoluminescence spectra of the QDs (orange, dashed and solid line) on glass.

The absorptivity of the 9-pulse hybrid device and its reference device were obtained in an integration sphere (Figure 5.3). Both spectra exhibit strong interference oscillation patterns across the wavelength range under consideration. This behaviour is attributed to interference within the 250 nm thick transparent AZO layer. No clear variation of the absorptivity due to hybridization is evident. Variations between the hybrid and reference remain below 1%. The absorption of the QD is potentially hidden by slight variations in the AZO thickness which impacts the interference pattern.

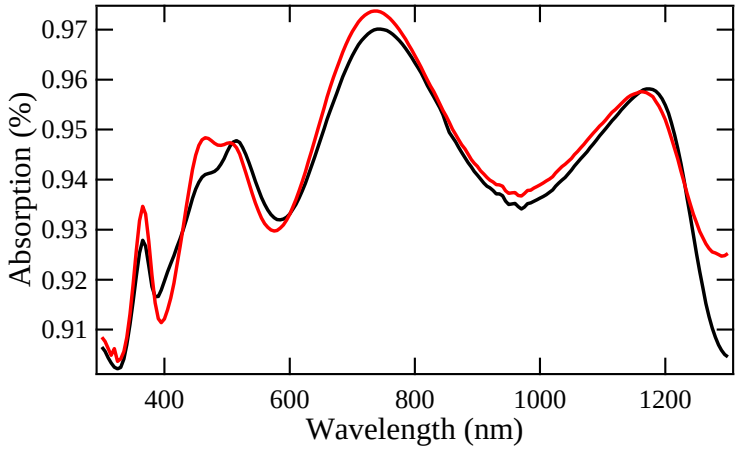

Figure 5.3: Absorption spectra of CIGS solar cells embedded with 9 pulses of QDs (red) and the corresponding reference devices (black).

5.3.2. Morphology study of the QD film

The in-plane morphology of the QD aggregates was studied using dark field fluorescence microscopy. A 2 µm thick CIGS layer capped with a 50 nm CdS thin-film was investigated before and after deposition of 9 pulses of QDs. The weak dark-green non-uniform PL signal in the bare sample (Figure 5.4a) is attributed to the bulk CdS emission. The hybridized sample exhibits bright emission from a non-uniform mesh of QD aggregates as shown in Figure 5.4b. Micrometer-wide features spanning 10 to 100 µm in length can be observed. Such a morphology is characteristic of the self-assembly of spray deposited QDs during solvent evaporation [119]. The lateral size of the QD aggregates was further investigated using cross-sectional TEM in two CdS/CIGS p-n junctions coated with 9 and 17 pulses of QDs (Figure 5.5). In these images, the QD aggregates are visible as a pale grey region embedded between the darker CdS layer and the black carbon support. Hybridization with 9 pulses of QDs is found to form thin (~10 nm) aggregates with a lateral spatial extension of ~500 nm. Aggregation is found to be more pronounced in the case of the 17-pulse deposition, with thicknesses in excess of 300 nm and lateral sizes ranging between 1 and 2 µm. The 17-pulse deposition is thus expected to induce a high series resistance at the ZnO/CdS interface, detrimental to the device performance. High-resolution magnifications of the areas marked with a red square in Figure 5.5a and d are presented in Figure 5.5b and e, respectively. In these images, 3-5 nm diameter nanoparticles can clearly be resolved .

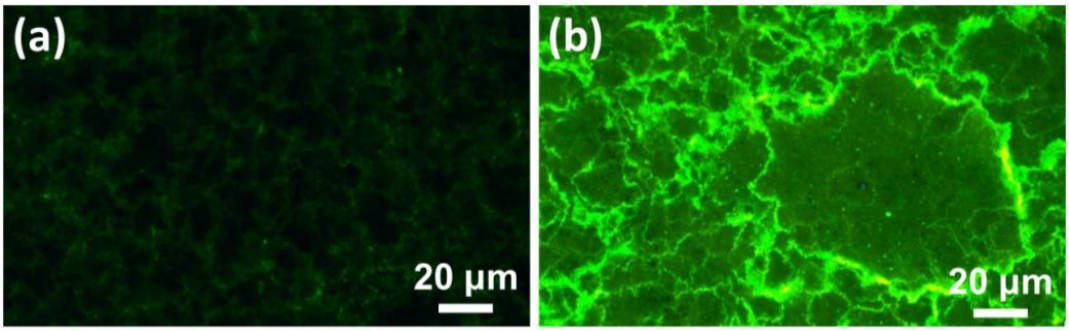

Figure 5.4: Fluorescence microscopy images of a CdS/CIGS junction before (a) and after (b) QD hybridization (9 spray pulses).

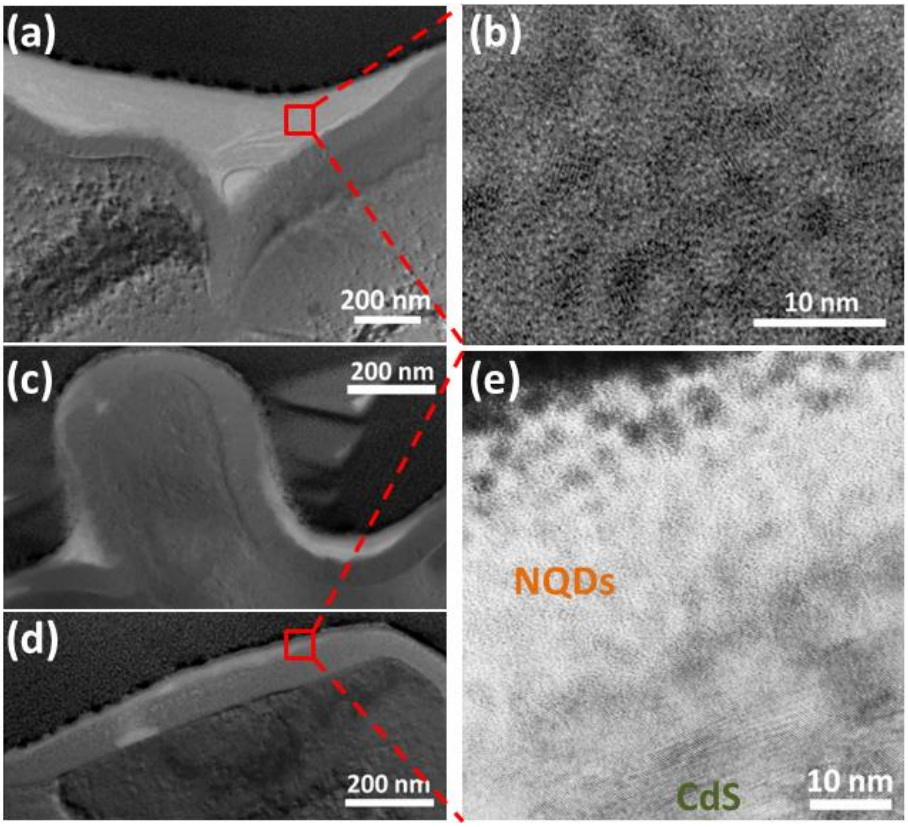

Figure 5.5: Low (a) and high (b) resolution TEM images of a CdS/CIGS junction hybridized with 17 pulses of nanocrystal quantum dots (NQDs). Low (c,d) and high (e) resolution TEM images of a CdS/CIGS junction hybridized with 9 pulses of QDs. The areas selected for magnification are marked with a red square.

5.3.3. Electrical caracterisation

The external quantum efficiency (EQE) and current-voltage (J-V) characteristics of the hybrid and reference devices were investigated for various QD doses, by varying the number of QD spray pulses between 1 and 17. The corresponding J-V curves are presented in Figure 5.6 and the relative variations in short-circuit current density (J_{SC}) (Figure 5.7a), photon conversion efficiency (PCE) (Figure 5.7b), open-circuit voltage (V_{OC}) and fill factor (FF) (Figure 5.7c) between each hybrid device and its corresponding reference device are presented as a function of the number of QD pulses. The variations in device series resistance R_S are derived from the slope of the J-V curves by fitting the curves with a linear function in a 20mV range centered on the open-circuit voltage (Figure 5.7a). The 9-pulse deposition is found to provide the maximum J_{SC} enhancement. The initial increase of the J_{SC} enhancement at lower QD doses is attributed to an increased contribution of LDS and of internal scattering on QD aggregates. The decrease of the J_{SC} above 9 pulses is due to the gradual emergence of an additional series resistance at the CdS/ZnO interface, as shown in Figure 5.7a. This interpretation is further corroborated by the cross-sectional TEM study, which showed that high QD doses promote the assembly of thick clusters larger than the CIGS grains (~1 µm) (Figure 5.4c and d**)**, which strongly impede the extraction of the minority carriers. The PCE variations (Figure 5.7b) are principally driven by the J_{SC}, and the PCE dependence on the QD dose follows closely the behaviour of the J_{SC}. Hybridization is found to be slightly detrimental to the V_{OC} for lower QD doses (Figure 5.7c), the QDs acting as recombination centres at the CdS/ZnO interface. The V_{OC} increase above 9 pulses is attributed to scattering on QD aggregates, which lowers the average penetration depth of the longer wavelength photons and limits bulk recombination in the CIGS layer. Contrary to the V_{OC}, the FF displays a net enhancement at lower doses and a reduction above 9 pulses (Figure 5.7c). The initial enhancement is attributed to LDS of the solar spectrum, which displaces carriers away from the CdS/ZnO interface and limits the space-charge screening of the depletion field. The reduction of the FF for higher QD doses is a consequence of the increase in series resistance. The low FF of the 1-pulse sample was found to be related to an increased shunt resistance, possibly due to a poor homogeneity of the CdS layer. The J-V characteristics of the optimized 9-pulse hybrid solar cell and of its corresponding reference device are presented in Figure 5.7d. The 9-pulse hybridization is found to provide the best overall performances, with a relative

increase in J_{SC} of 12.2% (31.9 mA/cm^2 to 35.5 mA/cm^2) yielding a large 10.9% relative enhancement of the PCE (8.42% to 9.34%).

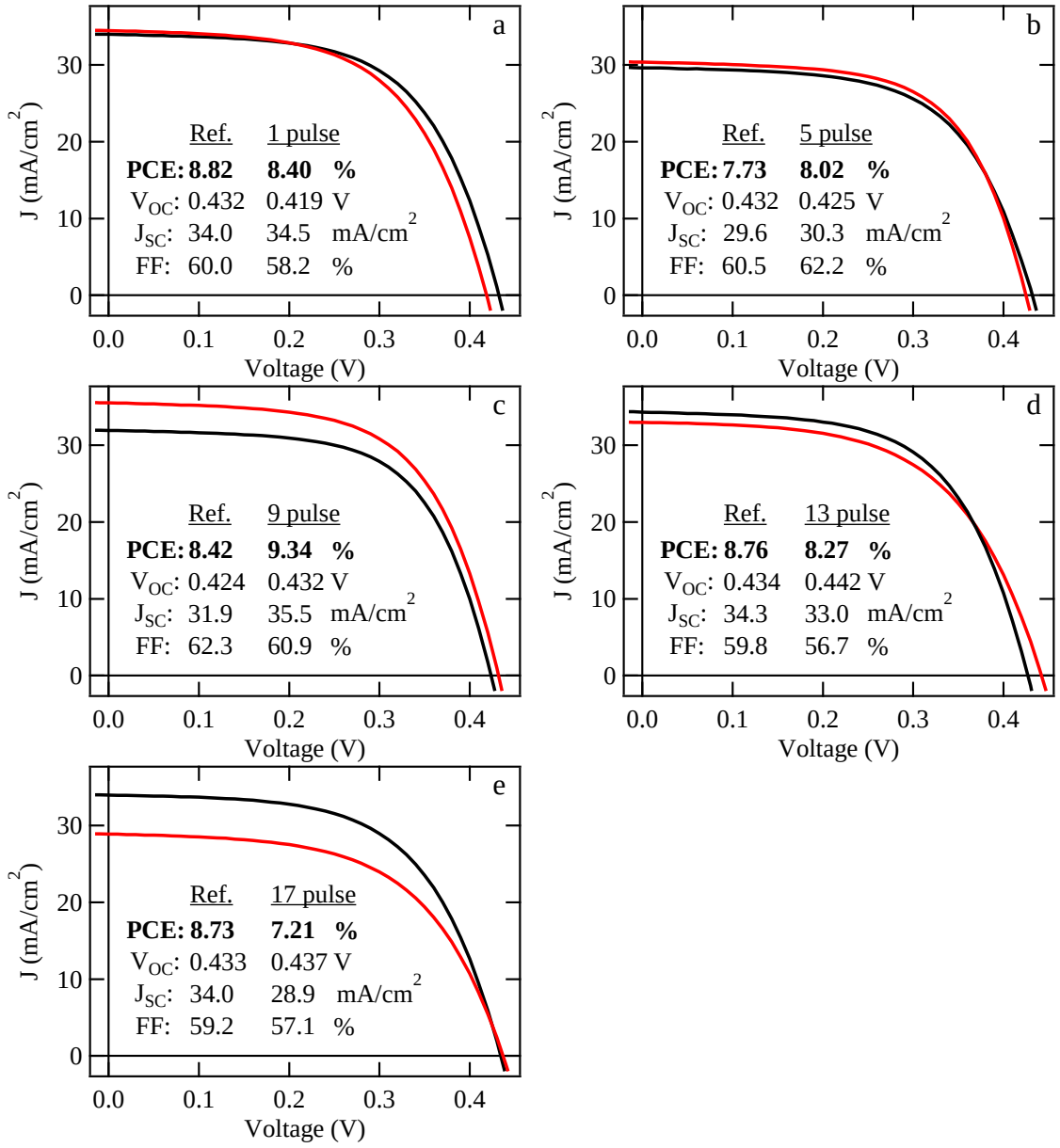

Figure 5.6: J-V curves of CIGS solar cells embedded with (a) 1 pulse, (b) 5 pulses, (c) 13 pulses and (d) 17 pulses of QDs (red) and their corresponding reference devices (black).

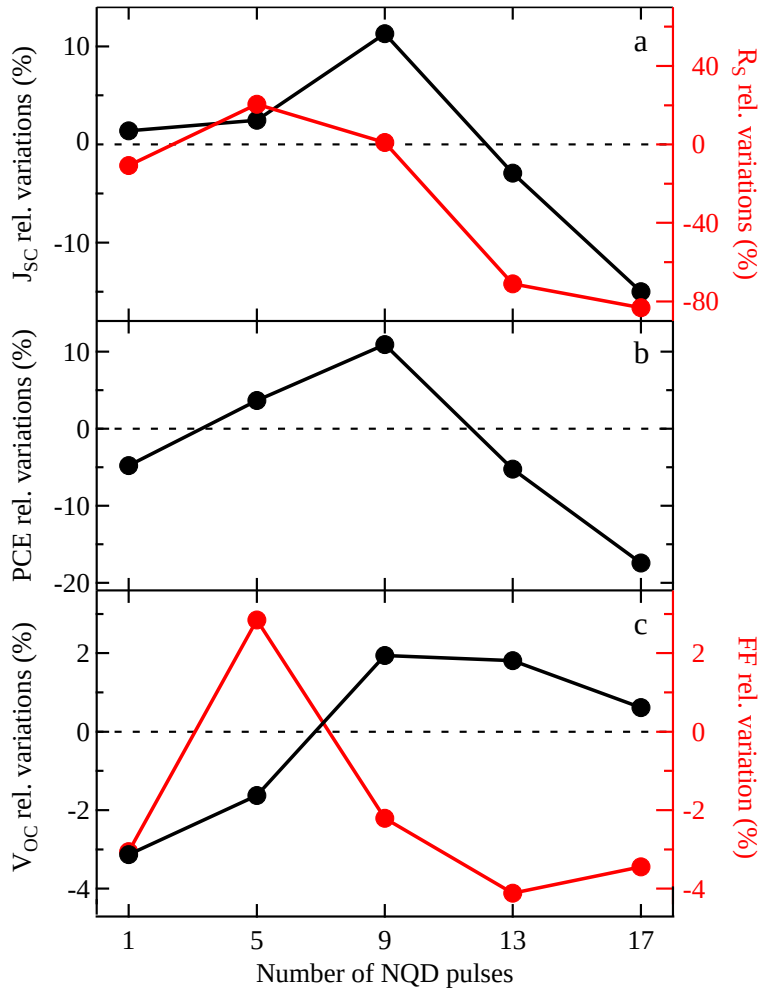

Figure 5.7: (a) Relative variations of the J_{SC} (black) and of the R_s (red). (b) Relative variations of the PCE. (c) Relative variations of the V_{OC} (black) and of the FF (red.

The EQE enhancement dependence on the QD dose was investigated by measuring the hybrid and reference EQEs for various numbers of QD spray pulses. The absorptivity of the 9-pulse hybrid and reference samples was measured in an integrating sphere and was found to be weakly impacted by hybridization (< 1%), thus discarding any potential anti-reflection coating effect (Figure 5.3). The EQE of the hybrid devices and their corresponding references are presented in Figure 5.8, along with the relative EQE enhancements. Hybridization with 1 pulse of QDs is found to provide a slight broadband increase of the EQE (1-4%), with a noticeable feature in the near infrared. Increasing the dose to 5 pulses and 9 pulses enhances the effect in the near-IR and another feature appears in the UV-blue part of the spectrum. Hybridization with higher doses starts to prove detrimental, with noticeable decreases of the EQE above 13 pulses. Hybridization with 17

pulses seriously damages the properties of the devices, with a large decrease of the EQE over the 350-1250 nm spectral range. A 9-pulse QD deposition is thus again found to be optimal, in good agreement with the J_{SC} dependence on the QD dose. For this QD dose, the rapid enhancement in the lower part of the spectrum corresponds to the absorption range of the QDs and is attributed to LDS. The QDs are directly photo-excited and the resulting photoluminescence is absorbed in the CIGS layer to generate extractable carriers, thus enhancing the overall quantum efficiency of the device. Above 560 nm, the QDs are non-absorbing and the EQE enhancement is attributed to scattering of the incident photons on QD aggregates. The embedded QD aggregates offer a good refractive index contrast to the surrounding ZnO/CdS interface (n_{QDs} = 2.5, n_{ZnO} = 1.94 and n_{CdS} = 2.34 at 1000 nm) and act as efficient scattering centres. The contributions of LDS and of scattering on QD aggregates to the photocurrent of the hybrid device can be estimated using the following equation:

$$\Delta J = \frac{\int_{\lambda_1}^{\lambda_2} \left(EQE_{hybrid} - EQE_{ref}\right) * \Phi_{\mathrm{AM1.5G}}\, d\lambda}{\int_{\lambda_1}^{\lambda_2} EQE_{hybrid} * \Phi_{\mathrm{AM1.5G}}\, d\lambda} \tag{43}$$

where EQE_{hybrid} and EQE_{ref} are the EQEs of the hybrid and reference devices, respectively, $\Phi_{\mathrm{AM1.5G}}$ is the photon flux of the AM1.5G solar spectrum (ASTMG173), ΔJ is the current density relative enhancement due to hybridization, and where the integration is done between 300 nm and 560 nm for the LDS contribution and between 560 nm and 1300 nm for the scattering component. Using this analysis, LDS and scattering on QD aggregates are estimated to contribute 1.9% and 8.1% of the J_{SC} enhancement due to hybridization. The significant contribution of LDS to the total photocurrent of the hybrid device reinforces the interest of using luminescent material as a scattering layer. In this analysis, the EQE enhancement for wavelengths below 560nm is entirely attribute to LDS, which may not be entirely accurate but provides a rough indication of the impact of the effect. Indeed in the ~500 to ~560nm wavelength range the EQE of the bare structure exceeds the QY of the QDs, negating any potential LDS. This is attributed to the neglected scattering contributions, which extends into the blue and UV parts of the solar spectrum.

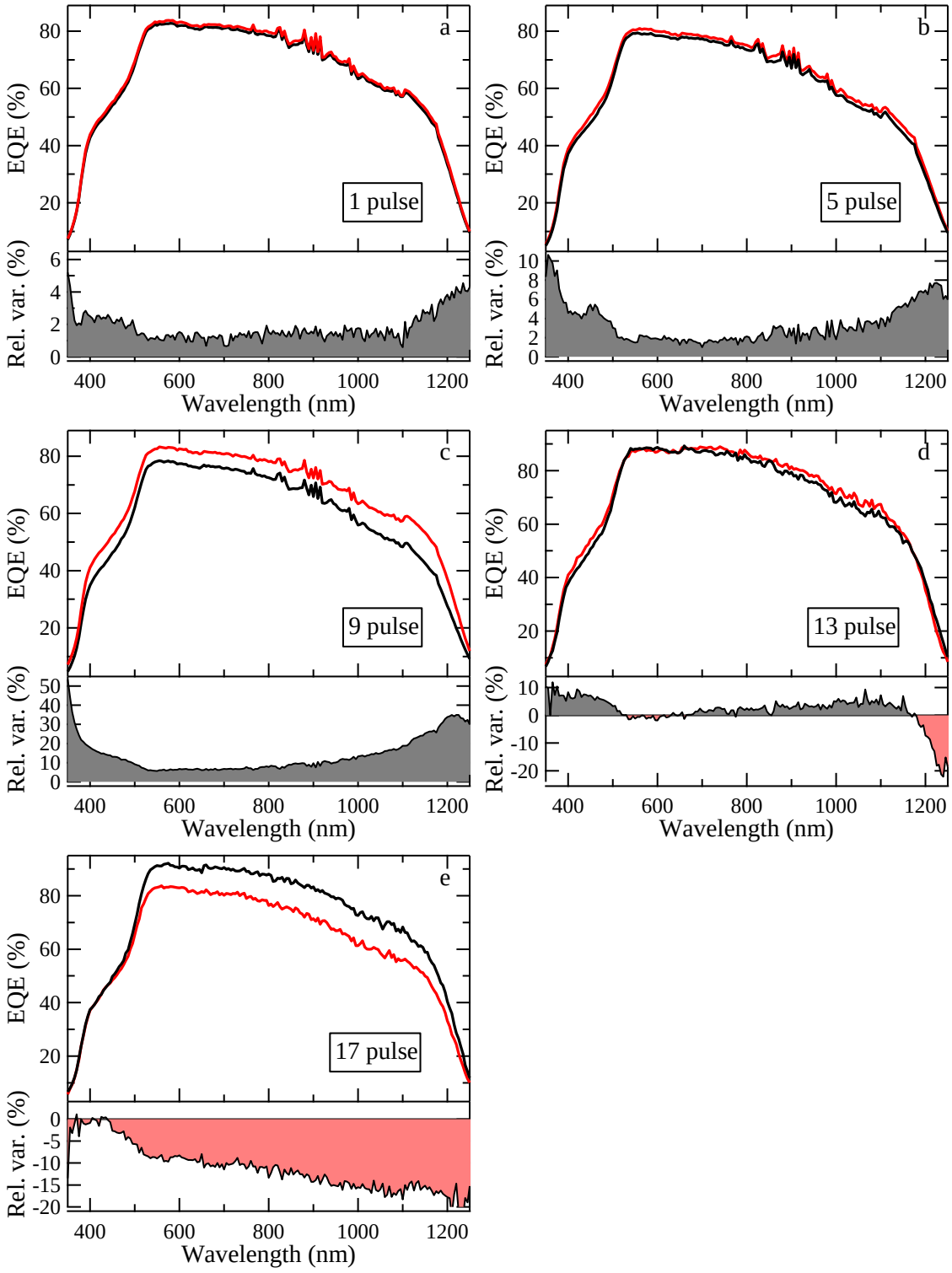

Figure 5.8: EQE curves of hybrid CIGS solar cells embedded with (a) 1 pulse, (b) 5 pulses, (c) 9 pulses, (d) 13 pulses and (e) 17 pulses of QDs (red) and their corresponding reference devices (black). The lower panel indicates the relative EQE variations due to hybridization.

5.3.4. Time-resolved spectroscopy

LDS in the QD layer was demonstrated using a 470 nm pulsed laser diode and time-resolved spectroscopy, by monitoring the PL decay of CIGS in a hybrid QD/CdS/CIGS structure and in a reference CdS/CIGS sample (red and black curves respectively in Figure 5.9). The bi-exponential dynamics of CIGS is found to be noticeably slower in the hybrid sample compare to the reference case, which indicates the presence of an additional slower pumping channel. The PL decay dynamics of the QDs in the hybrid sample (blue curve in Figure 6) is observed to be slower than the fast component of the CIGS decay dynamics. The PL decay of the QDs was fitted with a stretched exponential function to account for the distribution of lifetimes in the QDs, yielding an average lifetime of 4.79 ns. The CIGS dynamics was found to display a strong non-exponential behaviour and was modelled using the universal equation for free minority carrier recombination [120]

$$\frac{dn_{CIGS}}{dt} = -k_{CIGS,1} n_{CIGS}(t) - k_{CIGS,2} n_{CIGS}^2(t) \tag{44}$$

which can be analytically solved to provide the excess minority carrier population in CIGS n_{CIGS}:

$$n_{CIGS}(t) = \frac{n_{CIGS}(0)\exp\left(-k_{CIGS,1}t\right)}{1 + n_{CIGS}(0) * \frac{k_{CIGS,2}}{k_{CIGS,1}} * (1 - \exp(-k_{CIGS,1}t))} \tag{45}$$

where $k_{CIGS,1}$and $k_{CIGS,2}$ are the linear and quadratic recombination rate constants of the CIGS dynamics, corresponding to the low and high injection regime respectively.

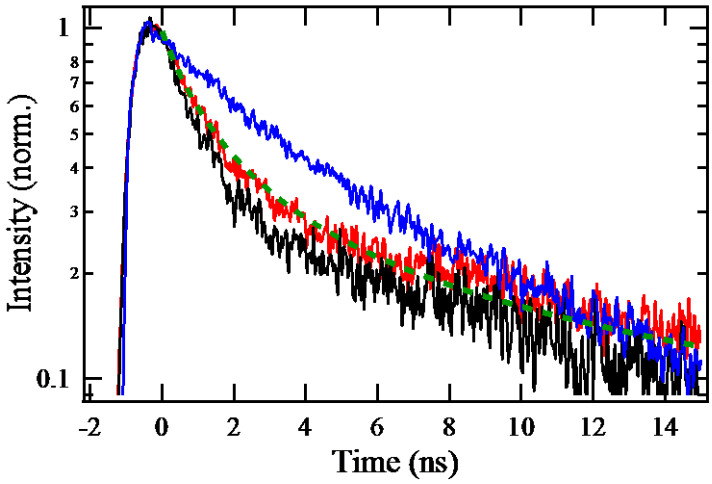

Figure 5.9: Photoluminescence decay dynamics of CIGS in a reference CdS/CIGS sample (black) and of CIGS and the QDs in a hybrid QD/CdS/CIGS sample (red and blue, respectively). The green dashed curve is a best fit to the CIGS dynamics in the hybrid sample using a rates equations model.

During the early times of the PL decay, the excess minority carrier density, estimated to be ~10^{19} cm^{-3}, is much larger than the typical net acceptor density of CIGS films (~10^{16}-10^{17} cm^{-3}) [120,121]. The decay dynamics is then driven by the quadratic term and the PL signal decays rapidly. When the excess minority carrier density decreases, linear recombination become dominant and the PL signal of CIGS starts decaying exponentially. A best fit to the measured decay curve of the reference CIGS sample yielded linear and quadratic decay times of 24.6 ns and 1.2 ns respectively, in good agreement with previous reports [122]. In the case of the hybrid QD/CIGS solar cell, the PL dynamics of CIGS was modelled using two coupled rate equations:

$$\frac{dn_{NQD}}{dt} = \alpha_{NQD}\delta(\mathrm{t}) - k_{NQD}n_{NQD} \tag{46}$$

$$\frac{dn_{CIGS}}{dt} = \left(1-\alpha_{NQD}\right)\delta(\mathrm{t}) + k_{NQD}QY_{NQD}n_{NQD} - k_{CIGS,1}n_{CIGS} - k_{CIGS,2}n_{CIGS}^2 \tag{47}$$

where k_{NQD} is the average decay rate of the QDs, measured experimentally, α_{NQD} is the absorption of the QDs at 470 nm, QY_{NQD} is the quantum yield of the QDs and $\delta(\mathrm{t})$ is a Kronecker delta function. A least squares optimization technique was used to fit the CIGS decay dynamics in the hybrid sample. A value of α_{NQD} = 0.12 was obtained, in good agreement with absorption measurements of QD films on glass. The LDS contribution to the CIGS PL, given by $\frac{\alpha_{NQD}\mathrm{QY_{QD}}}{1-\alpha_{NQD}}$, is found to be ~5.5%. Taking into account the variation

in EQE between 470 nm and 560 nm, this LDS contribution corresponds to an EQE relative enhancement of 8.4%, in good qualitative agreement with the measured 11% EQE relative enhancement at 470 nm. This analysis provides further evidence of the presence of a significant LDS pumping channel for the CIGS absorber in the hybrid QD/CIGS devices.

To understand the mechanism involved in the long wavelength enhancement of the EQE, a quantitative compositional study of the CdS/CIGS junction was undertaken using energy-dispersive X-ray spectroscopy (EDS). A cross sectional TEM image of the QD/CdS/CIGS region is overlaid with the EDS depth-resolved quantitative distributions of the atomic species constituting the different layers in Figure 5.10. A cadmium diffusion region extending nearly 100 nm into the CIGS absorber layer can be observed. p-type CIGS is known to contain abundant copper vacancies (V_{Cu}) and to allow massive cadmium ions to diffuse from the CdS layer to occupy copper sites (Cd_{Cu}) [123]. This high concentration of Cd_{Cu} sites locally dopes the CIGS and forms a type-inversion layer which creates a shallow buried CIGS homojunction [124]. The enhanced device performance induced by cadmium diffusion is understood to be in part due to the passivation of copper vacancies in the CIGS, which have been shown to be strong radiative recombination centres [125]. Cadmium diffusion also provides a strong enhancement of the built-in electric field intensity, which increases the extraction efficiency of the carriers generated near the CdS/CIGS interface [126]. Scattering of the incident light on QD clusters lowers the average photon penetration depth. This allows excitons to be generated closer to the depletion field of the cadmium diffusion layer and promotes their efficient extraction, thus enhancing the external quantum efficiency. The presence of Zn, S, Se and Cd also confirms that the particles visible previously in TEM are in fact CdSe/ZnS QDs.

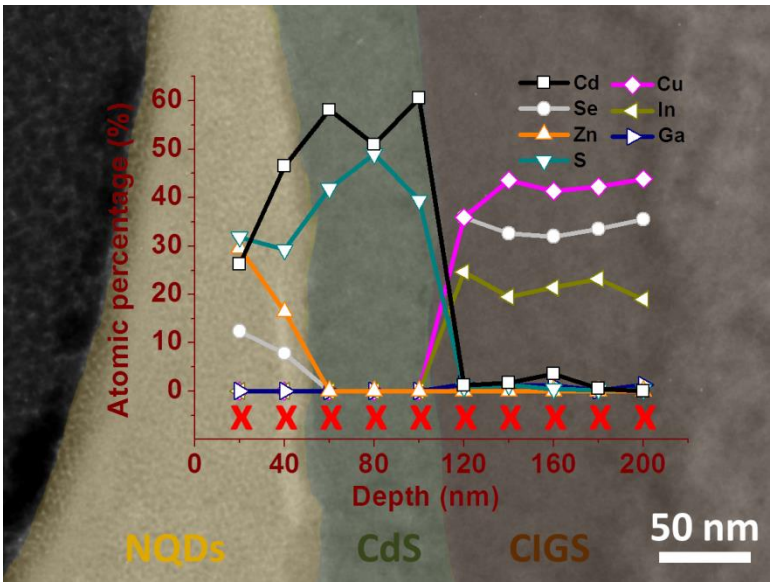

Figure 5.10: Depth-resolved quantitative compositional distributions of a CIGS/CdS junction coated with 17 pulses of QDs. The red crosses indicate each measurement point. The QD, CdS and CIGS layers were color-coded to facilitate comprehension (respectively beige, green and brown).

5.4. Conclusion

In this study, the successful integration of self-assembled aggregates of luminescent nanocrystal quantum dots (QDs) into flexible CIGS solar cells is demonstrated, yielding an ~11% relative enhancement in photon conversion efficiency. Luminescent down-shifting in the QDs and internal scattering of the incident light on self-assembled nanoparticle aggregates induce a large increase of the external quantum efficiency, in excess of 50% at 320nm. The low-cost pulsed-spray processing technique used to deposit the QDs makes this approach easily scalable and cost-effective, while the high deposition rates make it compatible with high-throughput roll-to-roll manufacturing. In this work, we utilize the self-aggregation of QD clusters, typical in spray deposited QD layers, to engineer an efficient light management scheme that significantly improves the efficiency of hybrid CIGS devices. The incorporation of luminescent colloidal QDs into hybrid photonics devices is believed to be a promising approach to help tackle the energy challenges of tomorrow.

5.5. Contributions to the work

The devices were designed in collaboration with NCTU, Taiwan, and fabricated in NCTU. The device characterization (IV, EQE, IQE) was done both in Southampton and NCTU, and the time-resolved spectroscopy study was carried out in NCTU. The detailed analysis of the data presented in this chapter was done by the author.

Chapter 6: Conclusions and Future Work

6.1. Conclusions

This thesis focuses on the integration of colloidal quantum dots into existing photovoltaic technologies. With a price rapidly decreasing and improving performances, the large-scale integration of QDs into consumer products is starting to become a reality. Having already found their way into next-generation televisions, with their inclusion in QD LED backlighting technology, these efficient low-cost emitters have proved to be of interest to the industry. In this context, the hybridization of solar cells with QDs appears to be a rather natural technological evolution. While the PV market was plagued by anticompetitive measures by the Chinese government for the past few years, which triggered anti-dumping measured by the European Commission in 2012, these subsidies are believed to be soon phased out. A more liberal PV market could provide the framework necessary for hybrid QD-PV devices to thrive.

In the 3rd chapter, we demonstrated the value of using PbS QDs as an absorber for thin-film PV devices. In this scheme, the high absorption cross-section of the QDs could be used to enhance the overall absorptivity of silicon structures. We demonstrated that excitons generated in the QDs can be efficiently non-radiatively transferred to an underlying silicon substrate through RET. This offers a strong proof of concept that QD excitons could be efficiently funneled to a bulk p-n junction, which could separate them to provide useable photocurrents.

In the 4th chapter, we demonstrate that QDs can also be used in InGaP thin-film solar cells to better match the device response of the devices with the solar spectrum, through LDS, and to recycle carriers trapped within the window layer. This is found to provide a large 14.6% relative enhancement of the efficiency. In this study, the QDs were simply spin-coated on top of the device, in close proximity with the window layer. III-V solar cells typical integrate complex AR-coating at the surface, which help quench the reflection at the interface between air and high-refractive index semiconductors. Using the QDs as the first layer of a multilayer AR coating could then allow the combination of LDS and RET-

LDS enhancement with an improved broadband light coupling, while protecting the QD under a protective dielectric barrier.

The 5th chapter focused onto the integration of QDs within the layer stack of a CIGS solar cell. In this case, the QDs are spray-deposited between the CdS layer and the top contact. Luminescent down-shifting is demonstrated using time-resolved spectroscopy. Spray deposition is also found to provide a way to control the morphology of the QD film, which is found to form micrometer wide dendrite-like structures. This structuration of the QD film is found to be very beneficial to the devices, by inducing scattering above the p-n junction and lowering the average penetration depth of the solar excitation. The dependence of the photon conversion efficiency of the hybrid devices on the QD dose is investigated, and a clear optimum is found.

6.2. Future work

The enhancement schemes proposed in this thesis are novel and remain unoptimitized. This is especially true of RET-LDS and internal scattering on structured QD films in PV devices, which are believed to be reported for the first time in this work. Optimization of the hybrid QD-CIGS devices is on-going. The careful tuning of the emission wavelength of the QDs, critical to all RET mechanisms, is under investigation. The possibility of a better control of the QD film structure, using techniques such as inkjet-printing and dip-coating, could also lead to a better tuning of the scattering properties of the QD film while increasing the overall QD coverage. Such hybridization schemes are of course also good candidates to improve the efficiency of CdTe solar cells, which share a very similar layer structure with CIGS devices. An ongoing collaboration with Ken Durose's group in Liverpool has already shown some promising results, with a large enhancement of the EQE in the UV and blue, but at the cost of significant additional series resistances.

References

[1] International Energy Agency, The Power of Transformation -- Wind, Sun and the Economics of Flexible Power Systems, 2014. http://www.iea.org/w/bookshop/add.aspx?id=465 (accessed August 16, 2014).

[2] A. Lopez, B. Roberts, D. Heimiller, N. Blair, G. Porro, (2012).

[3] B. Parida, S. Iniyan, R. Goic, Renew. Sustain. Energy Rev. 15 (2011) 1625–1636.

[4] V. Shah, J. Booream-Phelps, S. Min, 2014 Outlook: Let the Second Gold Rush Begin, 2014. http://www.qualenergia.it/sites/default/files/articolo-doc/DBSolar.pdf.

[5] D. V Talapin, J.H. Nelson, E. V Shevchenko, S. Aloni, B. Sadtler, a P. Alivisatos, Nano Lett. 7 (2007) 2951–9.

[6] L. Carbone, C. Nobile, M. De Giorgi, F. Della Sala, G. Morello, P. Pompa, M. Hytch, E. Snoeck, A. Fiore, I.R. Franchini, M. Nadasan, A.F. Silvestre, L. Chiodo, S. Kudera, R. Cingolani, R. Krahne, L. Manna, Nano Lett. 7 (2007) 2942–50.

[7] A.B. Greytak, P.M. Allen, W. Liu, J. Zhao, E.R. Young, Z. Popović, B. Walker, D.G. Nocera, M.G. Bawendi, Chem. Sci. 3 (2012) 2028–2034.

[8] C.-H.M. Chuang, P.R. Brown, V. Bulović, M.G. Bawendi, Nat. Mater. 13 (2014) 1–6.

[9] D.L. Dexter, J. Lumin. 18-19 (1979) 779–784.

[10] A.L. Rogach, Semiconductor nanocrystal quantum dots, Springer, 2008.

[11] C. Kittel, P. McEuen, Introduction to solid state physics, John Wiley & Sons, Ltd, 1976. http://tocs.ulb.tu-darmstadt.de/125610068.pdf (accessed August 7, 2014).

[12] V. Klimov, Semiconductor and metal nanocrystals: synthesis and electronic and optical properties, CRC Press, 2003. http://books.google.co.uk/books?hl=en&lr=&id=sarqqnaw-7oC&oi=fnd&pg=PR3&dq=V.+I.+Klimov,+Semiconductor+and+metal+nanocrystals&ots=GJtC8fMkMO&sig=k0D9tOUiiat8r6y68F95kJGDO6A (accessed August 7, 2014).

[13] S. Gaponenko, Optical properties of semiconductor nanocrystals, Cambridge University Press, 1998. http://books.google.co.uk/books?hl=en&lr=&id=1Y1zvul3kbQC&oi=fnd&pg=PP1&dq=gaponenko+optical+properties&ots=xJTeWVa0Pd&sig=HEutQ_ceEGk9mBWPs847gqQcLhM (accessed August 7, 2014).

[14] A.L. Efros, M. Rosen, Annu. Rev. Mater. Sci. 30 (2000) 475–521.

[15] R. Schaller, V. Klimov, Phys. Rev. Lett. 92 (2004) 186601.

[16] R.J. Ellingson, M.C. Beard, J.C. Johnson, P. Yu, O.I. Micic, A.J. Nozik, A. Shabaev, A.L. Efros, Nano Lett. 5 (2005) 865–71.

[17] O. Madelung, Semiconductors: data handbook, 3rd edition, Springer, 2004. http://books.google.co.uk/books?hl=en&lr=&id=v_8sMfNAcA4C&oi=fnd&pg=PA1&dq=madelung+data+handbook&ots=3VBn3o_L-H&sig=StMi7wL_RWwt0QckyhaFyrJVtzI (accessed August 7, 2014).

[18] S. Ahmed, S. Islam, S. Mohammed, IEEE Trans. Electron Devices. 57 (2010) 164–173.

[19] O. V Prezhdo, Acc. Chem. Res. 42 (2009) 2005–16.

[20] P. Sercel, K. Vahala, Phys. Rev. B. 42 (1990) 3690–3710.

[21] L.E. Brus, J. Chem. Phys. 80 (1984) 4403.

[22] A. Efros, Sov. Phys. Semicond. Ussr. 16 (1982) 772–775. http://scholar.google.co.uk/scholar?q=Efros+interband+absorption+of+light+sphere+1982&btnG=&hl=en&as_sdt=0,5#0 (accessed August 7, 2014).

[23] L. Brus, J. Chem. Phys. (1983). http://scitation.aip.org/content/aip/journal/jcp/79/11/10.1063/1.445676 (accessed August 7, 2014).

[24] B.O. Dabbousi, J. Rodriguez-Viejo, F. V. Mikulec, J.R. Heine, H. Mattoussi, R. Ober, K.F. Jensen, M.G. Bawendi, J. Phys. Chem. B. 101 (1997) 9463–9475.

[25] M.A. Hines, P. Guyot-Sionnest, J. Phys. Chem. 100 (1996) 468–471.

[26] J. Yao, D.R. Larson, H.D. Vishwasrao, W.R. Zipfel, W.W. Webb, Proc. Natl. Acad. Sci. U. S. A. 102 (2005) 14284–9.

[27] Invitrogen Corporation, QDdot Nanocrystal technology, 2010. www.invitrogen.com.

[28] V.I. Klimov, S.A. Ivanov, J. Nanda, M. Achermann, I. Bezel, J.A. McGuire, A. Piryatinski, Nature. 447 (2007) 441–6.

[29] H. Zhong, Y. Zhou, Y. Yang, C. Yang, Y. Li, J. Phys. Chem. C. 111 (2007) 6538–6543.

[30] National Renewable Energy Laboratory (NREL), Best Research-Cell Efficiencies, 2014. http://www.nrel.gov/ncpv/images/efficiency_chart.jpg.

[31] H. Sterling, R. Swann, Solid. State. Electron. 8 (1965) 653–654.

[32] W. Spear, P. LeComber, Solid State Comm. 17 (1975) 1193.

[33] D.E. Carlson, C.R. Wronski, Appl. Phys. Lett. 28 (1976) 671–673.

[34] J. Poortmans, V. Arkhipov, Thin Film Solar Cells Fabrication, Characterization and Applications, John Wiley & Sons, Ltd, 2006.

[35] I. Dharmadasa, Advances in thin-film solar cells, Pan Stanford Publishing, 2012. http://link.springer.com/chapter/10.1007/978-1-4899-0418-8_1 (accessed August 9, 2014).

[36] First Solar, First Solar Builds the Highest Efficiency Thin-Film PV Cell on Record, 2014.

[37] Fraunhofer ISE, Photovoltaics Report, 2014.

[38] T. Forster, Naturwissenschaften. 33 (1946) 166–175.

[39] T. Förster, Ann. Phys. 437 (1948) 55–75.

[40] V.M. Agranovich, D.M. Basko, G.C. La Rocca, F. Bassani, Synth. Met. 116 (2001) 349–351.

[41] M. Achermann, M. Petruska, D.D. Koleske, M.H. Crawford, V.I. Klimov, Nano Lett. 6 (2006) 1396–400.

[42] S. Chanyawadee, P.G. Lagoudakis, R.T. Harley, M.D.B. Charlton, D. V Talapin, H.W. Huang, C.-H. Lin, Adv. Mater. 22 (2010) 602–6.

[43] S. Pimputkar, J.S. Speck, S.P. DenBaars, S. Nakamura, Nat. Photonics. 3 (2009) 180–182.

[44] G. Itskos, C.R. Belton, G. Heliotis, I.M. Watson, M.D. Dawson, R. Murray, D.D.C. Bradley, Nanotechnology. 20 (2009) 275207.

[45] V.M. Agranovich, Y.N. Gartstein, M. Litinskaya, Chem. Rev. 111 (2011) 5179–214.

[46] I. Prigogine, S.A. Rice, R.R. Chance, A. Prock, R. Silbey, Advances in Chemical Physics, John Wiley & Sons, Inc., Hoboken, NJ, USA, 1978.

[47] S. Chanyawadee, R. Harley, M. Henini, D. Talapin, P. Lagoudakis, Phys. Rev. Lett. 102 (2009) 077402.

[48] S. Chanyawadee, R.T. Harley, D. Taylor, M. Henini, A.S. Susha, A.L. Rogach, P.G. Lagoudakis, Appl. Phys. Lett. 94 (2009) 233502.

[49] S. Lu, A. Madhukar, Nano Lett. 7 (2007) 3443–51.

[50] H.M. Nguyen, O. Seitz, W. Peng, Y.N. Gartstein, Y.J. Chabal, A. V Malko, ACS Nano. 6 (2012) 5574–82.

[51] H. Kuhn, J. Chem. Phys. 53 (1970) 101.

[52] M. Lunz, A.L. Bradley, W.Y. Chen, Y.K. Gun'ko, J. Phys. Chem. C. 113 (2009) 3084–3088.

[53] E.M. Purcell, Phys. Rev. 1-2 (1946) 693.

[54] K.H. Drexhage, J. Lumin. 1-2 (1970) 693–701.

[55] R.R. Chance, A. Prock, R. Silbey, Adv. Chem. Phys. 37 (1978).

[56] A.P. Alivisatos, M.F. Arndt, S. Efrima, D.H. Waldeck, C.B. Harris, J. Chem. Phys. 86 (1987) 6540.

[57] P.M. Whitmore, A.P. Alivisatos, C.B. Harris, Phys. Rev. Lett. (1983).

[58] V. Gowrishankar, S.R. Scully, A.T. Chan, M.D. McGehee, Q. Wang, H.M. Branz, J. Appl. Phys. 103 (2008) 064511.

[59] S. Chanyawadee, Resonant Energy Transfer in Light Harvesting and Light Emitting Applications, Southampton, 2009.

[60] S. Lu, Z. Lingley, T. Asano, D. Harris, T. Barwicz, S. Guha, A. Madhukar, Nano Lett. 9 (2009) 4548–4552.

[61] K. Orgassa, U. Rau, Q. Nguyen, H. Werner Schock, J.H. Werner, Prog. Photovoltaics Res. Appl. 10 (2002) 457–463.

[62] B.E. Hardin, H.J. Snaith, M.D. McGehee, Nat. Photonics. 6 (2012) 162–169.

[63] K. Shankar, X. Feng, C.A. Grimes, ACS Nano. 3 (2009) 788–94.

[64] C. Siegers, U. Würfel, M. Zistler, H. Gores, J. Hohl-Ebinger, A. Hinsch, R. Haag, ChemPhysChem. 9 (2008) 793–798.

[65] J.-S. Huang, T. Goh, X. Li, M.Y. Sfeir, E. a Bielinski, S. Tomasulo, M.L. Lee, N. Hazari, A.D. Taylor, Nat. Photonics. 7 (2013) 479–485.

[66] K. Cnops, B.P. Rand, D. Cheyns, B. Verreet, M.A. Empl, P. Heremans, Nat. Commun. 5 (2014) 3406.

[67] V.M. Agranovich, G.C. Rocca, F. Bassani, J. Exp. Theor. Phys. Lett. 66 (1997) 748–751.

[68] S. Blumstengel, S. Sadofev, C. Xu, J. Puls, F. Henneberger, Phys. Rev. Lett. 97 (2006) 8–11.

[69] G. Heliotis, G. Itskos, R. Murray, M.D. Dawson, I.M. Watson, D.D.C. Bradley, Adv. Mater. 18 (2006) 334–338.

[70] M. Achermann, M. Petruska, S. Kos, D.L. Smith, D.D. Koleske, V.I. Klimov, Nature. 429 (2004) 642–6.

[71] S. Rohrmoser, J. Baldauf, R.T. Harley, P.G. Lagoudakis, S. Sapra, A. Eychmüller, I.M. Watson, Appl. Phys. Lett. 91 (2007) 18–21.

[72] J.J. Rindermann, G. Pozina, B. Monemar, L. Hultman, H. Amano, P.G. Lagoudakis, Phys. Rev. Lett. 107 (2011) 1–5.

[73] I. Kang, J. Oh, F.W. Wise, K. Chang, G. Ihm, S. Lee, Phys. Rev. B. 14 (1996) 1632.

[74] F.W. Wise, Acc. Chem. Res. 33 (2000) 773–780.

[75] G. Konstantatos, E.H. Sargent, Colloidal Quantum Dot Optoelectronics and Photovoltaics, Cambridge University Press, 2013. http://www.amazon.co.uk/Colloidal-Quantum-Dot-Optoelectronics-Photovoltaics/dp/0521198267 (accessed August 12, 2014).

[76] J.J.H. Pijpers, R. Ulbricht, K.J. Tielrooij, A. Osherov, Y. Golan, C. Delerue, G. Allan, M. Bonn, Nat. Phys. 5 (2009) 811–814.

[77] G. Nair, M.G. Bawendi, Phys. Rev. B - Condens. Matter Mater. Phys. 76 (2007) 5–8.

[78] G. Nair, S.M. Geyer, L.Y. Chang, M.G. Bawendi, Phys. Rev. B - Condens. Matter Mater. Phys. 78 (2008) 1–10.

[79] M. Ben-Lulu, D. Mocatta, M. Bonn, U. Banin, S. Ruhman, Nano Lett. 8 (2008) 1207–1211. papers://9ab038d4-69c9-48f5-bf74-699db84987f0/Paper/p376.

[80] Z. Ning, O. Voznyy, J. Pan, S. Hoogland, V. Adinolfi, J. Xu, M. Li, A.R. Kirmani, J. Sun, J. Minor, K.W. Kemp, H. Dong, L. Rollny, A. Labelle, G. Carey, B. Sutherland, I. Hill, A. Amassian, H. Liu, J. Tang, O.M. Bakr, E.H. Sargent, Nat. Mater. 13 (2014) 4–10.

[81] D.J. Milliron, Nat. Mater. 13 (2014) 772–773.

[82] L. Turyanska, A. Patanè, M. Henini, B. Hennequin, N.R. Thomas, Appl. Phys. Lett. 90 (2007) 1–4.

[83] Hamamatsu Photonics, Guide to Streak Cameras, 2008.

[84] P. Andreakou, M. Brossard, C. Li, M. Bernechea, G. Konstantatos, P.G. Lagoudakis, J. Phys. Chem. C. 117 (2013) 1887–1892.

[85] M.S. Gaponenko, A.A. Lutich, N.A. Tolstik, A.A. Onushchenko, A.M. Malyarevich, E.P. Petrov, K. V. Yumashev, Phys. Rev. B - Condens. Matter Mater. Phys. 82 (2010) 1–9.

[86] M.T. Nimmo, L.M. Caillard, W. De Benedetti, H.M. Nguyen, O. Seitz, Y.N. Gartstein, Y.J. Chabal, A. V. Malko, ACS Nano. 7 (2013) 3236–3245.

[87] Alta Devices, Alta Devices Achieves 30.8% Efficiency Record with New Generation Solar Cell Technology, 2013.

[88] E. Klampaftis, D. Ross, K.R. McIntosh, B.S. Richards, Sol. Energy Mater. Sol. Cells. 93 (2009) 1182–1194.

[89] R.R. King, D.C. Law, K.M. Edmondson, C.M. Fetzer, G.S. Kinsey, H. Yoon, R.A. Sherif, N.H. Karam, Appl. Phys. Lett. 90 (2007) 183516.

[90] W. Guter, J. Schöne, S.P. Philipps, M. Steiner, G. Siefer, A. Wekkeli, E. Welser, E. Oliva, A.W. Bett, F. Dimroth, Appl. Phys. Lett. 94 (2009) 223504.

[91] J.F. Geisz, D.J. Friedman, J.S. Ward, A. Duda, W.J. Olavarria, T.E. Moriarty, J.T. Kiehl, M.J. Romero, A.G. Norman, K.M. Jones, Appl. Phys. Lett. 93 (2008) 123505.

[92] Fraunhofer Institute for Solar Energy Systems ISE, World Record Solar Cell with 44.7% Efficiency, 2013. http://www.ise.fraunhofer.de/en/press-and-media/press-releases/presseinformationen-2013/world-record-solar-cell-with-44.7-efficiency.

[93] X. Yan, D.J. Poxson, J. Cho, R.E. Welser, A.K. Sood, J.K. Kim, E.F. Schubert, Adv. Funct. Mater. 23 (2013) 583–590.

[94] A. Luque, S. Hegedus, Handbook of Photovoltaic Science and Engineering, John Wiley & Sons, Ltd, Chichester, UK, 2010.

[95] B. Richards, Sol. Energy Mater. Sol. Cells. 90 (2006) 2329–2337.

[96] X. Huang, S. Han, W. Huang, X. Liu, Chem. Soc. Rev. 42 (2013) 173–201.

[97] C.P. Thomas, A.B. Wedding, S.O. Martin, Sol. Energy Mater. Sol. Cells. 98 (2012) 455–464.

[98] H.-J. Muffler, M. Bär, I. Lauermann, K. Rahne, M. Schröder, M.C. Lux-Steiner, C.-H. Fischer, T.P. Niesen, F. Karg, Sol. Energy Mater. Sol. Cells. 90 (2006) 3143–3150.

[99] H.-C. Chen, C.-C. Lin, H.-V. Han, K.-J. Chen, Y.-L. Tsai, Y.-A. Chang, M.-H. Shih, H.-C. Kuo, P. Yu, Sol. Energy Mater. Sol. Cells. 104 (2012) 92–96.

[100] X. Pi, Q. Li, D. Li, D. Yang, Sol. Energy Mater. Sol. Cells. 95 (2011) 2941–2945.

[101] Z. Cheng, F. Su, L. Pan, M. Cao, Z. Sun, J. Alloys Compd. 494 (2010) L7–L10.

[102] S.D. Hodgson, W.S.M. Brooks, A.J. Clayton, G. Kartopu, V. Barrioz, S.J.C. Irvine, Nano Energy. 2 (2013) 21–27.

[103] O. Chen, J. Zhao, V.P. Chauhan, J. Cui, C. Wong, D.K. Harris, H. Wei, H.-S. Han, D. Fukumura, R.K. Jain, M.G. Bawendi, Nat. Mater. 12 (2013) 445–51.

[104] S. Kalytchuk, S. Gupta, O. Zhovtiuk, A. Vaneski, S. V. Kershaw, H. Fu, Z. Fan, E.C.H. Kwok, C.-F. Wang, W.Y. Teoh, A.L. Rogach, J. Phys. Chem. C. 118 (2014) 16393–16400.

[105] I. Moreno, J.J. Araiza, M. Avendano-Alejo, Opt. Lett. 30 (2005) 914.

[106] G. Bauer, Ann. Phys. 411 (1934) 434–464.

[107] F. Pedrotti, L. Pedrotti, L. Pedrotti, Introduction to optics, 3rd edition, Addison-Wesley, 2006. http://scholar.google.co.uk/scholar?q=F.+L.+Pedrotti,+L.+M.+Pedrotti,+L.+S.+Pedrotti,+Introduction+to+Optics&btnG=&hl=en&as_sdt=0,5#0 (accessed August 7, 2014).

[108] O. Heavens, Optical properties of thin solid films, Dover Publications, 2011. http://scholar.google.co.uk/scholar?q=O.+S.+Heavens,+Optical+Properties+of+Thin+Solid+Films,+Dover+Publications&btnG=&hl=en&as_sdt=0,5#0 (accessed August 7, 2014).

[109] J. Hoy, P.J. Morrison, L.K. Steinberg, W.E. Buhro, R.A. Loomis, J. Phys. Chem. Lett. 4 (2013) 2053–2060.

[110] A. Mukherjee, S. Ghosh, J. Phys. D. Appl. Phys. 45 (2012) 195103.

[111] M.A. Green, K. Emery, Y. Hishikawa, W. Warta, E.D. Dunlop, Prog. Photovoltaics Res. Appl. 22 (2014) 701–710.

[112] A. Chirilă, S. Buecheler, F. Pianezzi, P. Bloesch, C. Gretener, A.R. Uhl, C. Fella, L. Kranz, J. Perrenoud, S. Seyrling, R. Verma, S. Nishiwaki, Y.E. Romanyuk, G. Bilger, A.N. Tiwari, Nat. Mater. 10 (2011) 857–61.

[113] F. Engelhardt, L. Bornemann, M. Köntges, T. Meyer, J. Parisi, E. Pschorr-Schoberer, B. Hahn, W. Gebhardt, W. Riedl, U. Rau, Prog. Photovoltaics Res. Appl. 7 (1999) 423–436.

[114] H.-C. Chen, C.-C. Lin, H.-W. Han, Y.-L. Tsai, C.-H. Chang, H.-W. Wang, M.-A. Tsai, H.-C. Kuo, P. Yu, Opt. Express. 19 Suppl 5 (2011) A1141–7.

[115] Q. Sun, Y.A. Wang, L.S. Li, D. Wang, T. Zhu, J. Xu, C. Yang, Y. Li, Nat. Photonics. 1 (2007) 717–722.

[116] K.-J. Chen, H.-C. Chen, K.-A. Tsai, C.-C. Lin, H.-H. Tsai, S.-H. Chien, B.-S. Cheng, Y.-J. Hsu, M.-H. Shih, C.-H. Tsai, H.-H. Shih, H.-C. Kuo, Adv. Funct. Mater. 22 (2012) 5138–5143.

[117] G.C. Glaeser, U. Rau, Thin Solid Films. 515 (2007) 5964–5967.

[118] E. Klampaftis, D. Ross, S. Seyrling, A.N. Tiwari, B.S. Richards, Sol. Energy Mater. Sol. Cells. 101 (2012) 62–67.

[119] W. Han, Z. Lin, Angew. Chem. Int. Ed. Engl. 51 (2012) 1534–46.

[120] B. Ohnesorge, R. Weigand, G. Bacher, A. Forchel, W. Riedl, F.H. Karg, Appl. Phys. Lett. 73 (1998) 1224.

[121] M. Gloeckler, A. Fahrenbruch, J.R. Sites, 3rd World Conf. Photovolt. Energy Convers. 1 (2003) 491–494 Vol.1.

[122] S. Shirakata, T. Nakada, Thin Solid Films. 515 (2007) 6151–6154.

[123] T. Nakada, A. Kunioka, Appl. Phys. Lett. 74 (1999) 2444.

[124] C.S. Jiang, H.R. Mutinho, F.S. Hasoon, H.A. Al-Thani, D.J. Friedman, J.F. Geisz, Q. Wang, M.J. Romero, M.M. Al-Jassim, NREL Conf. Pap. (2003). http://www.osti.gov/scitech/biblio/15004237 (accessed August 7, 2014).

[125] Y. Liao, Y. Wang, Y. Yen, C.-H. Chen, D. Hsieh, S. Chen, C.-Y. Lee, C.-C. Lai, W.-C. Kuo, J.-Y. Juang, K.-H. Wu, S.-J. Cheng, C.-H. Lai, F.-I. Lai, S.-Y. Kuo, H.-C. Kuo, Y.-L. Chueh, ACS Nano. 7 (2013) 7318–29.

[126] U. Rau, M. Schmidt, Thin Solid Films. 387 (2001) 141–146.